

OPTIMAL DESIGN OF SPARSE MIMO ARRAYS FOR WIDEBAND
NEAR-FIELD IMAGING BASED ON A STATISTICAL FRAMEWORK

A THESIS SUBMITTED TO
THE GRADUATE SCHOOL OF NATURAL AND APPLIED SCIENCES
OF
MIDDLE EAST TECHNICAL UNIVERSITY

BY

MEHMET BURAK KOCAMIŞ

IN PARTIAL FULFILLMENT OF THE REQUIREMENTS
FOR
THE DEGREE OF MASTER OF SCIENCE
IN
ELECTRICAL AND ELECTRONICS ENGINEERING

MAY 2018

Approval of the thesis:

**OPTIMAL DESIGN OF SPARSE MIMO ARRAYS FOR WIDEBAND
NEAR-FIELD IMAGING BASED ON A STATISTICAL FRAMEWORK**

submitted by **MEHMET BURAK KOCAMIŞ** in partial fulfillment of the requirements for the degree of **Master of Science in Electrical and Electronics Engineering Department, Middle East Technical University** by,

Prof. Dr. Halil Kalıpçılar
Dean, Graduate School of **Natural and Applied Sciences**

Prof. Dr. Tolga Çiloğlu
Head of Department, **Electrical and Electronics Engineering**

Assist. Prof. Dr. Figen S. Öktem
Supervisor, **Electrical and Electronics Eng. Dept., METU**

Examining Committee Members:

Prof. Dr. Çağatay Candan
Electrical and Electronics Engineering Department, METU

Assist. Prof. Dr. Figen S. Öktem
Electrical and Electronics Engineering Department, METU

Prof. Dr. Sencer Koç
Electrical and Electronics Engineering Department, METU

Assoc. Prof. Dr. Lale Alatan
Electrical and Electronics Engineering Department, METU

Prof. Dr. Sinan Gezici
Electrical and Electronics Eng. Dept., Bilkent University

Date:

I hereby declare that all information in this document has been obtained and presented in accordance with academic rules and ethical conduct. I also declare that, as required by these rules and conduct, I have fully cited and referenced all material and results that are not original to this work.

Name, Last Name: MEHMET BURAK KOCAMIŞ

Signature :

ABSTRACT

OPTIMAL DESIGN OF SPARSE MIMO ARRAYS FOR WIDEBAND NEAR-FIELD IMAGING BASED ON A STATISTICAL FRAMEWORK

Kocamış, Mehmet Burak

M.S., Department of Electrical and Electronics Engineering

Supervisor : Assist. Prof. Dr. Figen S. Öktem

May 2018, 76 pages

Wideband near-field imaging is an emerging remote sensing technique in various applications such as airport security, surveillance, medical diagnosis, and through-wall imaging. Recently, there has been increasing interest in using sparse multiple-input-multiple-output (MIMO) arrays to achieve high resolution with reduced hardware complexity and cost. In this thesis, based on a statistical framework, an optimal design method is presented for two-dimensional MIMO arrays in wideband near-field imaging. Different optimality criteria are defined based on the image reconstruction quality obtained with the final design. An algorithm called clustered sequential backward selection is used to perform the optimization of the chosen criterion over all initial locations of antenna elements. The developed framework also allows incorporating different practical considerations into the design such as synthetic apertures and antenna patterns. The performance of the approach is illustrated for a microwave imaging application. The designs obtained for different observation settings are compared with some commonly used sparse array configurations in terms of image reconstruction quality. Numerical simulation results suggest that the approach can yield designs that outperform conventional sparse array configurations in terms of image reconstruction quality for a wide range of SNR.

Keywords: Wideband near field imaging, optimal MIMO array design, sparse array, image reconstruction

ÖZ

GENİŞBANTLI YAKIN ALAN GÖRÜNTÜLEMESİ İÇİN SEYREK ÇOK-GİRDİLİ ÇOK-ÇIKTILI DİZİLERİN İSTATİSTİKSEL ÇERÇEVEYE DAYALI OPTİMAL DİZAYNI

Kocamış, Mehmet Burak

Yüksek Lisans, Elektrik ve Elektronik Mühendisliği Bölümü

Tez Yöneticisi : Dr. Öğr. Üyesi Figen S. Öktem

Mayıs 2018 , 76 sayfa

Genişbantlı mikrodalga görüntüleme, havaalanı güvenliği, gözetim, tıbbi teşhis ve duvar-arkası görüntüleme gibi çok çeşitli uygulama alanlarında kullanılan gelişmekte olan bir uzaktan algılama tekniğidir. Yakın zamanda, yüksek çözünürlüğü başarmakla beraber donanımsal karmaşıklığın ve maliyetin azaltılması için seyrek çok-girdili çok-çıkıtlı (MIMO) dizilere olan ilgi artmıştır. Bu tez çalışmasında, istatistiksel bir çerçeveye dayandırılarak, genişbantlı yakın alan görüntülemeye iki boyutlu MIMO dizilerin optimal dizayn metodu sunulmaktadır. Nihai dizaynla elde edilen görüntü oluşturma kalitesine bağlı çeşitli en iyilik ölçütleri tanımlanmaktadır. Seçilen ölçütün bütün anten elemanlarının ilk yerleri üzerinden en iyilemesi kümeleşmiş ardışık geri seçim (KAGS) olarak adlandırılan algoritma kullanılarak gerçekleştirilir. Ayrıca, geliştirilen çerçeve, sentetik açıklık ve anten paternini dizayna dahil etme gibi değişik pratik düşünceleri uygulamaya imkan sağlar. Bu yaklaşımın performansı mikrodalga görüntüleme uygulamalarında gösterilmektedir. Bu yaklaşım kullanılarak değişik gözlem durumları için elde edilen dizaynlar yaygın olarak kullanılan seyrek anten dizilimleriyle görüntü oluşturma kaliteleri açısından karşılaştırılmaktadır. Sayısal benzetim sonuçları, önerilen yaklaşım ile elde edilen dizaynların yaygın olarak kullanılan seyrek anten dizilimlerine göre, geniş bir SNR aralığında daha iyi görüntü oluşturma kalitesi sağlayabildiğini göstermektedir.

Anahtar Kelimeler: geniş bantlı yakın alan görüntüleme, optimal MIMO dizi dizaynı, seyrek dizi, görüntü geri oluşturma

To my family with gratitude and love

ACKNOWLEDGMENTS

I would like to express my deep gratitude and appreciation to my supervisor Assist. Prof. Dr. Figen S. Öktem for her guidance, useful comments and remarks from the beginning till the end of this thesis study.

I would also like to thank my parents, who have supported me throughout the entire process, both by keeping me harmonious and helping me putting pieces together. I will be grateful forever for your love.

TABLE OF CONTENTS

ABSTRACT	v
ÖZ	vii
ACKNOWLEDGMENTS	x
TABLE OF CONTENTS	xi
LIST OF TABLES	xiv
LIST OF FIGURES	xv
LIST OF ABBREVIATIONS	xxi
CHAPTERS	
1 INTRODUCTION	1
1.1 Wideband Near-Field MIMO Imaging	1
1.2 Design of Wideband Near-Field MIMO Imaging Systems	3
1.3 Contributions and Outline	6
2 OPTIMAL DESIGN OF SPARSE MIMO ARRAYS BASED ON A STATISTICAL FRAMEWORK	7
2.1 Observation Model for Wideband Near-Field MIMO Imaging	8
2.1.1 Continuous Observation Model	8
2.1.2 Discrete Observation Model	9

2.2	Optimal Design Method	11
2.2.1	Statistical Framework	11
2.2.1.1	Maximum Likelihood (ML) Framework	11
2.2.1.2	Maximum a Posteriori (MAP) Frame- work	12
2.2.2	Cost Formulation Based on Error Covariance Matrix	16
2.2.3	Optimization Algorithm	16
2.3	Numerical Results	18
2.3.1	Simulation Scenario	18
2.3.2	Simulation Results	22
2.3.2.1	Results for ML Framework	22
2.3.2.2	Results for MAP Framework	37
2.3.2.3	Comparison of Obtained Designs	45
3	OPTIMAL DESIGN WITH PRACTICAL CONSIDERATIONS	53
3.1	Enforcing a Synthetic Aperture	53
3.1.1	Observation Model	54
3.1.2	Optimal Design Method	54
3.1.3	Numerical Results	55
3.1.3.1	Simulation Scenario	55
3.1.3.2	Results for MAP Framework	56
3.2	Inclusion of Antenna Pattern	60
3.2.1	Observation Model	61

3.2.2	Optimal Design Method	61
3.2.3	Numerical results	62
3.2.3.1	Simulation Scenario	62
3.2.3.2	Results for MAP Framework	63
4	CONCLUSIONS	71
4.1	Future Work	72
	REFERENCES	73

LIST OF TABLES

TABLES

Table 2.1	Scenario parameters	19
Table 2.2	Cost values using ML framework and Condition Number	22
Table 2.3	MSE values using ML framework for PS, MPS, EO for SNR= ∞	23
Table 2.4	MSE values using ML framework for PS, MPS, EO for SNR = 60 dB	23
Table 2.5	MSE values using ML framework for PS, MPS, EO for SNR = 30 dB	24
Table 2.6	MSE values using ML framework for PS, MPS, EO for SNR = 15 dB	24
Table 2.7	Cost and MSE values using MAP framework for PS, MPS, EO for SNR = 60 dB	40
Table 2.8	Cost and MSE values using MAP framework for PS, MPS, EO for SNR = 30 dB	41
Table 2.9	Cost and MSE values using MAP framework for PS, MPS, EO for SNR = 15 dB	47
Table 2.10	Cost values for ML and MAP frameworks	50
Table 3.1	Scenario parameters	57
Table 3.2	Cost and MSE values using MAP framework for PS, MPS, EO for SNR = 30 dB	58
Table 3.3	Cost and MSE values using MAP framework for PS, MPS, EO for SNR = 30 dB, $n = 4$	63
Table 3.4	Cost and MSE values using MAP framework for PS, MPS, EO for SNR = 30 dB, $n = 40$	66

LIST OF FIGURES

FIGURES

Figure 1.1 Illustration of a near-field imaging system [1].	2
Figure 1.2 Multistatic imaging system for near-field MIMO imaging [2].	2
Figure 2.1 Matrices used for discrete derivative operation along x (upper), z (middle), and y (lower) directions.	15
Figure 2.2 Initial antenna array configuration: Uniformly distributed initial array (left), randomly distributed initial array (right).	19
Figure 2.3 Known array topologies: rectangular (upper left), Mills Cross (upper right), ring-spiral (bottom)	20
Figure 2.4 Optimal arrays for ML framework: CSBS-designed with uniform initialization (left), CSBS-designed with random initialization (right)	22
Figure 2.5 Central slice, ML results for point scatterer, $\text{SNR}=\infty$: CSBS-designed with uniform initialization (upper left), CSBS-designed with random initialization (upper right), rectangular (middle left), ring-spiral (middle right), Mills Cross (bottom)	25
Figure 2.6 ML results for MPS and EO at $\text{SNR}=\infty$: Central range slice of CSBS-designed with random initialization (upper left), central range slice of rectangular (upper right), central range slice of CSBS-designed with random initialization (lower left), central range slice of rectangular (lower right)	26
Figure 2.7 Central slice, ML results for point scatterer, $\text{SNR} = 60$ dB: CSBS-designed with uniform initialization (upper left), CSBS-designed with random initialization (upper right), rectangular (middle left), Mills Cross (middle right), ring-spiral (bottom)	27

Figure 2.8 Range slice 1, ML results for point scatterer, SNR = 60 dB: CSBS-designed with uniform initialization (upper left), CSBS-designed with random initialization (upper right), rectangular (middle left), Mills Cross (middle right), ring-spiral (bottom)	28
Figure 2.9 Range slice 3, ML results for point scatterer, SNR = 60 dB: CSBS-designed with uniform initialization (upper left), CSBS-designed with random initialization (upper right), rectangular (middle left), Mills Cross (middle right), ring-spiral (bottom)	29
Figure 2.10 ML results for MPS and EO at SNR = 60 dB: Central range slice of CSBS-designed with random initialization (upper left), central range slice of rectangular (upper right), central range slice of CSBS-designed with random initialization (lower left), central range slice of rectangular (lower right)	30
Figure 2.11 Central slice, ML results for point scatterer, SNR = 30 dB: CSBS-designed with uniform initialization (upper left), CSBS-designed with random initialization (upper right), rectangular (middle left), Mills Cross (middle right), ring-spiral (bottom)	31
Figure 2.12 Range slice 1, ML results for point scatterer, SNR = 30 dB: CSBS-designed with uniform initialization (upper left), CSBS-designed with random initialization (upper right), rectangular (middle left), Mills Cross (middle right), ring-spiral (bottom)	32
Figure 2.13 Range slice 3, ML results for point scatterer, SNR = 30 dB: CSBS-designed with uniform initialization (upper left), CSBS-designed with random initialization (upper right), rectangular (middle left), Mills Cross (middle right), ring-spiral (bottom)	33
Figure 2.14 ML results for MPS and EO at SNR = 30 dB: Central range slice of CSBS-designed with random initialization (upper left), central range slice of rectangular (upper right), central range slice of CSBS-designed with random initialization (lower left), central range slice of rectangular (lower right)	34
Figure 2.15 Central slice, ML results for point scatterer, SNR = 15 dB: CSBS-designed with uniform initialization (upper left), CSBS-designed with random initialization (upper right), rectangular (middle left), Mills Cross (middle right), ring-spiral (bottom)	35

Figure 2.16 Range slice 1, ML results for point scatterer, SNR = 15 dB: CSBS-designed with uniform initialization (upper left), CSBS-designed with random initialization (upper right), rectangular (middle left), Mills Cross (middle right), ring-spiral (bottom)	36
Figure 2.17 Range slice 3, ML results for point scatterer, SNR = 15 dB: CSBS-designed with uniform initialization (upper left), CSBS-designed with random initialization (upper right), rectangular (middle left), Mills Cross (middle right), ring-spiral (bottom)	37
Figure 2.18 ML results for MPS and EO at SNR = 15 dB: Central range slice of CSBS-designed with random initialization (upper left), central range slice of rectangular (upper right), central range slice of CSBS-designed with random initialization (lower left), central range slice of rectangular (lower right)	38
Figure 2.19 Virtual arrays for ML: CSBS-designed with uniform initialization (upper left), CSBS-designed with random initialization (upper right), rectangular (middle left), Mills Cross (middle right), ring-spiral (bottom) . . .	39
Figure 2.20 Optimal arrays for ML framework for different image cubes: CSBS-designed with uniform initialization for smaller cube (left), CSBS-designed with uniform initialization for bigger cube (right)	40
Figure 2.21 Optimal designs for MAP framework at SNR of 60 dB: CSBS-designed with uniform initialization (left), CSBS-designed with random initialization (right)	40
Figure 2.22 MAP results for point scatterer at SNR of 60 dB: CSBS-designed with uniform initialization (upper left), CSBS-designed with random initialization (upper right), rectangular (middle left), Mills Cross (middle right), ring-spiral (bottom)	42
Figure 2.23 MAP results for MPS and EO at SNR of 60 dB: Central range slice of CSBS-designed with uniform initialization (upper left), central range slice of rectangular (upper right), central range slice of CSBS-designed with uniform initialization (lower left), central range slice of rectangular (lower right)	43
Figure 2.24 Virtual arrays for MAP at SNR of 60 dB: CSBS-designed with uniform initialization (left), CSBS-designed with random initialization (right)	43
Figure 2.25 Optimal arrays for MAP framework at SNR of 30 dB: CSBS-designed with uniform initialization (left), CSBS-designed with random initialization (right)	44

Figure 2.26 MAP results for PS at SNR of 30 dB: CSBS-designed with uniform initialization (upper left), CSBS-designed with random initialization (upper right), rectangular (middle left), Mills Cross (middle right), ring-spiral (bottom)	45
Figure 2.27 MAP results at SNR of 30 dB: CSBS-designed with uniform initialization, MPS (upper left), rectangular, MPS (upper right), CSBS-designed with uniform initialization, EO (lower left), rectangular, EO (lower right) .	46
Figure 2.28 Virtual arrays for MAP at SNR of 30 dB: CSBS-designed with uniform initialization (left), CSBS-designed with random initialization (right)	46
Figure 2.29 Optimal designs for MAP framework at SNR of 15 dB: CSBS-designed with uniform initialization (left), CSBS-designed with random initialization (right)	47
Figure 2.30 MAP results for point scatterer at SNR of 15 dB: CSBS-designed with uniform initialization (upper left), CSBS-designed with random initialization (upper right), rectangular (middle left), Mills Cross (middle right), ring-spiral (bottom)	48
Figure 2.31 MAP results at SNR of 15 dB: CSBS-designed with random initialization for MPS (upper left), rectangular for MPS (upper right), CSBS-designed with random initialization for EO (lower left), rectangular for EO (lower right)	49
Figure 2.32 Virtual arrays for MAP at SNR of 15 dB: CSBS-designed with uniform initialization (left), CSBS-designed with random initialization (right)	49
Figure 3.1 Array geometry for synthetic aperture implementation	56
Figure 3.2 Initial configuration for synthetic aperture at one array plane location: Uniform initial distribution (left), random initial distribution (right) .	57
Figure 3.3 Optimal arrays for MAP framework at SNR of 30 dB: CSBS-designed with uniform initialization (left), CSBS-designed with random initialization (right)	58
Figure 3.4 MAP results for point scatterer at SNR of 30 dB: CSBS-designed with uniform initialization (left), CSBS-designed with random initialization (right)	58

Figure 3.5	MAP results at SNR of 30 dB: CSBS-designed with uniform initialization, PS (upper left), CSBS-designed with uniform initialization from previous chapter, PS (upper right), CSBS-designed with uniform initialization, MPS (middle left), CSBS-designed with uniform initialization from previous chapter, MPS (middle right), CSBS-designed with uniform initialization, EO (bottom left), CSBS-designed with uniform initialization from previous chapter, EO (bottom right)	59
Figure 3.6	Virtual arrays for MAP at SNR of 30 dB: CSBS-designed with uniform initialization (left), CSBS-designed with random initialization (right)	60
Figure 3.7	3D Spherical Coordinate System [3].	61
Figure 3.8	Normalized antenna beam patterns for different n values: $n = 4$ (left), $n = 40$ (right)	62
Figure 3.9	Optimal arrays for MAP framework, $n = 4$: CSBS-designed with uniform initialization (left), CSBS-designed with random initialization (right)	63
Figure 3.10	MAP results, $n = 4$ for PS: CSBS-designed with uniform initialization (upper left), CSBS-designed with random initialization (upper right), rectangular (middle left), Mills Cross (middle right), ring-spiral (bottom) .	64
Figure 3.11	MAP results, $n = 4$: CSBS-designed with uniform initialization, MPS (upper left), rectangular, MPS (upper right), CSBS-designed with uniform initialization, EO (lower left), rectangular, EO (lower right)	65
Figure 3.12	Virtual arrays for MAP framework, $n = 4$: CSBS-designed with uniform initialization (left), CSBS-designed with random initialization (right)	65
Figure 3.13	Optimal arrays for MAP framework, $n = 40$: CSBS-designed with uniform initialization (left), CSBS-designed with random initialization (right)	66
Figure 3.14	MAP results, $n = 40$ for PS: CSBS-designed with uniform initialization (upper left), CSBS-designed with random initialization (upper right), rectangular (middle left), Mills Cross (middle right), ring-spiral (bottom)	67
Figure 3.15	MAP results, $n = 40$: CSBS-designed with random initialization, MPS (upper left), rectangular, MPS (upper right), CSBS-designed with random initialization, EO (lower left), rectangular, EO (lower right)	68

Figure 3.16 Virtual arrays for MAP framework, $n = 40$: CSBS-designed with uniform initialization (left), CSBS-designed with random initialization (right) 68

Figure 3.17 Best optimal arrays for MAP framework: $n = 4$ (left), $n = 40$ (right) 69

LIST OF ABBREVIATIONS

1-D	One Dimensional
2-D	Two Dimensional
3-D	Three Dimensional
MIMO	Multiple Input Multiple Output
SAR	Synthetic Aperture Radar
DBF	Digital Beamforming
PSL	Peak to Side Lobe
MSE	Mean Squared Error
CSBS	Clustered Sequential Backward Selection
DDO	Discrete Derivative Operator
PSF	Point-Spread Function
ML	Maximum Likelihood
MAP	Maximum a Posteriori
PDF	Probability Distribution Function
PS	Point Scatterer
MPS	Multiple Point Scatterers
EO	Extended Object

CHAPTER 1

INTRODUCTION

1.1 Wideband Near-Field MIMO Imaging

Near-field ultrawideband imaging systems are emerging array-based systems for various applications such as airport security, surveillance, through-wall imaging and medical diagnosis. For example, such systems are currently used for security screening to detect concealed weapons, explosives and metal objects [4, 5, 6]. Because there is a dielectric contrast difference between healthy and abnormal biological tissues, near-field radar imaging have also been studied for the diagnosis of certain diseases such as breast cancer and brain stroke [7, 8, 9]. Through-wall imaging is another radar-based application for near-field imaging. With these imaging systems, it becomes possible to determine the layouts of a building from outside, and detect or track humans and moving objects inside [10].

In wideband near-field imaging systems, down-range and cross-range resolutions are determined by the frequency bandwidth and size of the antenna arrays. In the classical two-dimensional designs, element spacing is chosen as at most half of the center wavelength to prevent undesired grating lobes. As a result, in applications demanding high-resolution, classical (non-sparse) planar arrays require large number of antenna elements, and this results in high hardware complexity and cost.

To reduce this complexity and cost, recently, there has been increasing interest in using sparse multiple-input-multiple-output (MIMO) arrays [2, 11]. MIMO imaging systems operating at a wide frequency range can offer high resolution with reduced hardware complexity and cost. A typical near-field MIMO imaging system is illus-

trated in Fig. 1.1. As seen in the figure, the system is composed of two main components: “sensors” consisting of antenna elements and “data processing” that performs the image reconstruction from the raw radar data.



Figure 1.1: Illustration of a near-field imaging system [1].

First, the transmit antenna elements transmit a radar pulse and the receiver antennas receive the reflected pulse from the unknown scene. This is often performed with a multistatic system; that is, transmission and reception are performed by different antenna elements unlike a monostatic system. For example, conventional wideband synthetic-aperture radar (SAR) systems are commonly monostatic [5, 12, 13], whereas wideband MIMO imaging systems are multistatic. A typical imaging geometry for the multistatic case is shown in Fig. 1.2. In this thesis, a similar MIMO planar array imaging system is utilized.

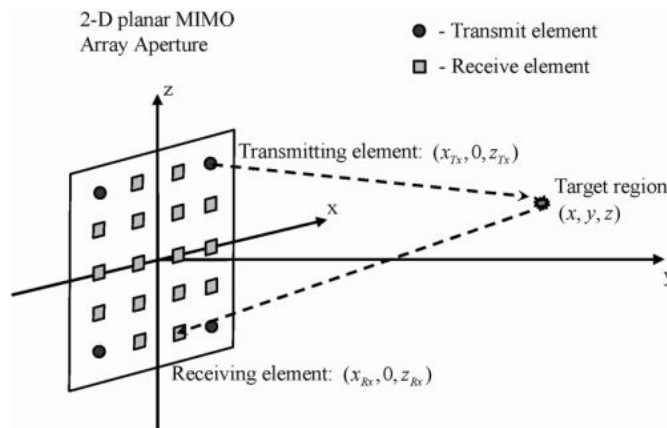


Figure 1.2: Multistatic imaging system for near-field MIMO imaging [2].

The second part of the MIMO imaging system is related to the algorithms used for data processing. An image is computationally formed from radar data by using an image reconstruction algorithm. For this purpose, many algorithms have been developed. Due to the difference in the locations of transmitters and receivers in the multistatic systems, the algorithm used for solving the inverse problem also changes. For

these systems, algorithms developed for monostatic systems are generally extended to the multistatic case. Stack migration, Kirchoff migration and modified range migration are the examples for such extensions [2, 11, 14, 15]. In the inverse problem community, statistical inversion methods are generally preferred over such analytical reconstruction methods. This is because statistical methods enable to regularize the ill-posed inverse problems and offer improved image reconstruction quality in the presence of noise and limited data [16]. In this thesis, statistical inversion methods are utilized to perform image reconstruction.

The operating frequency range of near-field MIMO imaging systems is another important factor. The higher the operating frequency and the bandwidth of the system, the better is the cross-range and down-range resolutions of the system, respectively. Thus, operating frequency range should be selected based on the system requirements. Wavelengths are generally in the order of millimeters or centimeters for the studied near-field imaging systems. For example, the operating frequency spans the range from 300 MHz to 30 GHz (corresponding to cm-wave radar) in [2, 11], and changes from 30 GHz to 300 GHz (corresponding to mm-wave radar) in [17]. Moreover, the operating frequency can also reach up to 1 THz for some applications [18].

1.2 Design of Wideband Near-Field MIMO Imaging Systems

With the increasing interest in using sparse MIMO arrays for imaging, the design of the sparse imaging arrays has become important. The design approaches studied in the literature are generally based on some desired properties of the virtual arrays and beam patterns.

For example, in [19, 20, 21, 22], sparse arrays have been designed by imposing some constraints on the beam pattern such as achieving a desired array radiation pattern, narrow main lobe width and/or low side lobe level. In most of these works, the design starts with a fully sampled non-sparse array, and the reduction of antenna elements are performed until either a predefined number of array elements is reached or the number of elements is minimized. Different non-iterative and iterative methods such as matrix pencil method, simulated annealing, and Bayesian compressive sensing are

applied to the resulting optimization problem, each demanding different amount of computations. These works generally focus on a single operating frequency rather than a wideband operation, and imaging quality is not of special interest.

There are also design approaches that take into account the imaging performance in an *indirect* way through the use of virtual arrays [23, 24]. The virtual array of an antenna configuration is mainly the morphological convolution of the locations of the transmit and receive antenna elements, and is also related to the concept of effective aperture. It has been proposed that the uniformity of the elements in the virtual array of an antenna configuration affects the imaging performance positively. Moreover, minimal element shadowing also improves the imaging quality. The proposed arrays in [11, 25, 23, 24, 26] are mainly based on the uniformity and minimal element shadowing of their virtual arrays, and the performance of the proposed arrays are then compared with the classical array configurations for imaging applications.

The virtual array concept used in the design of sparse MIMO arrays is mainly based on the idea of *co-arrays* [27]. In far-field imaging, the sum and difference coarrays determine the family of realizable point-spread functions (PSFs) associated with an antenna array, as well as the support of the inverse transform of the PSF. There are various works that aim to develop a design theory for maximizing the degrees of freedom (number of unique virtual sensors) in the co-array. These streams of works can be grouped into two categories: nested arrays [28, 29, 30] and coprime arrays [31, 32, 33, 34, 35]. The developed design approaches are for both 1D arrays and 2D arrays, are applicable to both active (as in MIMO radars) and passive sensing, and generally yield uniform and non-overlapping elements in the coarray. Moreover, the performance of the resulting sparse array designs have been shown to improve direction-of-arrival (DOA) estimation for a large number of targets in the field of view when operated at a narrow band. However, although the concept of *co-array* is directly related to the imaging performance for far-field conditions and narrowband operation [27], to the best of our knowledge, no such relation is known for near-field and wideband imaging. Hence, these design criteria based on the concepts of coarrays or virtual arrays appear to affect the imaging performance in an *indirect* way.

To summarize, none of the earlier design approaches for wideband near-field imaging

aim to minimize the image reconstruction error. In fact, a systematic approach to the optimal design of MIMO arrays has not been developed from an inverse theoretic perspective which takes into account the quality of the reconstructed images obtained with the design.

In this thesis, based on a statistical framework, an optimal design method is presented for two-dimensional MIMO arrays in wideband near-field imaging. The problem of image reconstruction from MIMO measurements is formulated as an estimation problem, and different optimality criteria are defined based on the image reconstruction errors obtained with the final design. An algorithm called clustered sequential backward selection is used to perform the optimization of the chosen criterion over all initial locations of antenna elements. That is, the algorithm starts with an initial antenna configuration (either a uniform or a random configuration), and iteratively reduces the antenna elements based on the chosen optimality criterion until the desired number of elements is reached.

To the best of our knowledge, such a statistical approach has not been applied to the optimal design of wideband near-field MIMO imaging systems before. The developed design framework is also flexible; it allows incorporating different practical considerations into the design such as synthetic apertures and antenna patterns. Existing design approaches do not also provide such flexibility. This work also illustrates the performance of ML- and MAP-based image reconstruction (or equivalently least-squares (LS) and Tikhonov-regularized LS solutions) for wideband near-field MIMO imaging.

The performance of the designs obtained with our approach is illustrated for a microwave imaging application. The designs obtained for different observation settings are compared with some commonly used sparse array configurations in terms of image reconstruction quality. Numerical simulation results suggest that the approach can yield designs that outperform conventional sparse array configurations in terms of image reconstruction quality for a wide range of SNR.

1.3 Contributions and Outline

The thesis is organized as follows. In Chapter 2, the statistical optimal design method is developed. In Sect. 2.1, first, the continuous observation model for wideband near-field MIMO imaging is derived, and the discretization of this forward model is presented. In Sect. 2.2, using this forward model, the problem of image reconstruction from MIMO measurements is formulated using maximum likelihood (ML) and maximum posterior (MAP) estimation principles. Then, an optimality criterion, which is a function of the error covariance matrix, is defined to maximize the image reconstruction quality obtained with the design. Lastly, the algorithm used to perform the optimization of the chosen criterion is presented. In Sect. 2.3, a simulation scenario for microwave imaging is described, and numerical results are presented to illustrate the performance of optimized designs. To perform comparison, ML and MAP based image reconstruction for classical designs are also computed and compared with that of optimized designs in terms of image reconstruction quality.

Chapter 3 focuses on practical design aspects such as enforcing a synthetic aperture and including an antenna pattern to the formulation. In Sect. 3.1, the synthetic aperture concept is considered, and continuous and discrete observation models are modified for this purpose. Numerical simulations are performed for designs with a specific synthetic aperture structure, and results are presented. In Sect. 3.2, the inclusion of the antenna pattern to the observation model is first presented and then numerical simulations are performed for designs with different antenna patterns.

Finally, Chapter 4 concludes this work by summarizing the contributions, results and their implications, as well as the future work.

CHAPTER 2

OPTIMAL DESIGN OF SPARSE MIMO ARRAYS BASED ON A STATISTICAL FRAMEWORK

In the classical two-dimensional designs, element spacing is chosen as at most half of the shortest wavelength to eliminate undesired grating lobes. As a result, in applications demanding high-resolution, classical (non-sparse) planar arrays require high hardware complexity and cost. To reduce this complexity and cost, recently, there has been increasing interest in using sparse multiple-input-multiple-output (MIMO) arrays in ultrawideband radar imaging applications. Many such sparse MIMO topologies have been suggested and tested for this purpose [24, 25, 26, 36]. The arrays have been designed based on some desired properties of the virtual arrays such as uniformity and minimal element shadowing. However, a systematic approach to the optimal design of MIMO arrays has not been developed from an inverse problem perspective which takes into account the quality of the reconstructed images obtained with the design.

In this chapter, optimal design of sparse MIMO arrays based on a statistical framework is presented. Firstly, continuous and discrete observation models for the imaging system and the corresponding inverse problem are formulated. Secondly, the statistical framework is introduced, the design cost is formulated based on the estimation error, and the optimization method is described. Then, the simulation scenarios are presented and the imaging performance of the designed MIMO arrays are analyzed. Moreover, the performance of the designed MIMO arrays are compared with that of the classical MIMO designs in terms of image reconstruction quality.

2.1 Observation Model for Wideband Near-Field MIMO Imaging

The continuous observation model and its corresponding discrete form are presented in Sect. 2.1.1 and in Sect 2.1.2, respectively.

2.1.1 Continuous Observation Model

The main goal here is to mathematically relate the reflectivity of the scene to the measurements obtained with the MIMO imaging system. The transmitter and receiver antennas are placed on a planar plane located at $(x, 0, z)$. In the MIMO imaging system one transmitter and one receiver pair is active at each time. The continuous observation model can be formulated in the time domain as follows:

$$s(x_t, z_t, x_r, z_r, t) = \int_x \int_y \int_z \frac{1}{4\pi d_t d_r} f(x, y, z) p(t - \frac{d_t}{c} - \frac{d_r}{c}) dx dy dz \quad (2.1)$$

where

$$d_t = \sqrt{(x_t - x)^2 + y^2 + (z_t - z)^2}, \quad (2.2)$$

$$d_r = \sqrt{(x_r - x)^2 + y^2 + (z_r - z)^2}. \quad (2.3)$$

Here x , y and z denote the spatial positions, $f(x, y, z)$ is the three-dimensional reflectivity distribution of the scene, and $s(x_t, z_t, x_r, z_r, t)$ denotes the measurement obtained using the transmitter located at $(x_t, 0, z_t)$ and the receiver located at $(x_r, 0, z_r)$. Also d_t and d_r respectively represent the distances from the corresponding transmitter and receiver antenna element to a position (x, y, z) in the scene. Moreover, $p(t)$ is the waveform of the transmitted signal, and c and t denote the speed of the light and the time variable, respectively [2].

By applying Fourier transform, the observation model can be obtained in the temporal frequency domain as follows:

$$s(x_t, z_t, x_r, z_r, k) = \int_x \int_y \int_z \frac{1}{4\pi d_t d_r} f(x, y, z) p(k) e^{-jk d_t} e^{-jk d_r} dx dy dz \quad (2.4)$$

Here the measurements, $s(x_t, z_t, x_r, z_r, k)$, are expressed in the temporal frequency domain with f denoting the frequency and $k = 2\pi f/c$ denoting the frequency-wavenumber. Moreover, $p(k)$ represents the Fourier transform of the transmitted pulse.

2.1.2 Discrete Observation Model

The continuous observation model in Eqn. 2.4 relates the reflectivity of the scene to the measurements obtained with the MIMO imaging system. In the inverse problem, the goal is to estimate the unknown scene reflectivity function from the observations. Because the computations will be performed on a computer and discrete set of measurements are available, the continuous observation model needs to be discretized. The measurement obtained with the m th transmitter and n th receiver at the l th frequency step can be obtained as follows:

$$\begin{aligned} s[m, n, l] &= s(x_{t_m}, z_{t_m}, x_{r_n}, z_{r_n}, k_l) \\ &= \int_x \int_y \int_z \frac{1}{4\pi d_{t_m} d_{r_n}} f(x, y, z) p(k_l) e^{-jk_l d_{t_m}} e^{-jk_l d_{r_n}} dx dy dz \end{aligned} \quad (2.5)$$

Here, m, n, l take the values $1 \leq m \leq M$, $1 \leq n \leq N$ and $1 \leq l \leq L$, respectively, and k_l denotes the l th frequency wavenumber. Hence the continuous observations, $s(x_{t_m}, z_{t_m}, x_{r_n}, z_{r_n}, k_l)$, are now in discrete form given by $s[m, n, l]$.

Apart from the observations, the unknown scene reflectivity function also needs to be discretized. This can be done by representing $f(x, y, z)$ in a proper basis:

$$f(x, y, z) = \sum_{q=1}^Q f_q \Phi_q(x, y, z) \quad (2.6)$$

where $\Phi_q(x, y, z)$'s are the chosen basis functions, each corresponding to a rectangular function associated with one voxel. Then f_q 's are the representation coefficients corresponding to the voxel values, and Q is the total number of the voxels in the discretized reflectivity function. Using this representation, the relation between the discrete measurements and the voxel values is obtained as follows:

$$s[m, n, l] = \sum_{q=1}^Q f_q \int_x \int_y \int_z \frac{1}{4\pi d_{t_m} d_{r_n}} \Phi_q(x, y, z) p(k_l) e^{-jk_l d_{t_m}} e^{-jk_l d_{r_n}} dx dy dz \quad (2.7)$$

Using lexicographic ordering, the measurements can be cast in vector form y , i.e. $y_i = s[m(i), n(i), l(i)]$ where $i = 1, \dots, MNL$. That is, the i th measurement in the vector y corresponds to the measurement obtained with $m(i)$ th transmitter and

$n(i)$ th receiver at the $l(i)$ th frequency index. After mapping the three-dimensional measurements, s , into a one-dimensional vector, y , the above linear discrete model can be written in matrix-vector form as follows:

$$y_i = \sum_{q=1}^Q A_{iq} f_q \quad (2.8)$$

where

$$A_{i,q} = \int_x \int_y \int_z \frac{1}{4\pi d_{t_m} d_{r_n}} \Phi_q(x, y, z) p(k_l) e^{-jk_l d_{t_m}} e^{-jk_l d_{r_n}} dx dy dz \quad (2.9)$$

By assuming that the observation kernel changes slowly within a voxel, A_{iq} can be approximated as follows:

$$A_{i,q} \approx \frac{p(k_l) e^{-jk_l d_{t_m}^{(q)}} e^{-jk_l d_{r_n}^{(q)}} \Delta x \Delta y \Delta z}{4\pi d_{t_m}^{(q)} d_{r_n}^{(q)}} \quad (2.10)$$

Here $d_{t_m}^{(q)}$ and $d_{r_n}^{(q)}$ represent the distance from the center of the q th voxel to the m th transmitter and n th receiver, respectively. The measurement index i indicates the locations of the transmitting and receiving antennas, as well as the frequency used. The voxel sizes in x , y and z axes are denoted as Δx , Δy and Δz , respectively, and q is the voxel index. Hence (i, q) th element of the observation matrix A represents the contribution of the q th voxel to the i th measurement. The total number of rows in A is equal to the length of the measurement vector, and the number of columns is equal to the length of the reflectivity vector.

The linear forward model above can be completed by including the noise component denoted by w as follows:

$$y = Af + w, \quad (2.11)$$

As mentioned before, A is the observation matrix, f is the reflectivity vector and y is the measurement vector. Denoting the number of receivers, transmitters and frequency steps as M , N , L , respectively, and the number of voxels as Q , the length of the measurement vector, y , is given by $P = MNL$. Thus, the size of the matrix A is given by $P \times Q$.

2.2 Optimal Design Method

In the inverse problem, the goal is to estimate the unknown reflectivity vector f from the noisy measurements y . In this work, a statistical framework is used to formulate the inverse problem. More specifically, the problem of image reconstruction from MIMO measurements is formulated both as a maximum likelihood (ML) and a maximum posterior (MAP) estimation problem. Based on these statistical frameworks, a design approach [37] is presented. The optimality criterion for the design is chosen based on the error covariance matrix with the goal of minimizing image reconstruction error. A greedy optimization algorithm is used to numerically solve the resulting optimization problem.

2.2.1 Statistical Framework

The ML and MAP frameworks used for the inverse problem formulation are described in Sect. 2.2.1.1 and 2.2.1.2, respectively.

2.2.1.1 Maximum Likelihood (ML) Framework

In the ML framework [38], the noise vector is assumed to be complex Gaussian distributed with mean zero as follows:

$$w \sim CN(0, \Sigma_w), \quad (2.12)$$

Here Σ_w denotes the covariance matrix of the noise vector. With f treated as a deterministic quantity, the distribution of the measurement vector is same as that of the noise vector except its mean is shifted by Af :

$$y \sim CN(Af, \Sigma_w), \quad (2.13)$$

Then, to estimate the unknown reflectivity vector f using the maximum likelihood approach, the likelihood function of f is maximized:

$$\hat{f}_{\text{ML}} = \underset{f}{\operatorname{argmax}} p(y|f), \quad (2.14)$$

$$= \frac{e^{-(y-Af)^H \Sigma_w^{-1} (y-Af)}}{\pi^P |\Sigma_w|} \quad (2.15)$$

where $|\cdot|$ denotes the determinant of a matrix and the superscript $(\cdot)^H$ represents the Hermitian of a matrix.

The easy way to maximize the likelihood function is to first take its logarithm to get rid off the exponential term. In fact, the maximization problem is equivalent to the following minimization problem:

$$\begin{aligned} \hat{f}_{\text{ML}} &= \arg \min_f -\log p(y|f), \\ &= \arg \min_f \|y - Af\|_{\Sigma_w^{-1}}^2, \end{aligned} \quad (2.16)$$

When A is full column rank, this problem has a closed-form solution given by

$$\hat{f}_{\text{ML}} = (A^H \Sigma_w^{-1} A)^{-1} A^H \Sigma_w^{-1} y. \quad (2.17)$$

Moreover, by defining the error vector as $e = f - \hat{f}_{\text{ML}}$, the error covariance matrix for this ML estimate is given by [39]

$$\Sigma_e = (A^H \Sigma_w^{-1} A)^{-1}. \quad (2.18)$$

In the special case that noise components are independent and identically distributed (i.i.d.) with variance σ_w^2 , the ML estimate and its error covariance matrix simplifies as follows:

$$\hat{f}_{\text{ML}} = (A^H A)^{-1} A^H y, \quad (2.19)$$

$$\Sigma_e = \sigma_w^2 (A^H A)^{-1}. \quad (2.20)$$

2.2.1.2 Maximum a Posteriori (MAP) Framework

In the MAP framework [40], the unknown reflectivity vector f is also treated as random. The distribution of the reflectivity vector, i.e. the prior distribution, is assumed to be complex Gaussian as follows:

$$f \sim CN(f_0, \Sigma_f), \quad (2.21)$$

where f_0 and Σ_f respectively denote the mean vector and the covariance matrix. To find the MAP estimate of f , the posterior distribution of f is maximized:

$$\hat{f}_{\text{MAP}} = \underset{f}{\operatorname{argmax}} p(f|y), \quad (2.22)$$

By using Bayes' rule, the posterior distribution $p(f|y)$ is expressed as follows:

$$p(f|y) = \frac{p(y|f)p(f)}{p(y)}, \quad (2.23)$$

where $p(y|f)$ denotes the conditional pdf of y given f (equivalently, the likelihood function of the unknown f), $p(f)$ is the prior distribution, and $p(y)$ is the distribution of the measurement vector. Because $p(y)$ does not depend on f , the maximization of $p(f|y)$ over f depends only on $p(y|f)p(f)$. After taking logarithm, the MAP estimation problem becomes

$$\begin{aligned} \hat{f}_{\text{MAP}} &= \underset{f}{\operatorname{argmin}} -\log(p(y|f)) - \log(p(f)). \\ &= \underset{f}{\operatorname{argmin}} \|y - Af\|_{\Sigma_w^{-1}}^2 + \|f - f_0\|_{\Sigma_f^{-1}}^2. \end{aligned} \quad (2.24)$$

Then the MAP estimate of the scene reflectivity vector has a closed-form given by

$$\hat{f}_{\text{MAP}} = f_0 + (A^H \Sigma_w^{-1} A + \Sigma_f^{-1})^{-1} A^H \Sigma_w^{-1} (y - Af_0). \quad (2.25)$$

Moreover, the error covariance matrix for this MAP estimate is given by [39]

$$\Sigma_e = (A^H \Sigma_w^{-1} A + \Sigma_f^{-1})^{-1}. \quad (2.26)$$

In the special case that the noise is assumed to be independent and identically distributed (i.i.d.) with variance σ_w^2 , and the covariance matrix of the reflectivity vector has the form $\Sigma_f = (1/\gamma^2)(L^T L)^{-1}$, the MAP estimate becomes equivalent to the Tikhonov regularized least-squares solution, \hat{f}_{Tik} , [37]:

$$\hat{f}_{\text{Tik}} = \underset{f}{\operatorname{argmin}} \frac{1}{\sigma_w^2} \|y - Af\|_2^2 + \gamma^2 \|L(f - f_0)\|_2^2, \quad (2.27)$$

$$= \underset{f}{\operatorname{argmin}} \|y - Af\|_2^2 + \lambda \|L(f - f_0)\|_2^2, \quad (2.28)$$

$$= f_0 + (A^H A + \lambda L^T L)^{-1} A^H (y - Af_0). \quad (2.29)$$

Its error covariance matrix is then given by

$$\Sigma_e = \left(\frac{1}{\sigma_w^2} A^H A + \Sigma_f^{-1} \right)^{-1}. \quad (2.30)$$

$$= \sigma_w^2 (A^H A + \lambda L^T L)^{-1}. \quad (2.31)$$

where $\lambda = (\gamma\sigma_w)^2$ is the defined regularization parameter.

One possible choice for the transformation matrix L is a discrete derivative operator (DDO) for three dimensional space (x, y, z) . This choice imposes a smoothness constraint on the solution since large changes between consecutive voxel values in x, y and z axes are penalized significantly. Here a first-order discrete approximation to the gradient operator is used as DDO, which results in taking differences between neighboring voxels. This is equivalent to the convolution operation with $[-1 \ 1]$ vector in each direction. Hence, the matrix L is chosen as

$$L = [D_x; D_y; D_z]. \quad (2.32)$$

where the matrices D_x, D_y and D_z are convolution matrices performing convolution with $[-1 \ 1]$ along $x, y,$ and z directions, respectively. The general form of these matrices are as follows:

$$D_x = \begin{bmatrix} D_{subx} & 0\dots 0 & \dots & 0\dots 0 \\ 0\dots 0 & D_{subx} & \dots & 0\dots 0 \\ \vdots & \vdots & \vdots & \\ 0\dots 0 & \dots & 0\dots 0 & D_{subx} \end{bmatrix}, D_{subx} = \begin{bmatrix} 1 & 0 & \dots & 0 & -1 & 0 & \dots & \dots & 0 \\ 0 & 1 & 0 & \dots & 0 & -1 & 0 & \dots & 0 \\ & & \vdots & & \vdots & & \vdots & & \\ 0 & \dots & \dots & 0 & 1 & 0 & \dots & 0 & -1 \end{bmatrix} \quad (2.33)$$

$$D_z = \begin{bmatrix} 1 & -1 & 0 & \dots & \dots & \dots & 0 \\ 0 & 1 & -1 & \dots & \dots & \dots & 0 \\ & & \vdots & \vdots & \vdots & & \\ 0 & \dots & \dots & \dots & 0 & 1 & -1 \end{bmatrix} \quad (2.34)$$

$$D_y = \begin{bmatrix} 1 & 0 & \dots & 0 & \dots & 0 & -1 & 0 & \dots & \dots & \dots & 0 \\ 0 & 1 & 0 & \dots & 0 & \dots & 0 & -1 & 0 & \dots & \dots & 0 \\ & & & \vdots & & \vdots & & \vdots & & & & \\ 0 & \dots & \dots & \dots & 0 & 1 & 0 & \dots & 0 & \dots & 0 & -1 \end{bmatrix} \quad (2.35)$$

These matrices are illustrated in Fig. 2.1 for an image cube of size $7x7x3$.

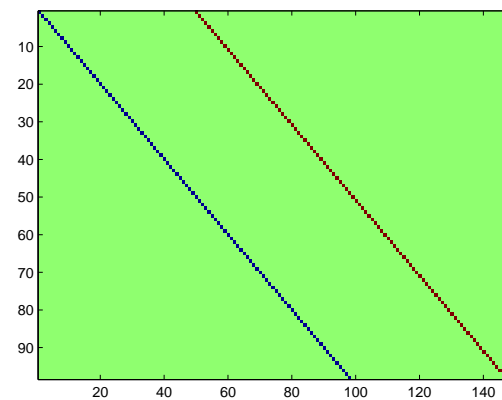
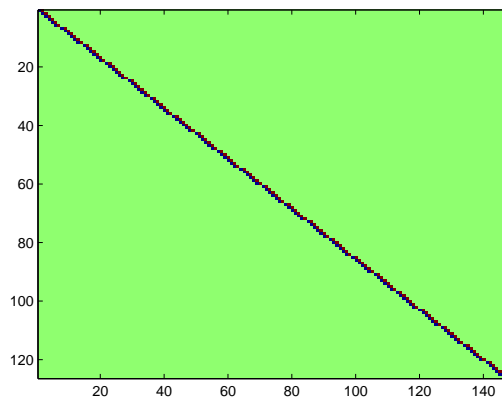
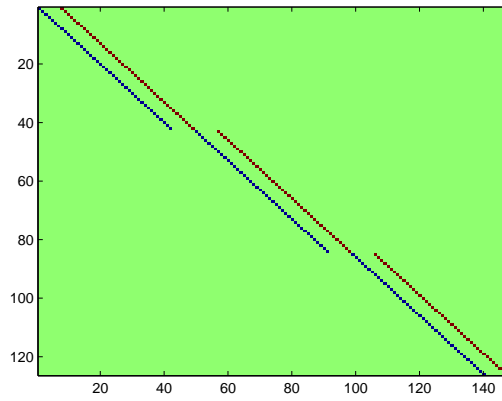


Figure 2.1: Matrices used for discrete derivative operation along x (upper), z (middle), and y (lower) directions.

2.2.2 Cost Formulation Based on Error Covariance Matrix

Having established the statistical frameworks for the inverse problem, we can now define an optimality criterion based on the error covariance matrix with the goal of minimizing image reconstruction error. It is possible to define various different optimality criteria based on Σ_e [37]. Here, we define the cost function for the design as the trace of the error covariance matrix:

$$\text{Cost}(A) = \text{Tr}(\Sigma_e) = \sum_{q=1}^Q (\Sigma_e)_{qq}, \quad (2.36)$$

The closed-form expressions for the error covariance matrix are given earlier for the ML and MAP cases in Eqn. 2.20 and 2.31, respectively. Because the factor σ_w^2 in these equations does not change the result of the cost minimization, the cost functions used for the design optimization are as follows:

$$\text{Cost}(A)_{ML} = \text{Tr}((A^H A)^{-1}), \quad (2.37)$$

$$\text{Cost}(A)_{MAP} = \text{Tr}((A^H A + \lambda L^T L)^{-1}). \quad (2.38)$$

After determining the cost functions for both frameworks, a numerical optimization technique is required to perform design optimization.

2.2.3 Optimization Algorithm

For a given number of antenna elements, the goal in the optimal design is to obtain an array configuration that minimizes the cost function. For this purpose, an algorithm called clustered sequential backward selection (CSBS) [37] is used. The algorithm starts with an initial antenna configuration with large number of antenna elements, and iteratively reduces the antenna elements based on the chosen optimality criterion until the desired number of elements is reached. More specifically, the reduction of the antenna elements corresponds to the elimination of the respective rows from the observation matrix. The optimality criterion is used to identify which rows to eliminate. That is, at each iteration, the cost function of the design resulting after the removal of each antenna element is calculated, and the one that yields the minimum

cost value is removed from the current design. Equivalently, corresponding rows from the observation matrix are eliminated. This process continues until the desired number of antennas is reached for the design.

In order to reduce the computational complexity, the cost function can be replaced with an equivalent but a simpler form [37]. This results in the following faster implementation:

$$\Gamma \leftarrow \Gamma \setminus k^* : k^* = \arg \min_{k \in \Gamma} \sum_{i \in \Pi_k} \frac{a_i \Sigma_e^2 a_i^H}{1 - a_i \Sigma_e a_i^H}, \quad (2.39)$$

Here Γ contains the indices of the antenna elements in the current configuration, and k^* represents the index of the antenna element that is removed from the current configuration. Moreover, a_i shows the i th row of the observation matrix, Π_k contains the row numbers corresponding to the measurements related to the k th antenna. To compute this cost function, matrix Σ_e is required to be updated at each iteration using the current observation matrix A^Γ and Eqn. 2.20 or 2.30 without σ_w^2 term.

Greedy algorithms like CSBS algorithms can only provide suboptimal solutions; that is, it does not guarantee to obtain the optimal solution that minimizes the cost function. At each iteration it makes the optimal decision for the reduction of a single antenna element; however, this does not guarantee to reach the optimal combination of antenna elements that minimizes the overall cost function. Once the best selection is made at the current step, change in the decision is not allowed later on. Hence, although the designs obtained with the CSBS algorithm are sometimes referred as *optimal design* in this thesis, one should note that these designs are inherently suboptimal due to the suboptimality of the CSBS algorithm.

In order to analyze the computational complexity of the CSBS algorithm [40], recall that Σ_e and the summation in Eqn. 2.39 are required to be computed at each iteration. Computation of Σ_e involves matrix multiplication and inversion operations in Eqn. 2.26 but note that the inverse of Σ_f is calculated only once and stored for the rest. Assuming that the number of rows in the updated matrix A^Γ is P^* ($\tilde{P} \leq MNL$), the computational complexity is $O(\tilde{P}^2 Q + Q^2 \tilde{P})$ for the matrix multiplications and $O(Q^3)$ for the matrix inversion. Since $\tilde{P} \geq Q$, the computational complexity of Σ_e calculation becomes $O(\tilde{P}^2 Q)$. Moreover, if the sum of the receiver and transmitter antenna elements is denoted by C ($C = M + N$), then the computational complexity

of the summation in Eqn. 2.39 is $O(Q^2C)$. Hence, the computational complexity of one iteration becomes $O(\tilde{P}^2Q + Q^2C)$. Since $\tilde{P} \geq Q$ and $\tilde{P} \geq C$, computational complexity of one iteration can be expressed as $O(\tilde{P}^2Q)$.

2.3 Numerical Results

The aim of this section is to apply the design method discussed in Sect. 2.2 to some observation scenarios. First, the simulation parameters are presented. Then, the simulation results and their discussions are given. In particular, the performance of the designs obtained with the CSBS algorithm is compared with that of the known array topologies such as uniform rectangular, Mills Cross, and ring-spiral arrays in terms of image reconstruction quality. The comparisons are made separately both for ML and MAP frameworks.

2.3.1 Simulation Scenario

To compare the image reconstruction quality of the CSBS-based array designs with the commonly used sparse arrays [24], a microwave imaging scenario is considered. The parameters used in this scenario are given in Table 2.1. The center frequency and bandwidth are selected as same with [24]. Moreover, the number of frequency steps is selected such that observation matrices become full rank.

For the initial antenna array configurations used in the CSBS algorithm, a large number of antenna elements are distributed uniformly or randomly within the antenna aperture. Sample initial array configurations are shown in Fig. 2.2. Throughout this thesis, for the random case, three different random configurations are used, and the one that gives the smaller design cost is presented as the result. Initial antenna elements are distributed between $-10\lambda_c$ and $10\lambda_c$ in x and z directions, which result in a width of $20\lambda_c$ in both directions for the initial arrays. Moreover, the initial array configuration contains 242 antennas equally shared for receiver and transmitter antennas. The task is to reduce the number of antenna elements to the desired number of 25 using the CSBS algorithm.

Table 2.1: Scenario parameters

Parameter	Value
Center frequency (f_c)	11 GHz
Bandwidth (B)	16.5 GHz
Number of frequency steps (F)	10
Center wavelength (λ_c)	2.73 cm
Number of image cube voxels (x, z, y)	19 x 19 x 3
Voxel size (x, z, y)	$\lambda_c, \lambda_c, \lambda_c$
Physical size of the image cube	$19\lambda_c \times 19\lambda_c \times 3\lambda_c$
Target distance to arrays (R)	$40\lambda_c$
SNR (dB)	60, 30, 15

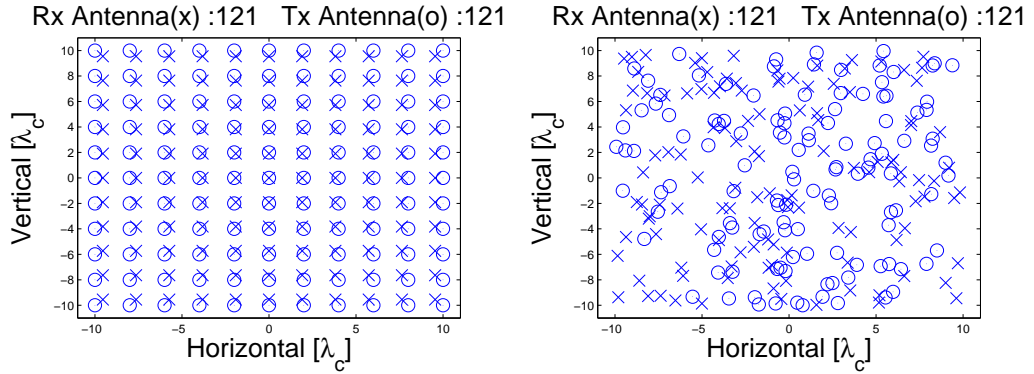


Figure 2.2: Initial antenna array configuration: Uniformly distributed initial array (left), randomly distributed initial array (right).

For uniformly distributed initial antenna array configuration (see Fig. 2.2), the spacing between transmit antennas is set to $\lambda_c/2$. In order to avoid overlapping of the virtual array elements, the spacing between receive antennas is chosen different than $\lambda_c/2$. In fact, the ratio between the spacing's of receive and transmit antennas is chosen as an irrational number of $3/\pi$, while keeping the width of the transmit and receive antenna arrays close to $20\lambda_c$.

To compare the imaging performance of the CSBS-based array designs, uniform rectangular, Mills Cross, and ring-spiral topologies in [24] are considered. These array topologies also have 25 antenna elements, and are shown in Fig. 2.3.

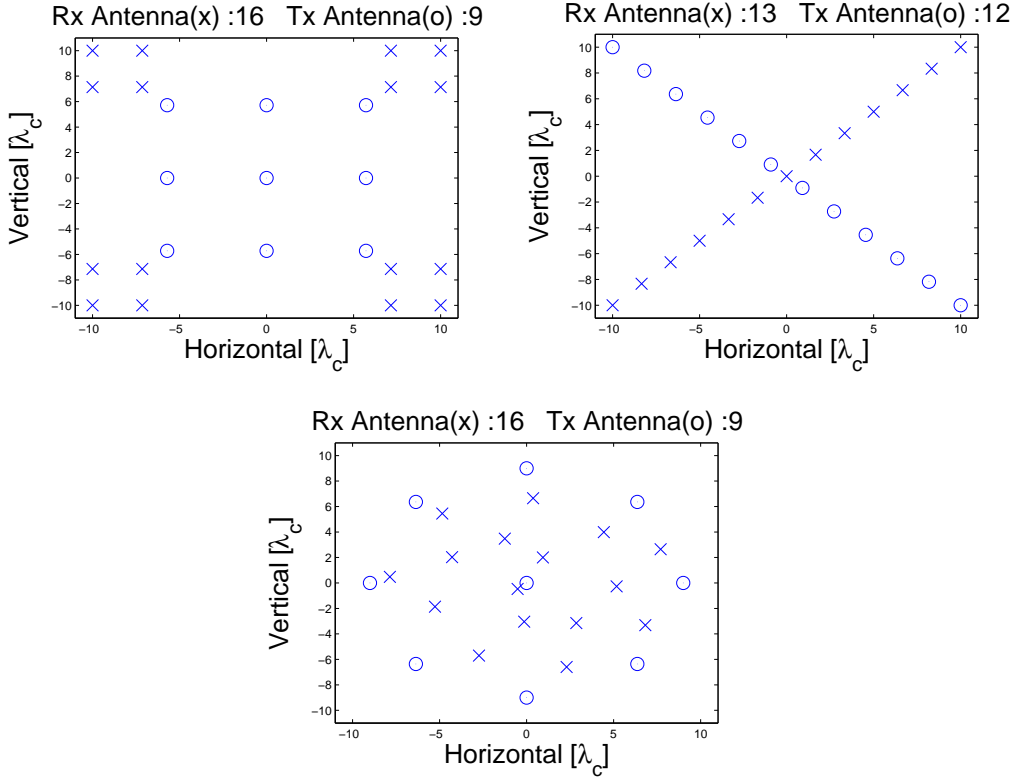


Figure 2.3: Known array topologies: rectangular (upper left), Mills Cross (upper right), ring-spiral (bottom)

The reflectivity cube of interest is divided into $19 \times 19 \times 3$ voxels in the x , z and y directions, respectively. To determine the voxel sizes along each direction, down-range and cross-range resolutions are calculated using the following equations [24]:

$$\delta y = \frac{c}{2B}, \quad \delta x = \delta z = \frac{\lambda_c R}{2W}, \quad (2.40)$$

Here δy is the down-range resolution, and δx and δz are the cross-range resolutions along x and z directions. Using the scenario parameters in Table 2.1, down-range and cross-range resolutions are calculated as $0.33\lambda_c$ and $1\lambda_c$, respectively. Based on these, voxel size is chosen as λ_c in each direction. The physical size of the image cube then becomes $19\lambda_c \times 19\lambda_c \times 3\lambda_c$.

As the test object for the simulations, a point scatterer (PS) at the center of the reflec-

tivity cube is considered as in [24], and the distance from the point scatterer to the antenna array, R , is selected as $40\lambda_c$. Other synthetic test objects used in the simulations are multiple point scatterers (MPS) (consisting of 5 points) and a sample 2D extended object (EO) (in the shape of letter H).

To analyze the imaging performance of different array designs, the elements of the observation matrix is calculated using Eqn. 2.10, and $p(k)$ there is taken as unity. The measurement vector is computed using Eqn. 2.11 and the observation noise w is generated as i.i.d. complex Gaussian. Then the reflectivity vector is reconstructed using both ML and MAP approaches for different types of objects. Specifically, in the MAP case, the reflectivity vector is reconstructed using Eqn. 2.29 (equivalently, Tikhonov regularization), with λ chosen as the optimal regularization parameter and L chosen as the discrete derivative operator described before. Throughout this thesis, the reconstruction results obtained with five different noise realizations are visually checked, and neither the best nor the worst one, but the median one is presented to illustrate the average performance.

For the point scatterer, each range slice of the reconstructed reflectivity cube is provided. In this case, the central slice of the cube provides an effective point-spread function (PSF) for the imaging system. Apart from the central slices, the first and third slices of the reconstructed cube are also provided for PS target to check the cleanliness of these target-free slices. Furthermore, the reconstructions for MPS and EO target types are only given for the best optimal and classical arrays (i.e. for the arrays that give the smallest cost value).

For the generation of the noise, the signal-to-noise ratio (SNR) is chosen as the ratio of the power of noise-free observation to the power of noise [41] as follows:

$$SNR(dB) = 10 \log_{10} \frac{\|Af\|_2^2}{P\sigma_w^2}. \quad (2.41)$$

2.3.2 Simulation Results

2.3.2.1 Results for ML Framework

In this part of the results, ML framework is considered for three different SNR values of 60 dB, 30 dB, and 15 dB. Note that the cost function for the ML-based design does not depend on the noise variance (see Eqn. 2.37); as a result the optimal designs do not depend on SNR. CSBS algorithm is applied on uniformly or randomly distributed initial antenna arrays (see Fig. 2.2) to reduce the number of antenna elements to 25. The array designs obtained with these initializations are provided in Fig. 2.4. The number of receivers and transmitters are respectively 12 and 13 for both designs.

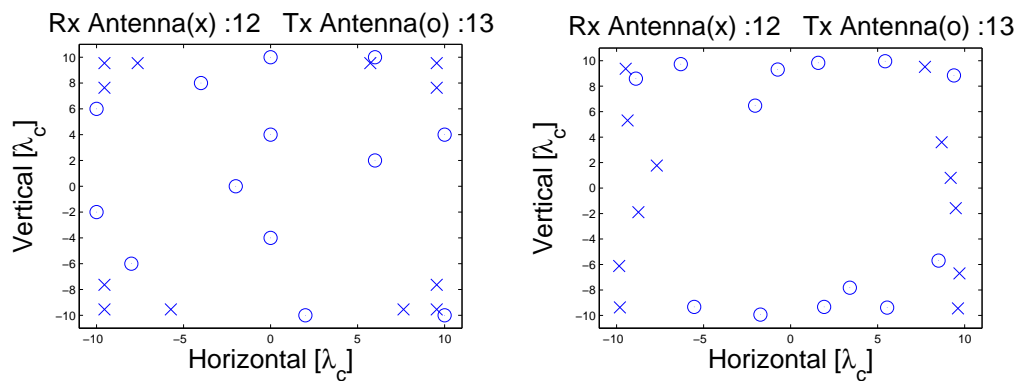


Figure 2.4: Optimal arrays for ML framework: CSBS-designed with uniform initialization (left), CSBS-designed with random initialization (right)

Table 2.2: Cost values using ML framework and Condition Number

Array Type	Cost _{ML}	Cond. Num.
CSBS-designed, initially uniform	1.76e+3	52.7
CSBS-designed, initially random	1.44e+3	42.6
Rectangular	4.28e+5	4.1e+3
Mills Cross	2.60e+7	3.4e+4
Ring-spiral	9.74e+7	6.4e+4

To compare the CSBS-designed arrays with the classical designs, the cost values are calculated for each design using Eqn. 2.37 and provided in Table 2.2. As seen, CSBS-

based designs yield smaller cost value; hence they outperform the classical designs in terms of the cost values. In particular, CSBS-based design with random initialization yields the best result while the rectangular array yields the best result among classical arrays. Condition numbers of the observation matrices for each array type are also provided in Table 2.2. CSBS-based designs also have smaller condition number than classical designs, which means they yield better-conditioned inverse problems, or equivalently less solution sensitivity to errors in the observation vector.

Table 2.3: MSE values using ML framework for PS, MPS, EO for SNR= ∞

Array Type	MSE, PS	MSE, MPS	MSE, EO
CSBS-designed, initially uniform	1.6e-27	7.8e-27	2.6e-25
CSBS-designed, initially random	1.2e-27	5.6e-27	1.1e-25
Rectangular	3.1e-21	1.8e-20	1.5e-18
Mills Cross	1.5e-15	1.6e-15	4.5e-13
Ring-Spiral	2.6e-15	6.7e-15	1.1e-12

Table 2.4: MSE values using ML framework for PS, MPS, EO for SNR = 60 dB

Array Type	MSE, PS	MSE, MPS	MSE, EO
CSBS-designed, initially uniform	6.8e-6	3.5e-5	1.4e-3
CSBS-designed, initially random	5.6e-6	3.0e-5	1.1e-3
Rectangular	1.7e-3	7.9e-3	0.32
Mills Cross	0.11	0.52	24.7
Ring-spiral	0.41	2.13	130.1

To analyze the sensitivity of image reconstruction to noise, image reconstructions are obtained for different designs, test objects and SNR values. For each design, mean square error (MSE) values are calculated for point scatterer (PS), multiple point scatterers (MPS) and extended object (EO) types with 50 Monte Carlo trials. The average of these MSE values is given in Table 2.3, 2.4, 2.5 and 2.6, for the cases that SNR is ∞ , 60 dB, 30 dB, and 15 dB, respectively. (There is no noise component

Table 2.5: MSE values using ML framework for PS, MPS, EO for SNR = 30 dB

Array Type	MSE, PS	MSE, MPS	MSE, EO
CSBS-designed, initially uniform	6.8e-3	3.5e-2	1.4
CSBS-designed, initially random	5.6e-3	3.0e-2	1.1
Rectangular	1.7	7.9	320
Mills Cross	110	520	2.5e+4
Ring-spiral	410	2130	1.3e+5

Table 2.6: MSE values using ML framework for PS, MPS, EO for SNR = 15 dB

Array Type	MSE, PS	MSE, MPS	MSE, EO
CSBS-designed, initially uniform	0.21	1.09	43.3
CSBS-designed, initially random	0.18	0.93	33.5
Rectangular	53.8	249	1.0e+4
Mills Cross	3.4e+3	1.7e+4	7.8e+5
Ring-spiral	1.3e+4	6.7e+4	4.1e+6

used during the reconstruction of the images at SNR= ∞ .) For all object types, the smallest MSE values are obtained for the CSBS-based designs, as expected from the cost values in Table 2.2. The given cost values in this table are Cost_{ML} , hence they do not include the noise variance σ_w^2 term in the original cost function (see Eqn. 2.20 and 2.37). In fact, if the cost value of a specific array in the table is multiplied with the noise variance σ_w^2 used for any object type, the result is nearly the MSE value obtained for that object type. Moreover, the MSE values for each design are increased as the SNR value decreases as expected. It is also observed that MSE values of any array type at any SNR value increase as the object type is changed from PS to EO since MSE is affected from the noise variance σ_w^2 . The noise variance increases as the signal power increases from PS to EO object types, to keep the SNR value same for each object.

Sample image reconstructions are obtained using ML estimation and for different

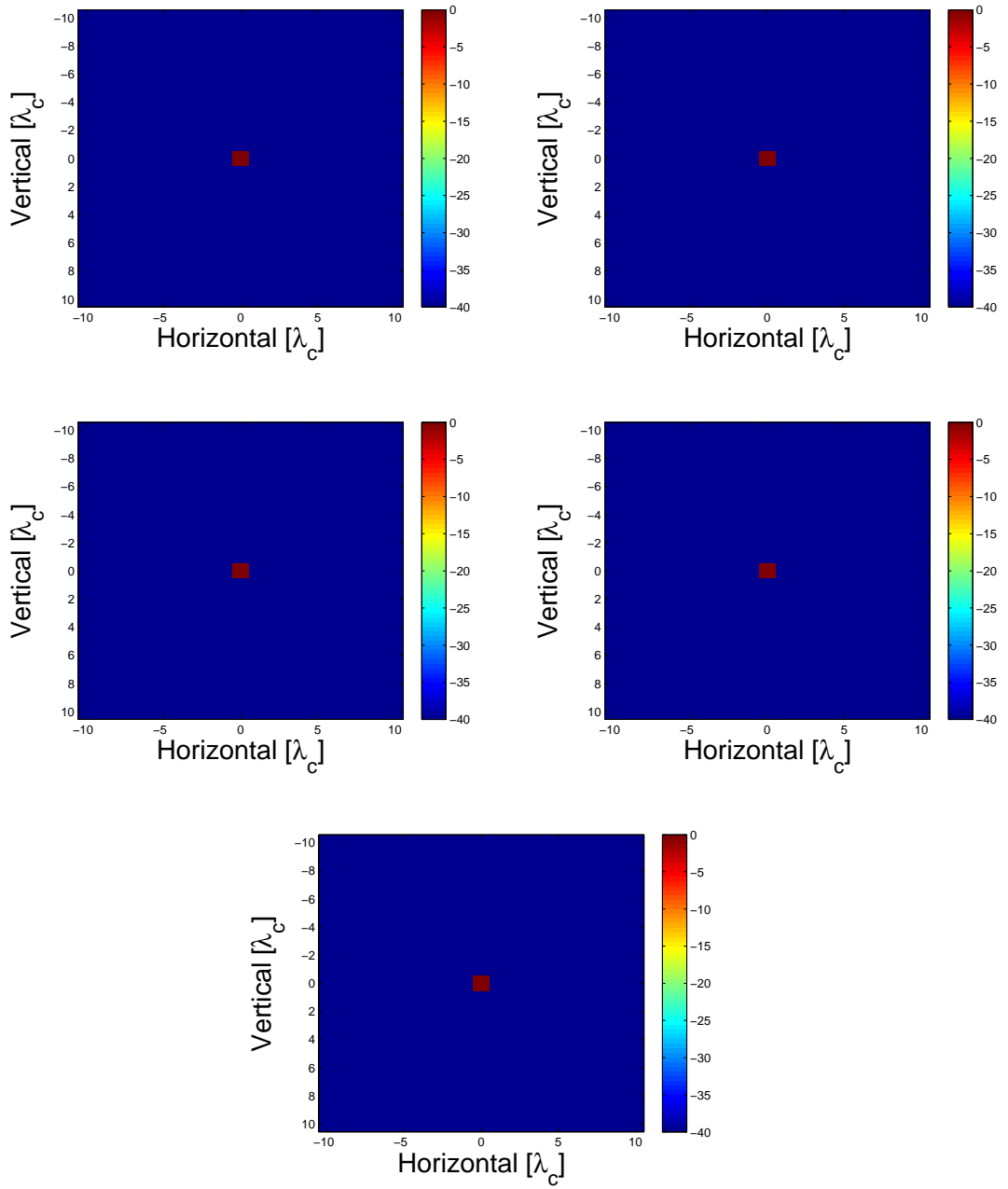


Figure 2.5: Central slice, ML results for point scatterer, $\text{SNR}=\infty$: CSBS-designed with uniform initialization (upper left), CSBS-designed with random initialization (upper right), rectangular (middle left), ring-spiral (middle right), Mills Cross (bottom)

array topologies, object types, and SNRs. These reconstructions are shown in Figures 2.5-2.18, which also illustrate the superiority of the CSBS-designs. To determine which array types are more suitable at a predefined SNR value, it may also help to

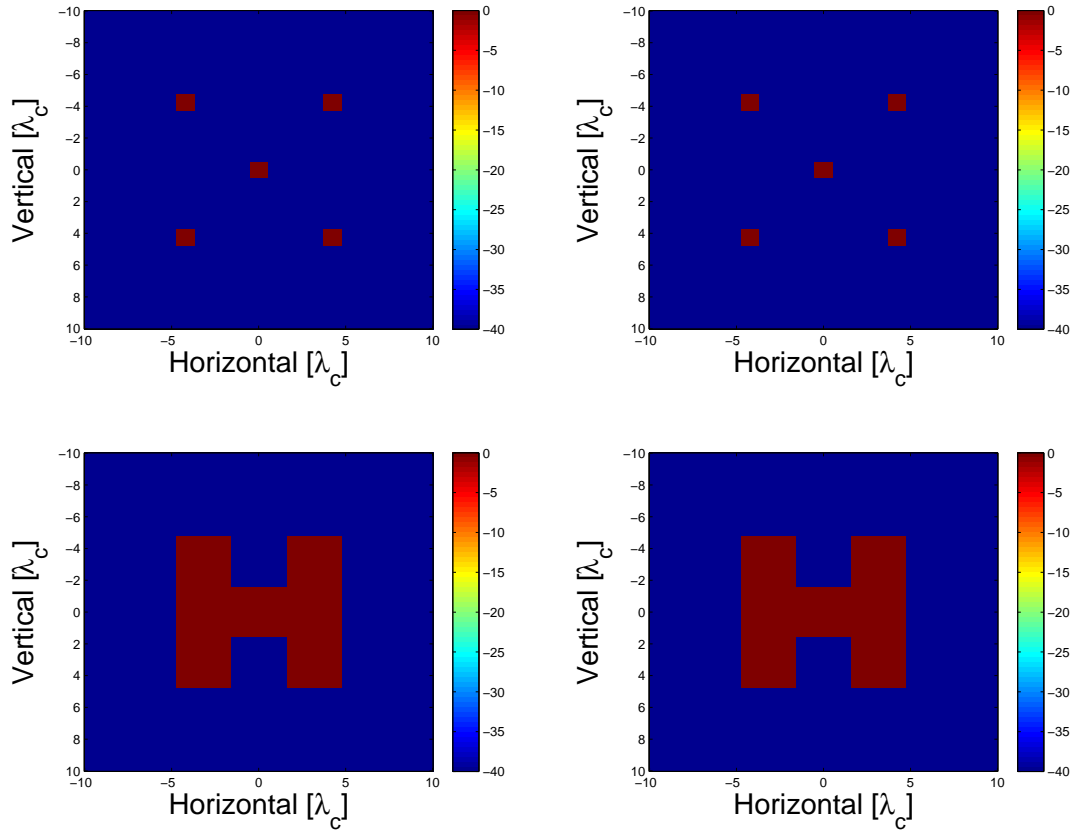


Figure 2.6: ML results for MPS and EO at $\text{SNR}=\infty$: Central range slice of CSBS-designed with random initialization (upper left), central range slice of rectangular (upper right), central range slice of CSBS-designed with random initialization (lower left), central range slice of rectangular (lower right)

check the MSE values and the sample image reconstructions for PS and EO target types. PS target is important since it gives an idea about the effective PSF of the imaging system. EO target is also important since in many applications targets of interest cover much more than a single voxel. MPS target can also be considered as the transition between PS and EO target types in terms of number of nonzero voxels in the target.

For example, Fig. 2.5 shows sample image reconstructions at $\text{SNR}=\infty$ for PS target. Only the central slice of the image cube is shown since the other range slices are completely clean in this noise-free case. Moreover, image reconstruction results for the best optimal and classical arrays are also shown in Fig. 2.6 for MPS and EO targets when $\text{SNR}=\infty$. For this non-realistic case, all array types are suitable for

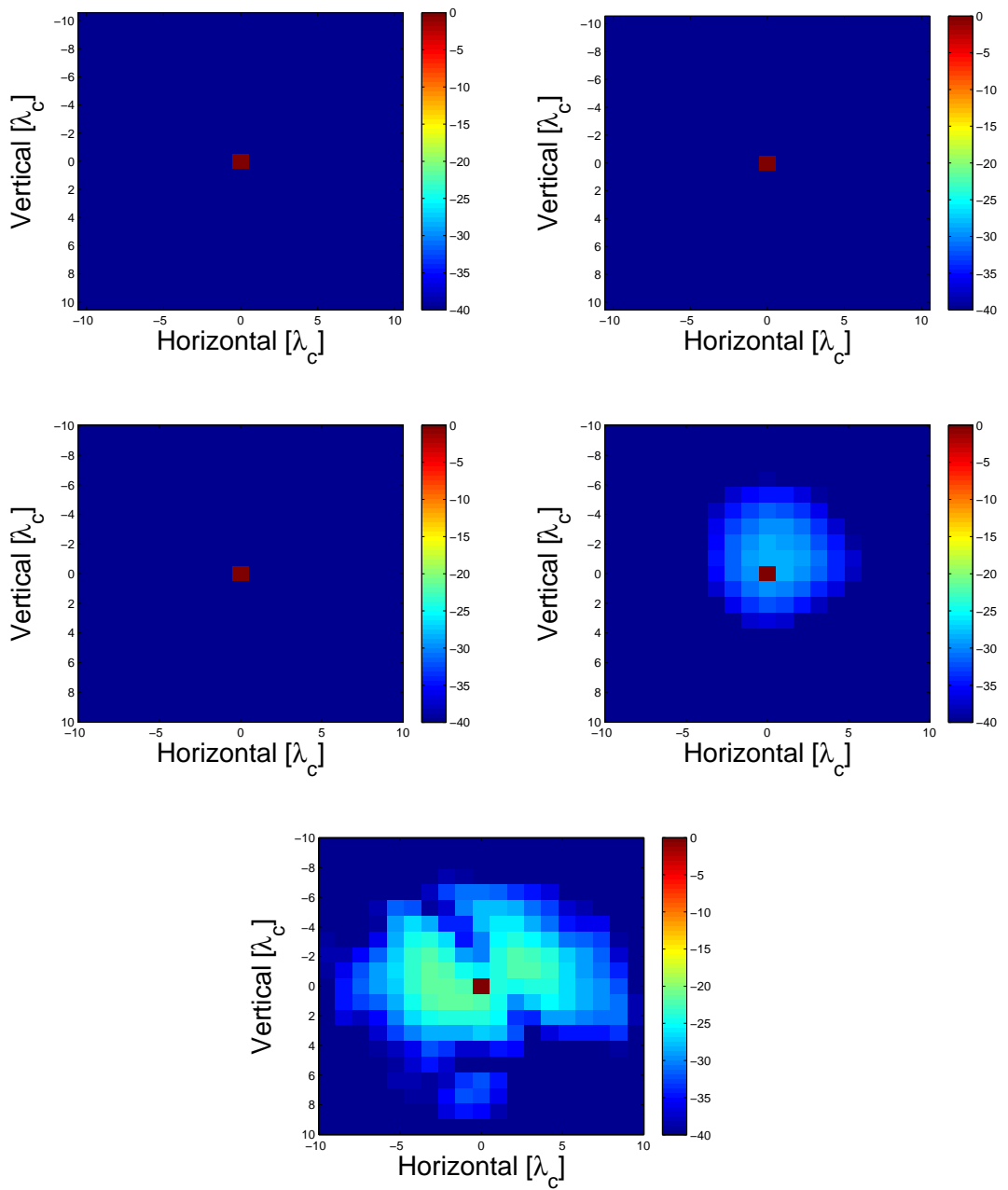


Figure 2.7: Central slice, ML results for point scatterer, SNR = 60 dB: CSBS-designed with uniform initialization (upper left), CSBS-designed with random initialization (upper right), rectangular (middle left), Mills Cross (middle right), ring-spiral (bottom)

operation. They all give faithful reconstructions.

On the other hand, at 60 dB SNR, ring-spiral array does not work properly for the cho-

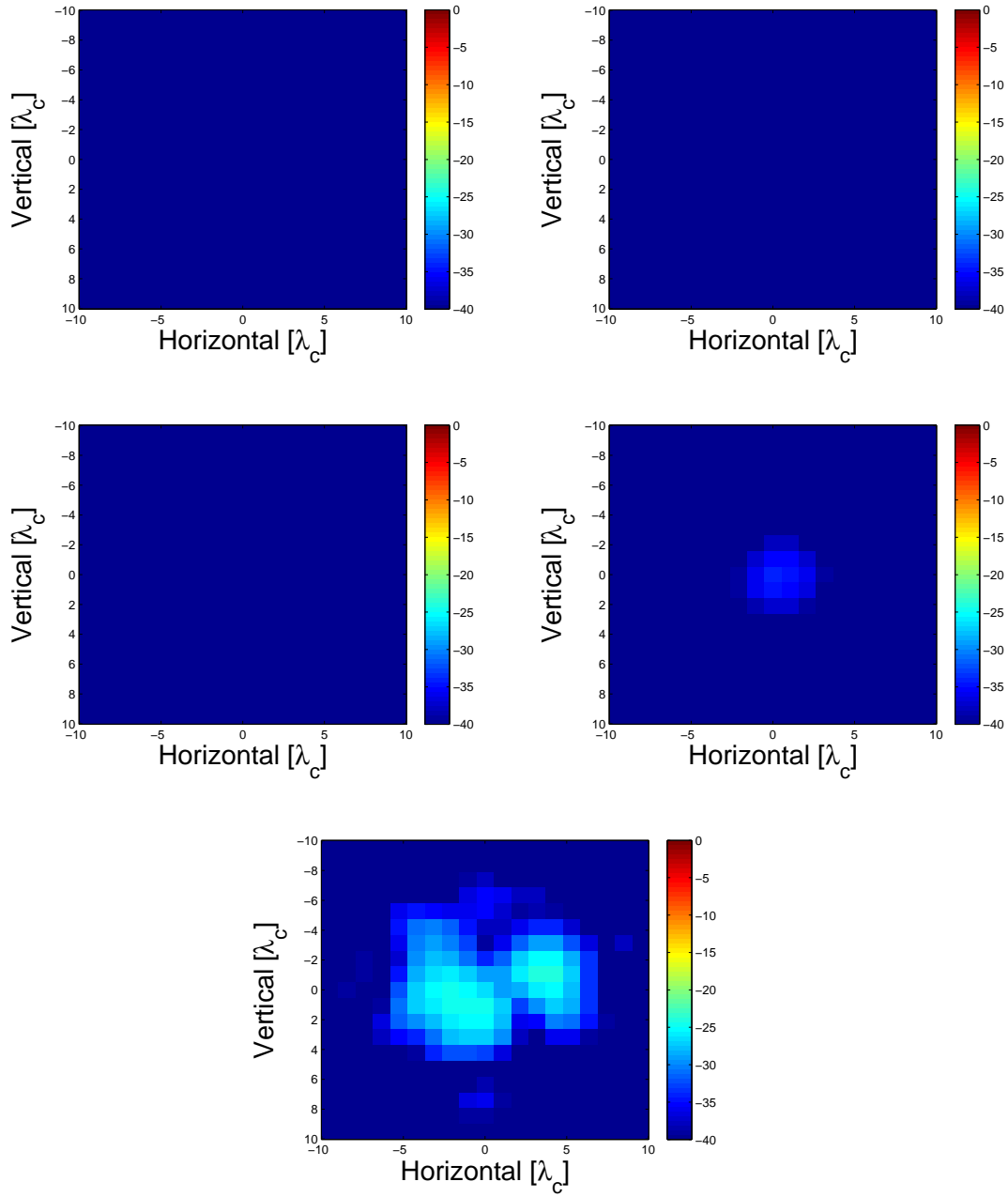


Figure 2.8: Range slice 1, ML results for point scatterer, SNR = 60 dB: CSBS-designed with uniform initialization (upper left), CSBS-designed with random initialization (upper right), rectangular (middle left), Mills Cross (middle right), ring-spiral (bottom)

sen scenario. Image reconstruction results for PS target are provided in Fig. 2.7, 2.8, 2.9. Moreover, image reconstruction results for MPS and EO targets are also shown in Fig. 2.10 for the best optimal and classical arrays. Although the performance of

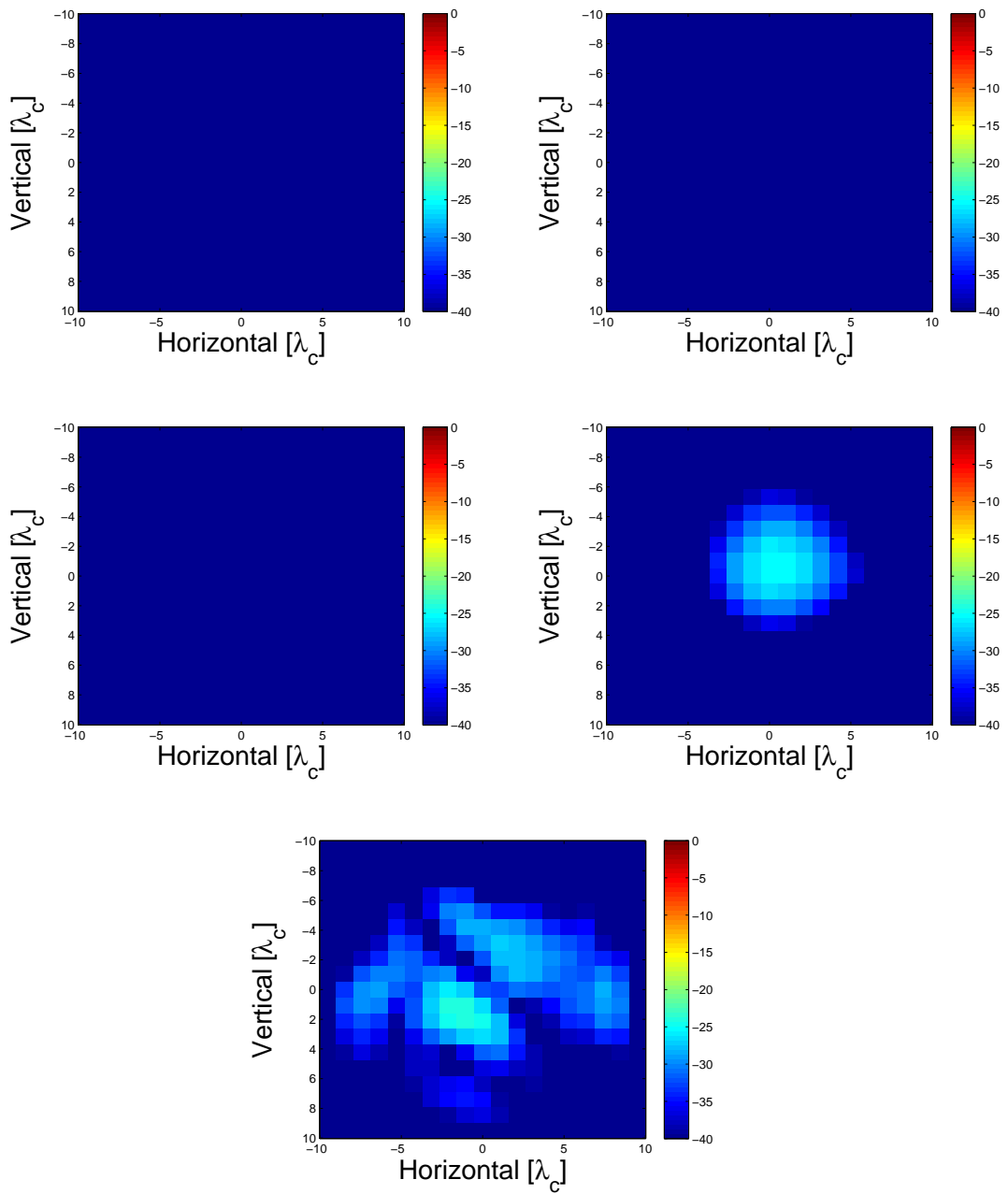


Figure 2.9: Range slice 3, ML results for point scatterer, SNR = 60 dB: CSBS-designed with uniform initialization (upper left), CSBS-designed with random initialization (upper right), rectangular (middle left), Mills Cross (middle right), ring-spiral (bottom)

CSBS-designs and rectangular array appears to be similar for PS and MPS targets, the performance of the rectangular array is actually worse than the CSBS-design as can be seen from the MSE values in the Table 2.4. This is due to the used dynamic

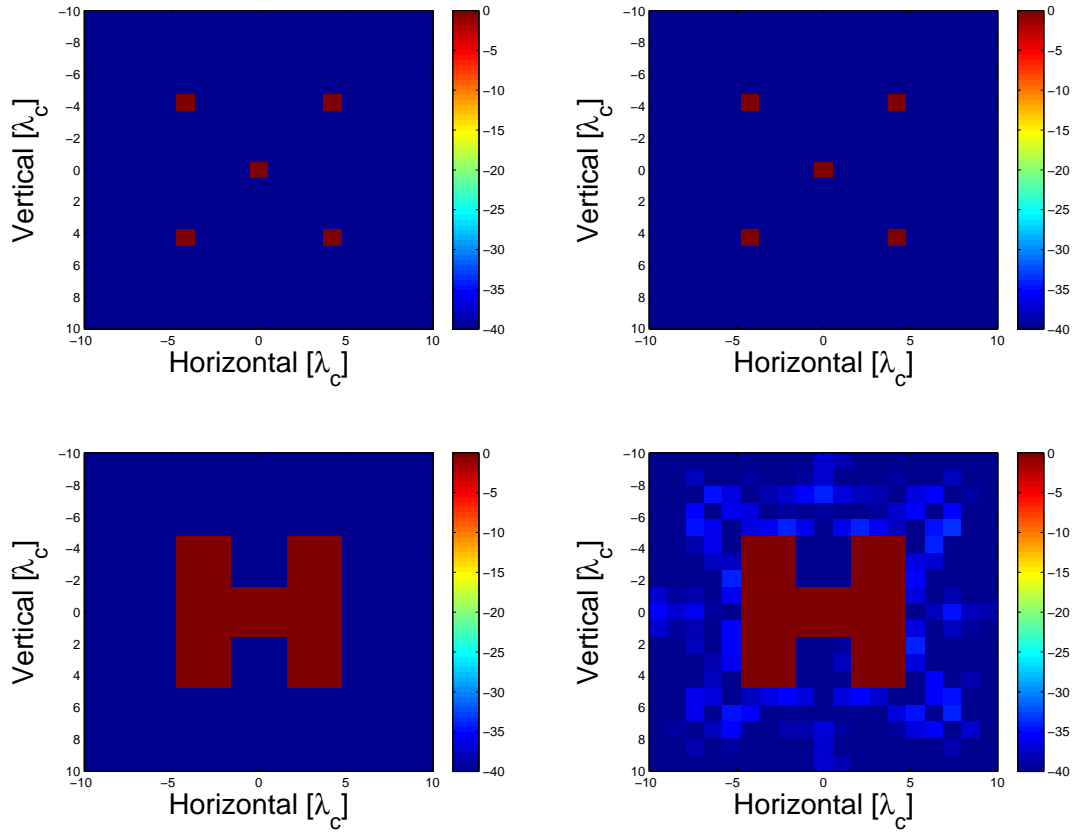


Figure 2.10: ML results for MPS and EO at SNR = 60 dB: Central range slice of CSBS-designed with random initialization (upper left), central range slice of rectangular (upper right), central range slice of CSBS-designed with random initialization (lower left), central range slice of rectangular (lower right)

range of 0 to -40 dB in the figures; that is, the structures that have smaller value than -40 dB are not visible in the figures.

Image reconstruction results at 30 dB SNR is provided in Fig. 2.11, 2.12, and 2.13 for the PS target, and in Fig. 2.14 for the MPS and EO targets. At 30 dB SNR, none of the classical arrays do work properly since their MSE values are very high for each target type. This can also be seen from Fig. 2.14. The reconstruction for the EO type has too many artifacts even for the best classical design, while the MPS target rarely gives faithful reconstructions, but the quality of the reconstruction tends to change significantly with different noise realizations. Neither the worst nor the best reconstructions are provided as mentioned before. On the other hand, the CSBS-designed arrays are still capable of working properly at 30 dB SNR for each target

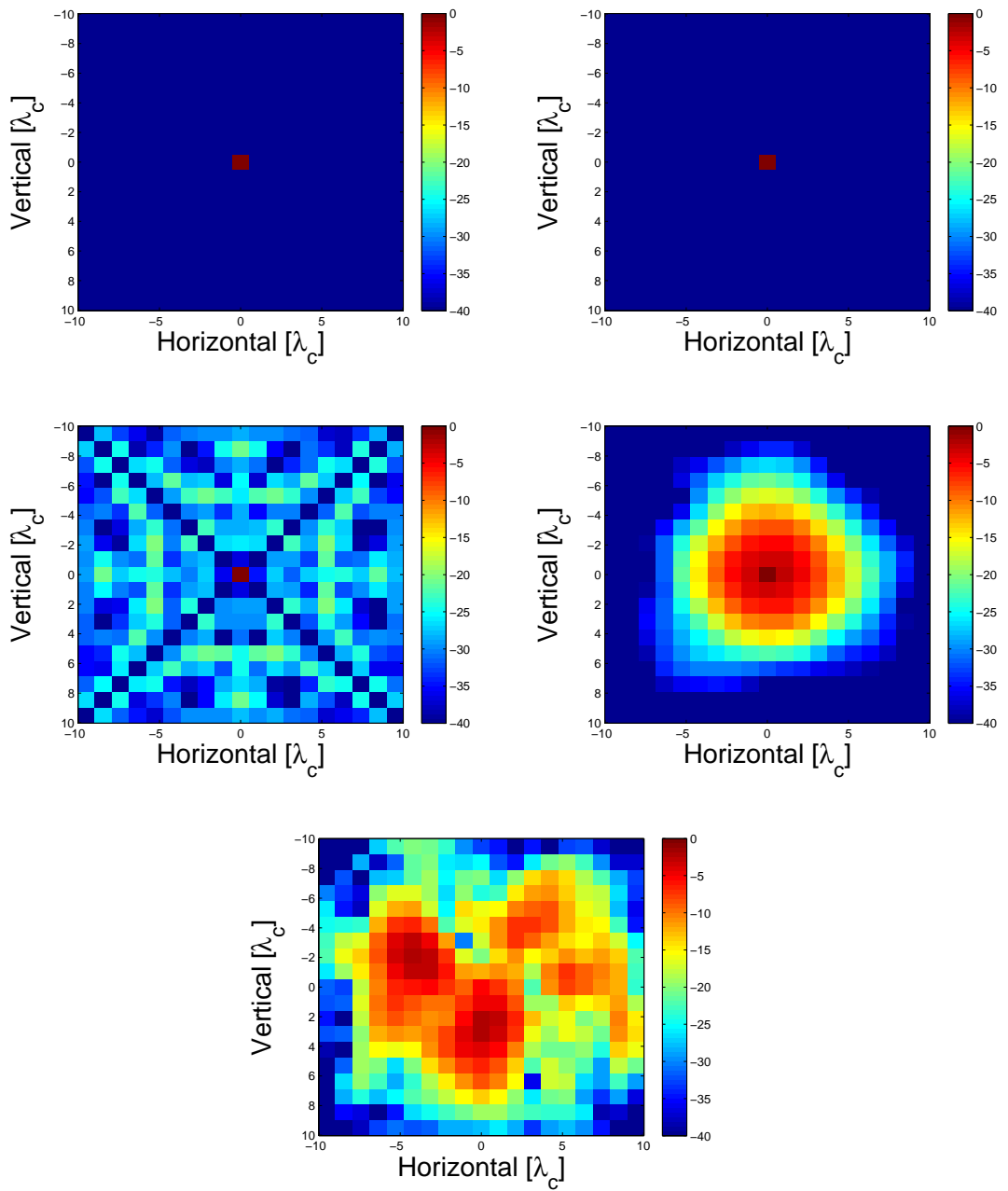


Figure 2.11: Central slice, ML results for point scatterer, SNR = 30 dB: CSBS-designed with uniform initialization (upper left), CSBS-designed with random initialization (upper right), rectangular (middle left), Mills Cross (middle right), ring-spiral (bottom)

type since they are optimized to operate well in the ML framework.

At 15 dB SNR, a sample image cube reconstruction is shown in Fig. 2.15, 2.16, and

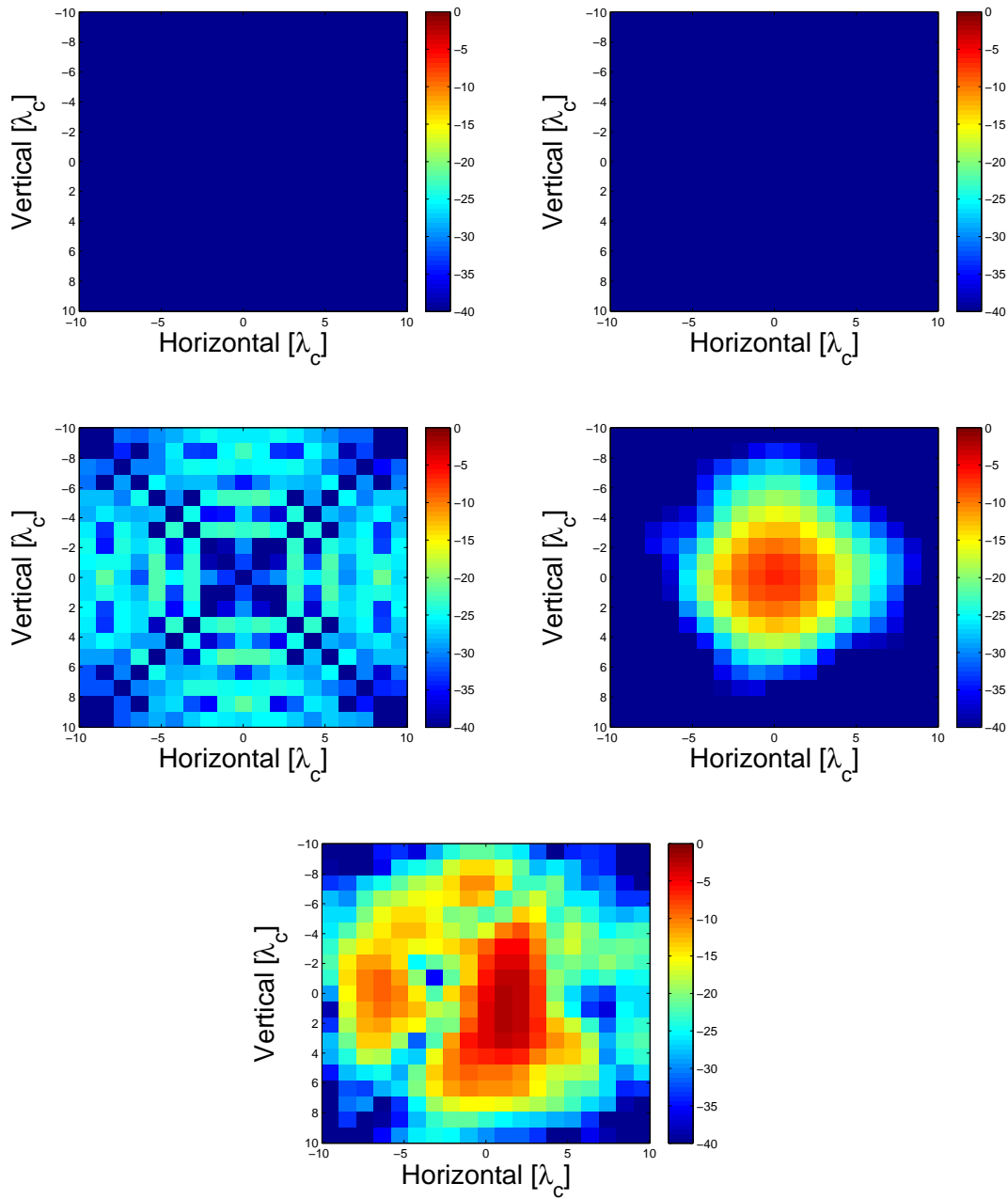


Figure 2.12: Range slice 1, ML results for point scatterer, SNR = 30 dB: CSBS-designed with uniform initialization (upper left), CSBS-designed with random initialization (upper right), rectangular (middle left), Mills Cross (middle right), ring-spiral (bottom)

2.17 for the PS target, and in Fig. 2.18 for the MPS and EO targets. As seen from the figures, none of the classical arrays do work properly at this SNR. However, the optimal arrays still yield good reconstructions for each target type.

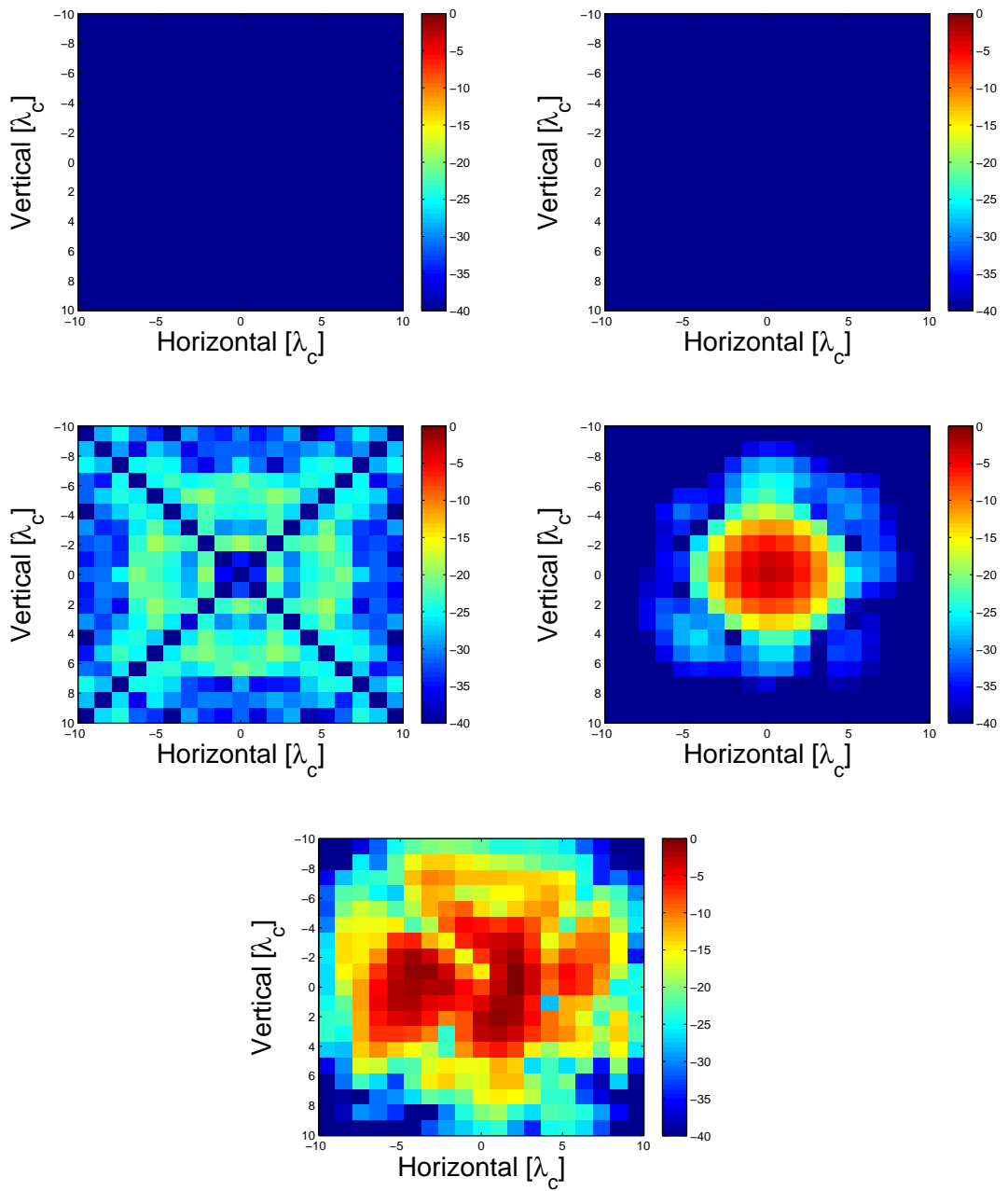


Figure 2.13: Range slice 3, ML results for point scatterer, SNR = 30 dB: CSBS-designed with uniform initialization (upper left), CSBS-designed with random initialization (upper right), rectangular (middle left), Mills Cross (middle right), ring-spiral (bottom)

The goodness of a design may also be assessed based on the extent and uniformity of its virtual array as in earlier works [24]. Fig. 2.19 shows the virtual arrays of all the designs. As seen in the figure, the virtual arrays of CSBS-based designs extend

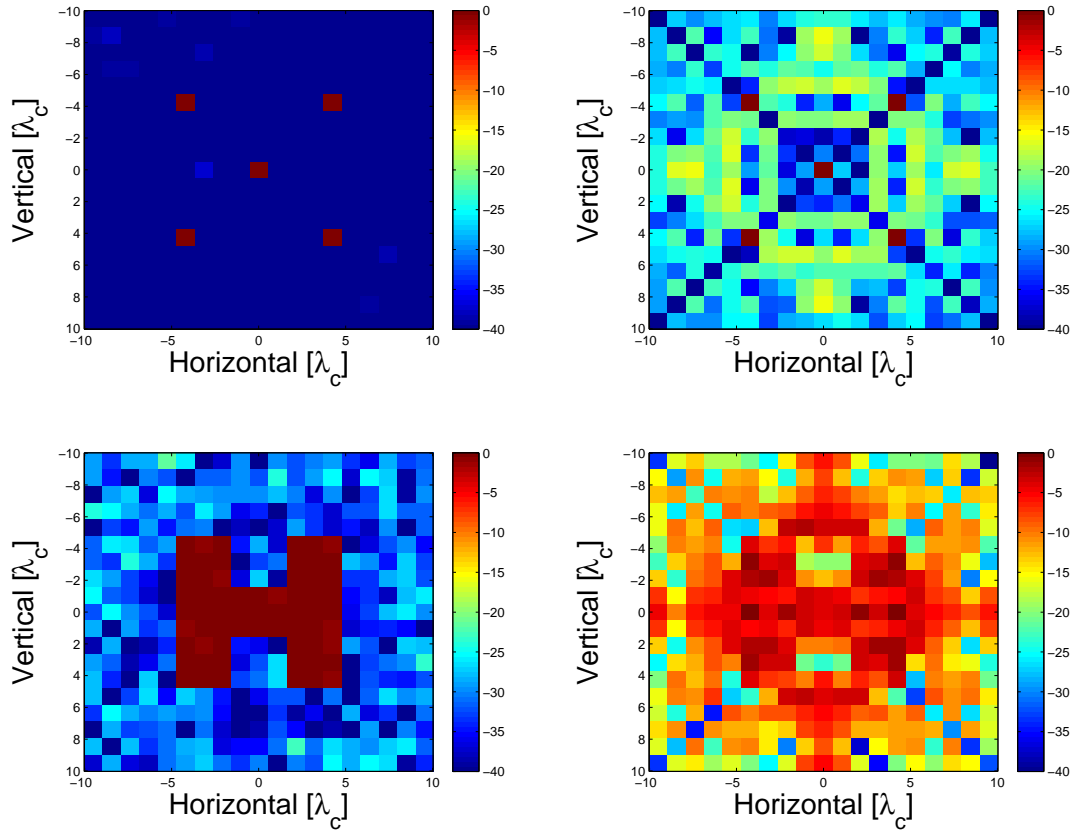


Figure 2.14: ML results for MPS and EO at SNR = 30 dB: Central range slice of CSBS-designed with random initialization (upper left), central range slice of rectangular (upper right), central range slice of CSBS-designed with random initialization (lower left), central range slice of rectangular (lower right)

from $-10\lambda_c$ to $10\lambda_c$, while the classical designs have smaller coverage. Moreover, the virtual array elements distribute more uniformly within this extent for the CSBS-designs.

For the chosen observation scenario, most of the antenna elements in the CSBS-designs appear close to the boundaries of the array plane. Additional simulations are performed to check whether this trend changes if the unknown image cube is smaller or bigger at cross ranges. Uniform initialization is utilized for this analysis. The image cube size is halved to obtain a smaller cube while the voxel sizes are kept as before. To generate a bigger image cube, the image cube size is doubled while the voxel sizes are also doubled at cross range. The resulting CSBS-designs are shown in Fig. 2.20. As seen, the obtained designs are similar in terms of the spread of the

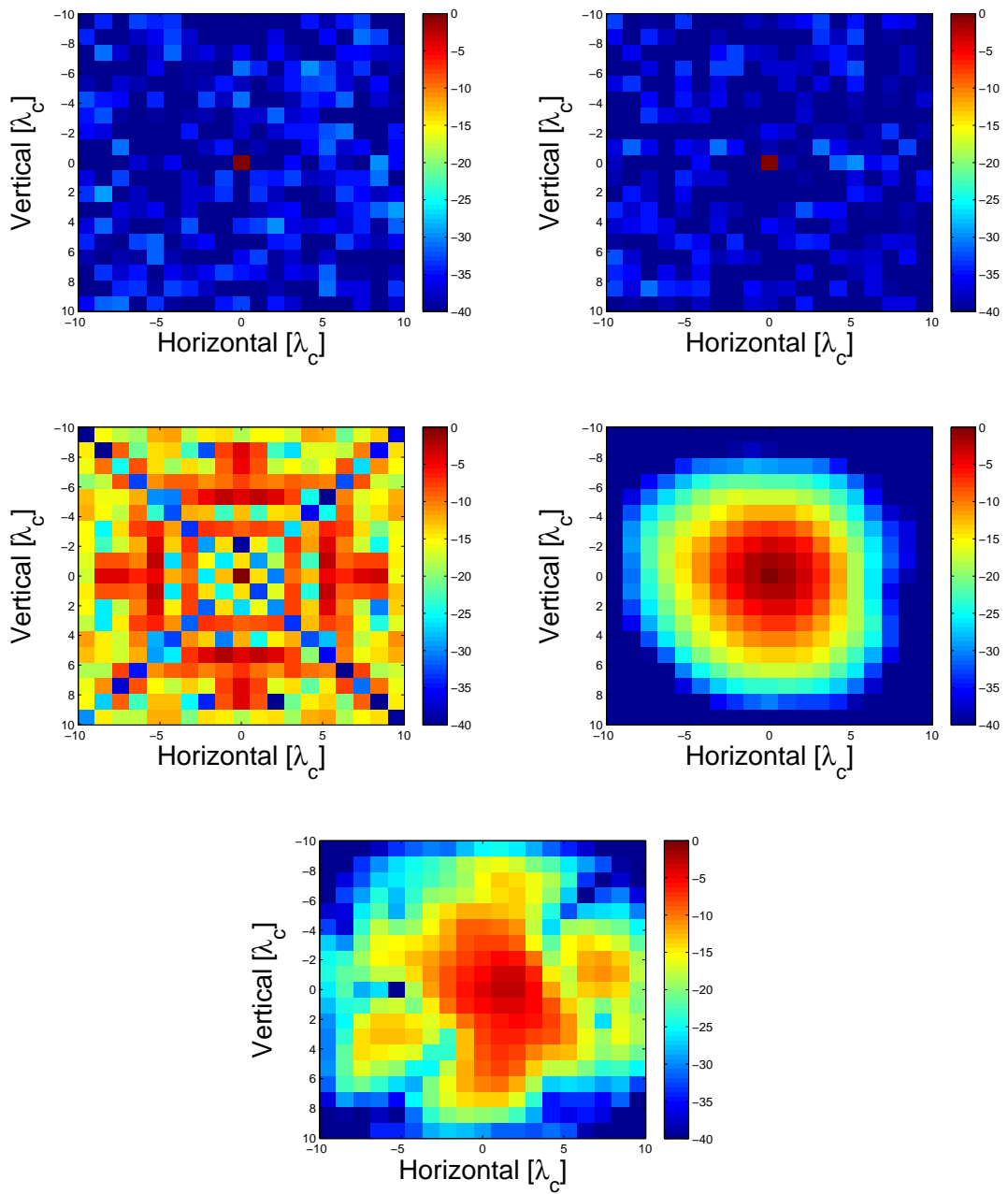


Figure 2.15: Central slice, ML results for point scatterer, SNR = 15 dB: CSBS-designed with uniform initialization (upper left), CSBS-designed with random initialization (upper right), rectangular (middle left), Mills Cross (middle right), ring-spiral (bottom)

antenna elements over the array plane. Hence, for these changes on the size of the image cube along cross range direction, most of the antenna elements are still located close to the boundaries.

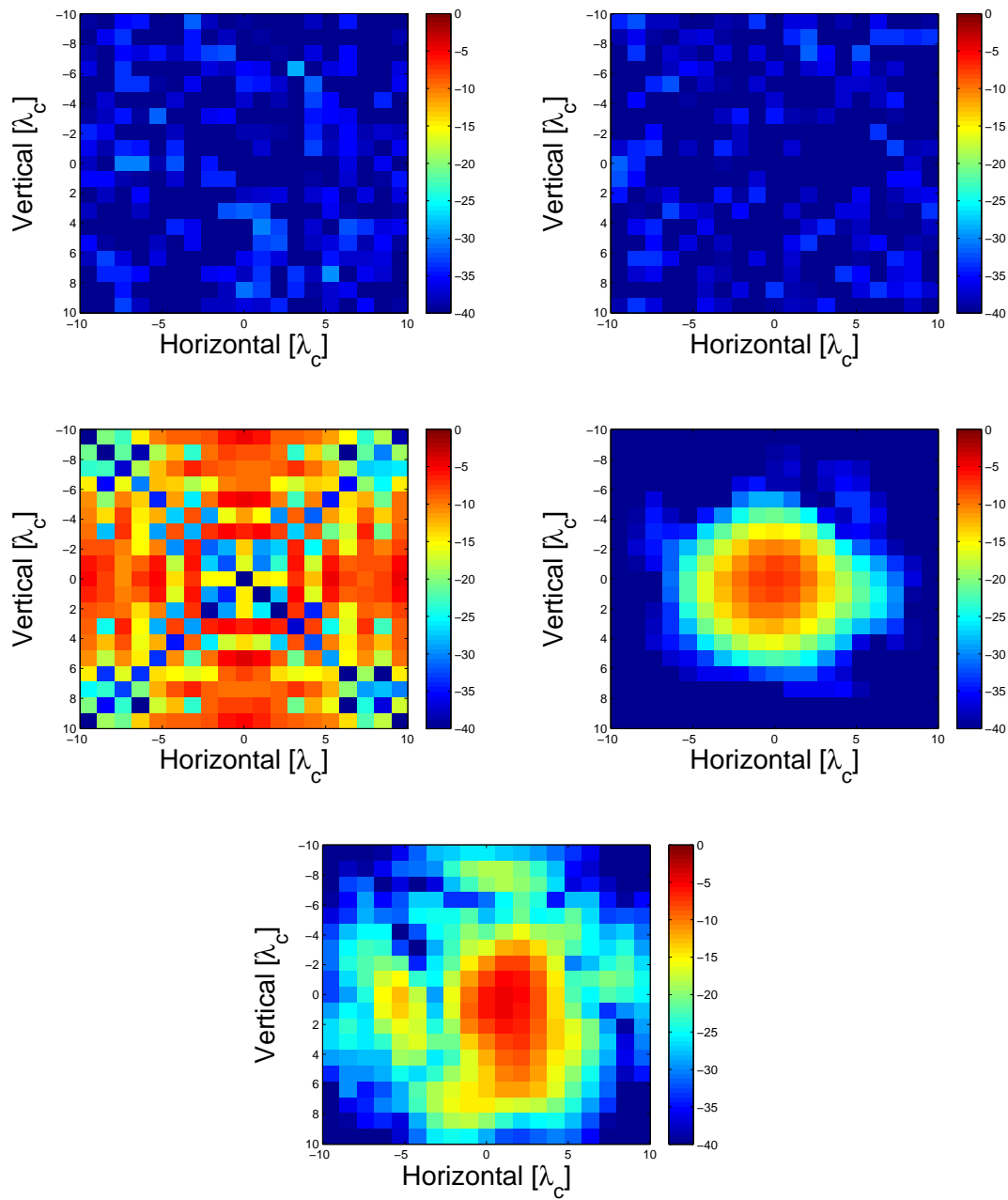


Figure 2.16: Range slice 1, ML results for point scatterer, SNR = 15 dB: CSBS-designed with uniform initialization (upper left), CSBS-designed with random initialization (upper right), rectangular (middle left), Mills Cross (middle right), ring-spiral (bottom)

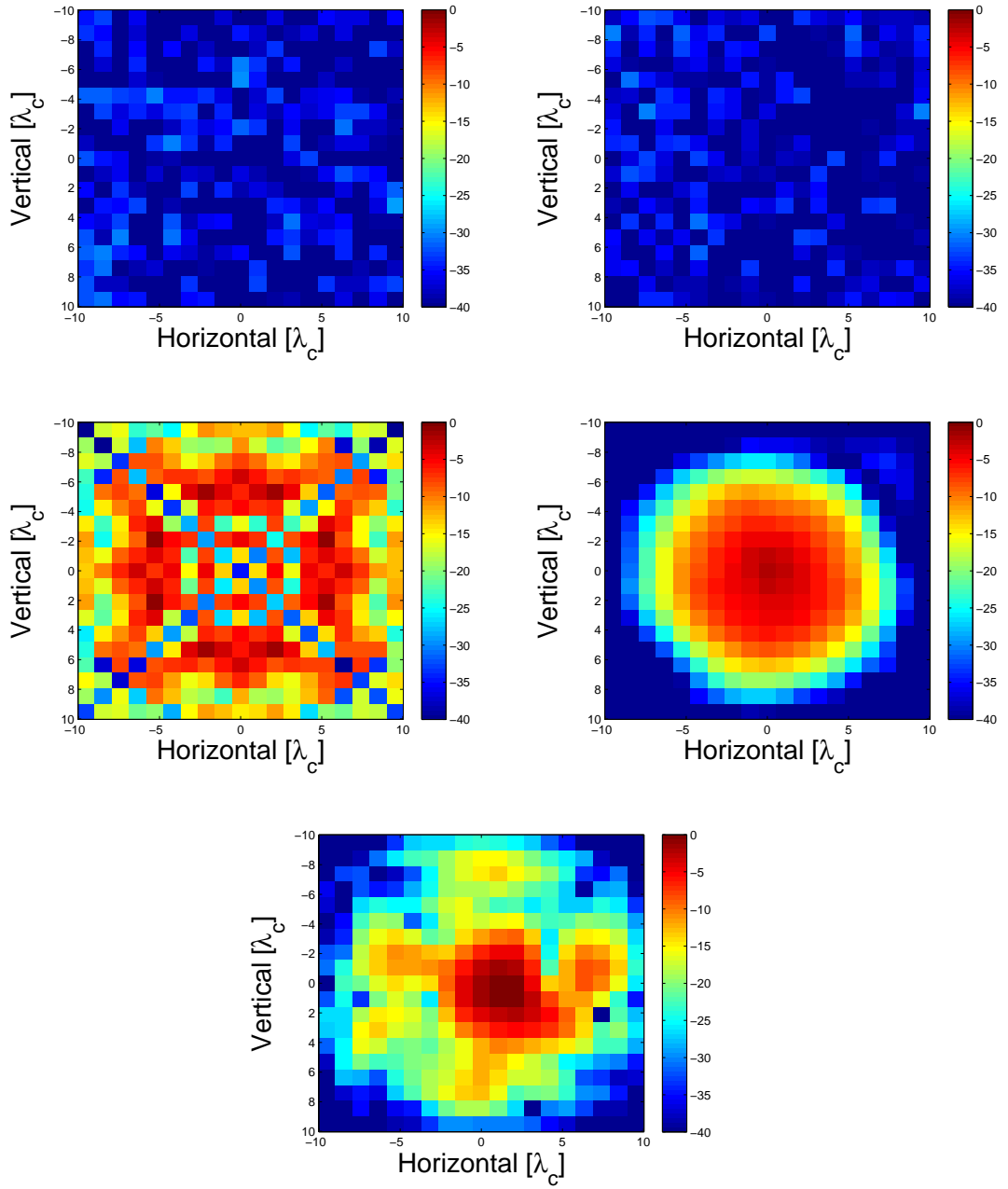


Figure 2.17: Range slice 3, ML results for point scatterer, SNR = 15 dB: CSBS-designed with uniform initialization (upper left), CSBS-designed with random initialization (upper right), rectangular (middle left), Mills Cross (middle right), ring-spiral (bottom)

2.3.2.2 Results for MAP Framework

In this section, instead of the ML framework, both the design optimization and the reconstructions are obtained using the MAP framework. The same scenario param-

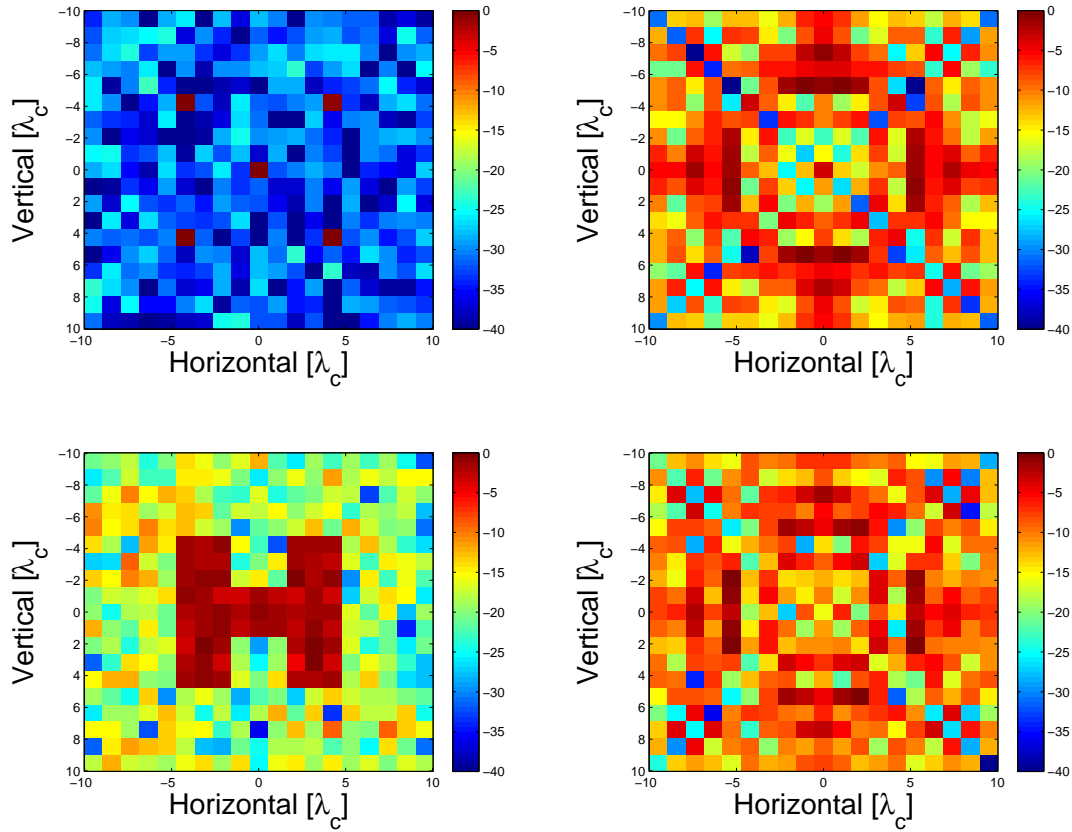


Figure 2.18: ML results for MPS and EO at SNR = 15 dB: Central range slice of CSBS-designed with random initialization (upper left), central range slice of rectangular (upper right), central range slice of CSBS-designed with random initialization (lower left), central range slice of rectangular (lower right)

ters in Table 2.1 are used. The MAP framework requires prior knowledge regarding the distribution of the unknown reflectivity vector. The prior distribution is chosen as Gaussian, as described in Section 2.2.1.2, with the mean set to 0 and the covariance matrix form given in terms of the discrete derivative operator. With this prior, the MAP estimate becomes equivalent to the Tikhonov regularized least squares solution.

The parameter λ appearing in the cost function of MAP framework (see Eqn. 2.38) should be different for different SNR values since λ increases with the noise variance σ_w^2 . To set this parameter (which is related to the prior distribution of the reflectivity), its optimal value is investigated for the known array topologies and different target types, then the value that generally yields good reconstructions is chosen as λ . In particular, λ is selected as 9×10^{-6} , 9×10^{-3} , and 3×10^{-1} in the design for SNRs

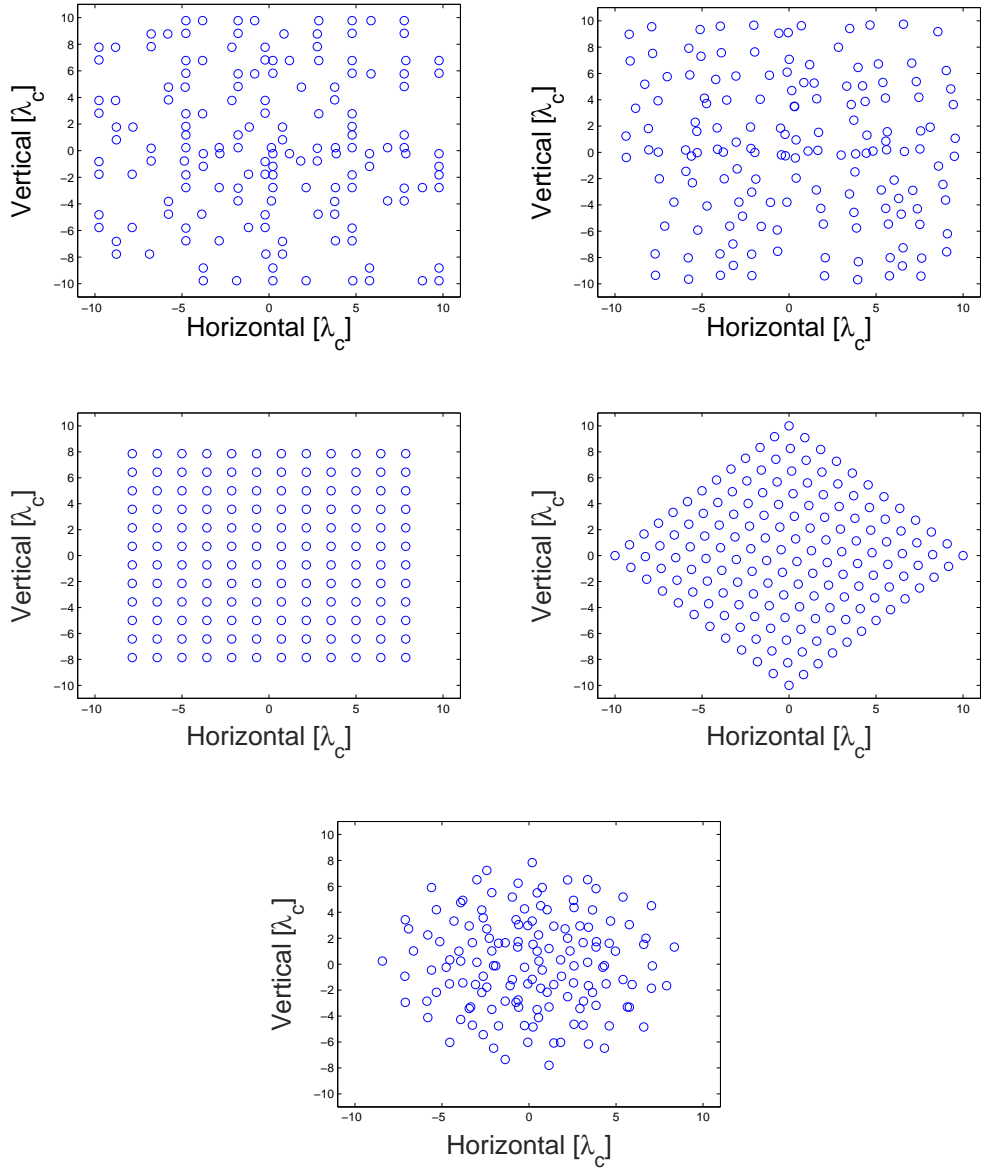


Figure 2.19: Virtual arrays for ML: CSBS-designed with uniform initialization (upper left), CSBS-designed with random initialization (upper right), rectangular (middle left), Mills Cross (middle right), ring-spiral (bottom)

of 60, 30 and 15 dB, respectively. Hence, each value is used for obtaining the MAP-based design at the corresponding SNR value.

The CSBS-designs obtained for the MAP framework at 60 dB SNR are shown in Fig. 2.21. For both uniform and random initializations, the resulting designs have same number of receive and transmit antennas, which are 12 and 13, respectively.

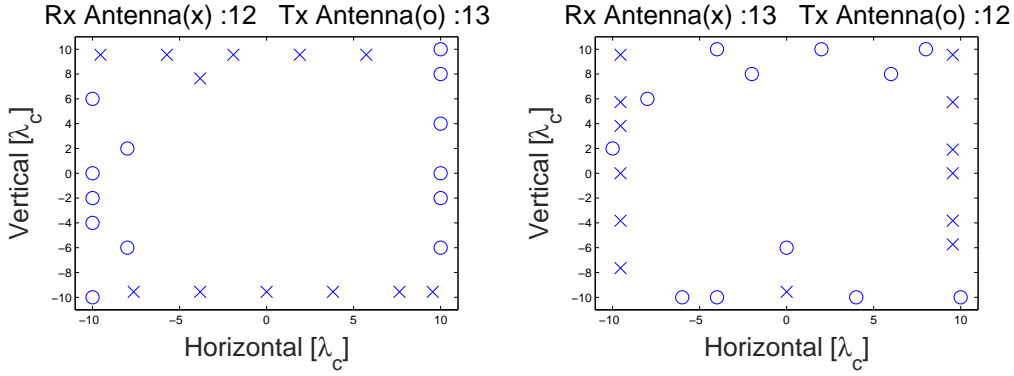


Figure 2.20: Optimal arrays for ML framework for different image cubes: CSBS-designed with uniform initialization for smaller cube (left), CSBS-designed with uniform initialization for bigger cube (right)

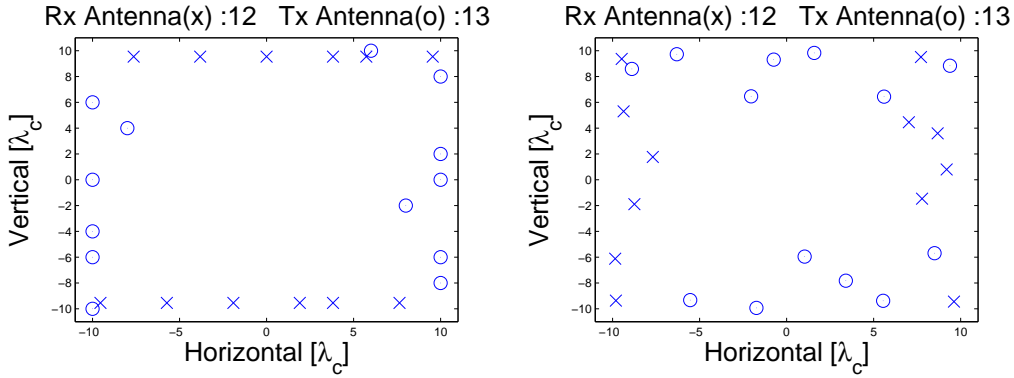


Figure 2.21: Optimal designs for MAP framework at SNR of 60 dB: CSBS-designed with uniform initialization (left), CSBS-designed with random initialization (right)

Table 2.7: Cost and MSE values using MAP framework for PS, MPS, EO for SNR = 60 dB

Array Type	Init. Cost _{MAP}	Final Cost _{MAP}	MSE, PS	MSE, MPS	MSE, EO
CSBS-design, init. uniform	3.74	1.3e+3	5.0e-6	2.5e-5	8.8e-4
CSBS-design, init. random	3.55	1.5e+3	5.8e-6	3.1e-5	1.1e-3
Rectangular	-	5.12e+4	8.2e-5	4.9e-4	0.03
Mills Cross	-	2.3e+5	0.05	0.08	0.11
Ring-spiral	-	8.5e+5	0.06	0.13	0.39

For the 60 dB SNR case, the results are summarized in Table 2.7. The table contains the cost values for different designs computed using Eqn. 2.38, and also the average MSE values for the reconstruction of different object types. Both the initial and final costs of the CSBS-based designs are provided whereas only the final costs are given for the known array topologies. (In particular, the initial cost is the cost value for the initial array with 242 antenna elements and the final cost is the cost value after reduction to 25 elements.)

At 60 dB SNR, the CSBS-designed arrays outperform the classical arrays in terms of the cost values. The best array is the CSBS-based design with uniform initialization, and the best classical array is the rectangular array. The image reconstruction performance of these arrays for the PS target is shown in Fig. 2.22, and the image reconstruction results for MPS and EO target types are shown in Fig. 2.23 for best CSBS and classical arrays. Sample reconstructions also illustrate that the CSBS-based arrays and the rectangular array have better imaging performance than the others.

It is also observed that the MSE values are not much different than the ML case. This is expected because the SNR is high and the prior term (i.e. the regularization) does not significantly contribute to the solution in this case.

Table 2.8: Cost and MSE values using MAP framework for PS, MPS, EO for SNR = 30 dB

Array Type	Init. Cost _{MAP}	Final Cost _{MAP}	MSE, PS	MSE, MPS	MSE, EO
CSBS-design, init. uniform	3.74	0.9e+3	4.8e-3	2.5e-2	0.54
CSBS-design, init. random	3.55	1.1e+3	5.8e-3	2.8e-2	0.68
Rectangular	-	1.9e+3	0.02	0.09	1.03
Mills Cross	-	2.4e+3	0.11	0.36	1.72
Ring-spiral	-	4.2e+3	0.21	0.68	2.39

The virtual arrays of the CSBS-designs are shown in Fig. 2.24. As seen in the figure, the virtual arrays of CSBS-based designs extend from $-10\lambda_c$ to $10\lambda_c$, while the classical designs have smaller coverage. Moreover, there is no overlap among the elements of the virtual array for the CSBS-based design with uniform initialization

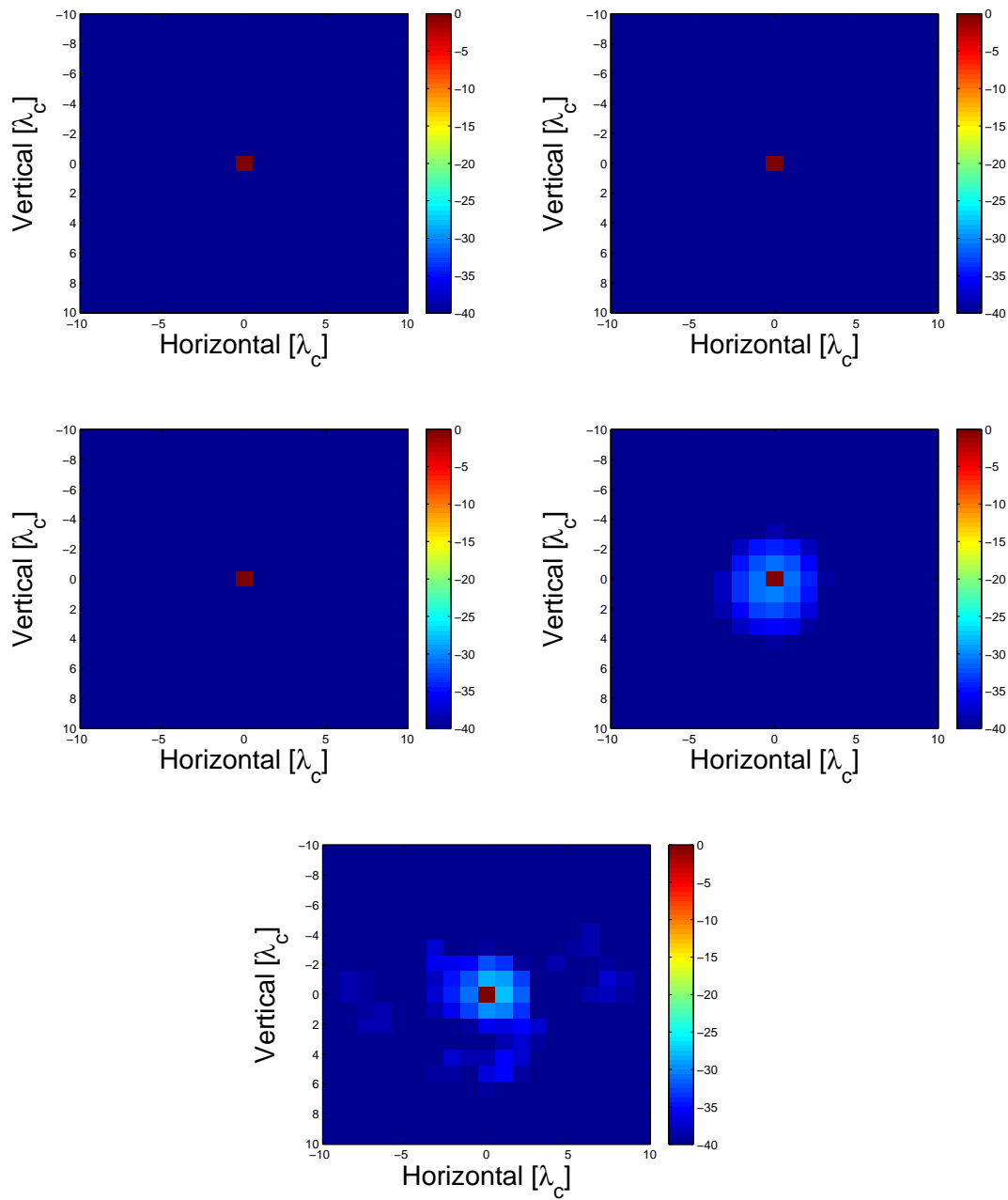


Figure 2.22: MAP results for point scatterer at SNR of 60 dB: CSBS-designed with uniform initialization (upper left), CSBS-designed with random initialization (upper right), rectangular (middle left), Mills Cross (middle right), ring-spiral (bottom)

whereas a couple of overlaps exist for CSBS-based design with random initialization, which could be another indicator of the better design for the CSBS-based array with uniform initialization.

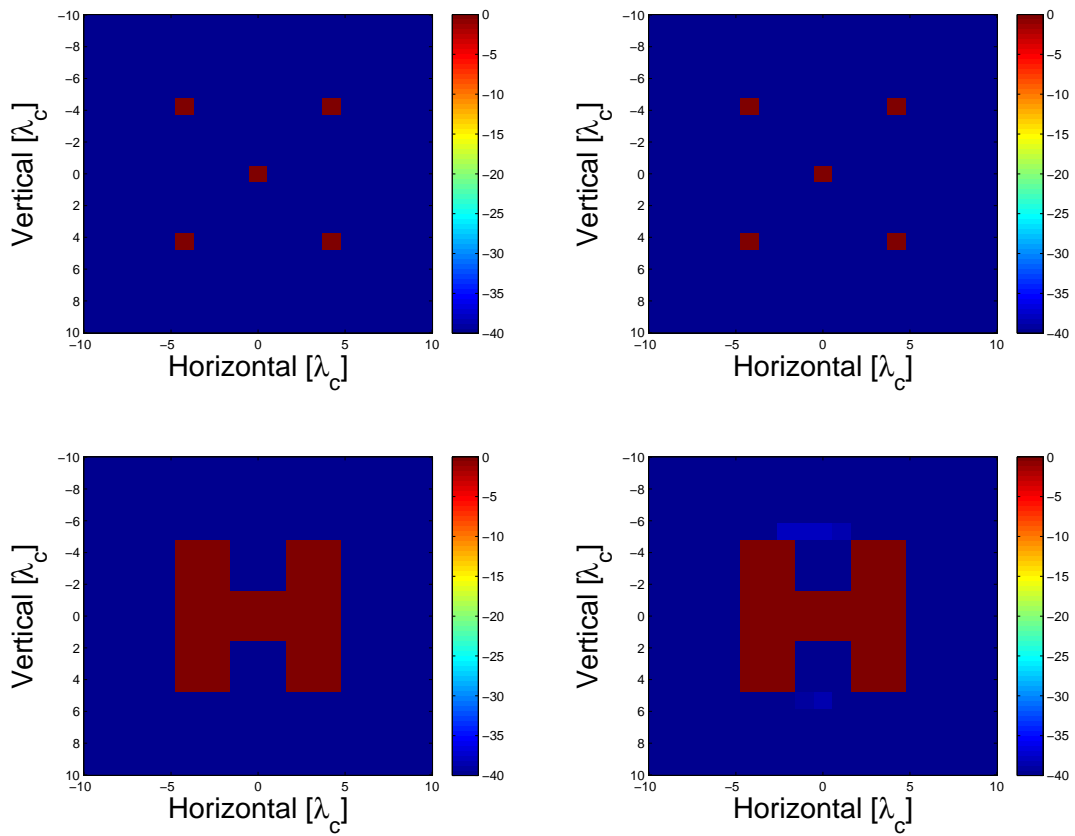


Figure 2.23: MAP results for MPS and EO at SNR of 60 dB: Central range slice of CSBS-designed with uniform initialization (upper left), central range slice of rectangular (upper right), central range slice of CSBS-designed with uniform initialization (lower left), central range slice of rectangular (lower right)

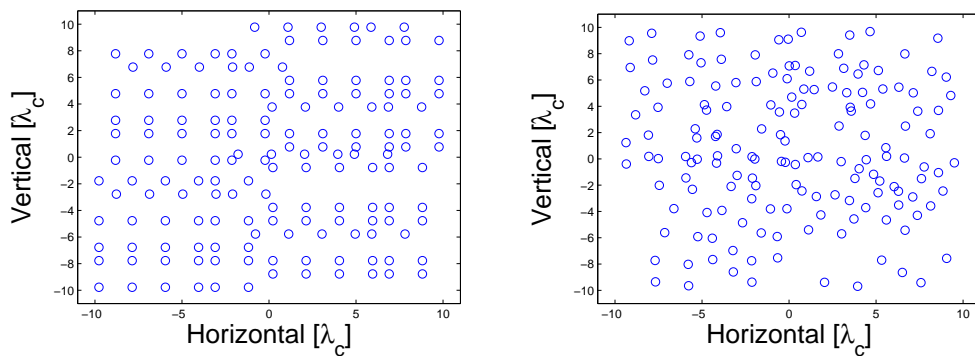


Figure 2.24: Virtual arrays for MAP at SNR of 60 dB: CSBS-designed with uniform initialization (left), CSBS-designed with random initialization (right)

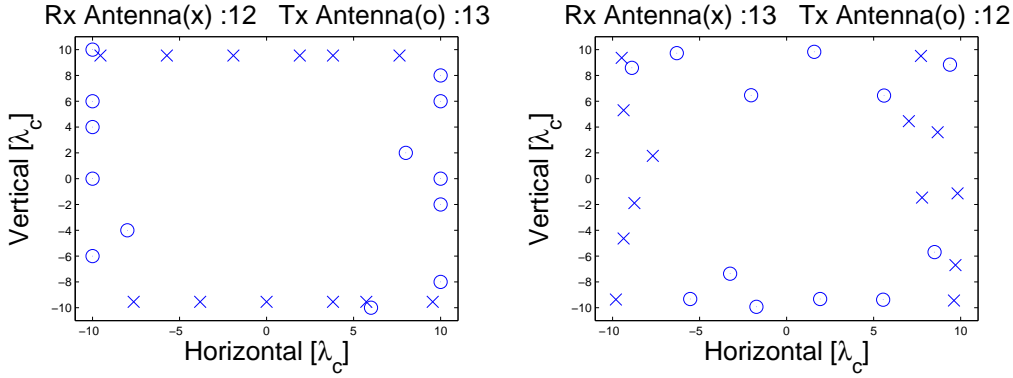


Figure 2.25: Optimal arrays for MAP framework at SNR of 30 dB: CSBS-designed with uniform initialization (left), CSBS-designed with random initialization (right)

The CSBS-designs obtained for SNR= 30 dB case are shown in Fig. 2.25, and the related results are given in the Table 2.8, and Fig. 2.26 and 2.27. The virtual arrays of these designs are also shown in Fig. 2.28. The number of receiver and transmitter antennas are 12 and 13, respectively, for the CSBS-design with uniform initialization, and 13 and 12, respectively, for the CSBS-design with random initialization. Observations are similar with the SNR= 60 dB case; the CSBS-based designs outperform the classical arrays in terms of cost values.

The CSBS-designs obtained for SNR= 15 dB case are shown in Fig. 2.29. In both designs, the number of receiver and transmitter antennas are 12 and 13, respectively. The performance related results are given in the Table 2.9, and Fig. 2.30 and 2.31. This time the best array is the CSBS-based design with random initialization, while the best classical array is the rectangular array. The virtual array of each design is also given in Fig. 2.32. Couple of overlaps exists for both CSBS-designs. Other observations are similar as before; the CSBS-based designs outperform the classical arrays in terms of cost values.

The difference between ML and MAP reconstructions is apparent at higher noise levels. For example at 15 dB SNR, MAP reconstructions are better than ML reconstructions in terms of reconstruction quality, especially for the EO target type. This can be observed by comparing Fig. 2.18 and 2.31.

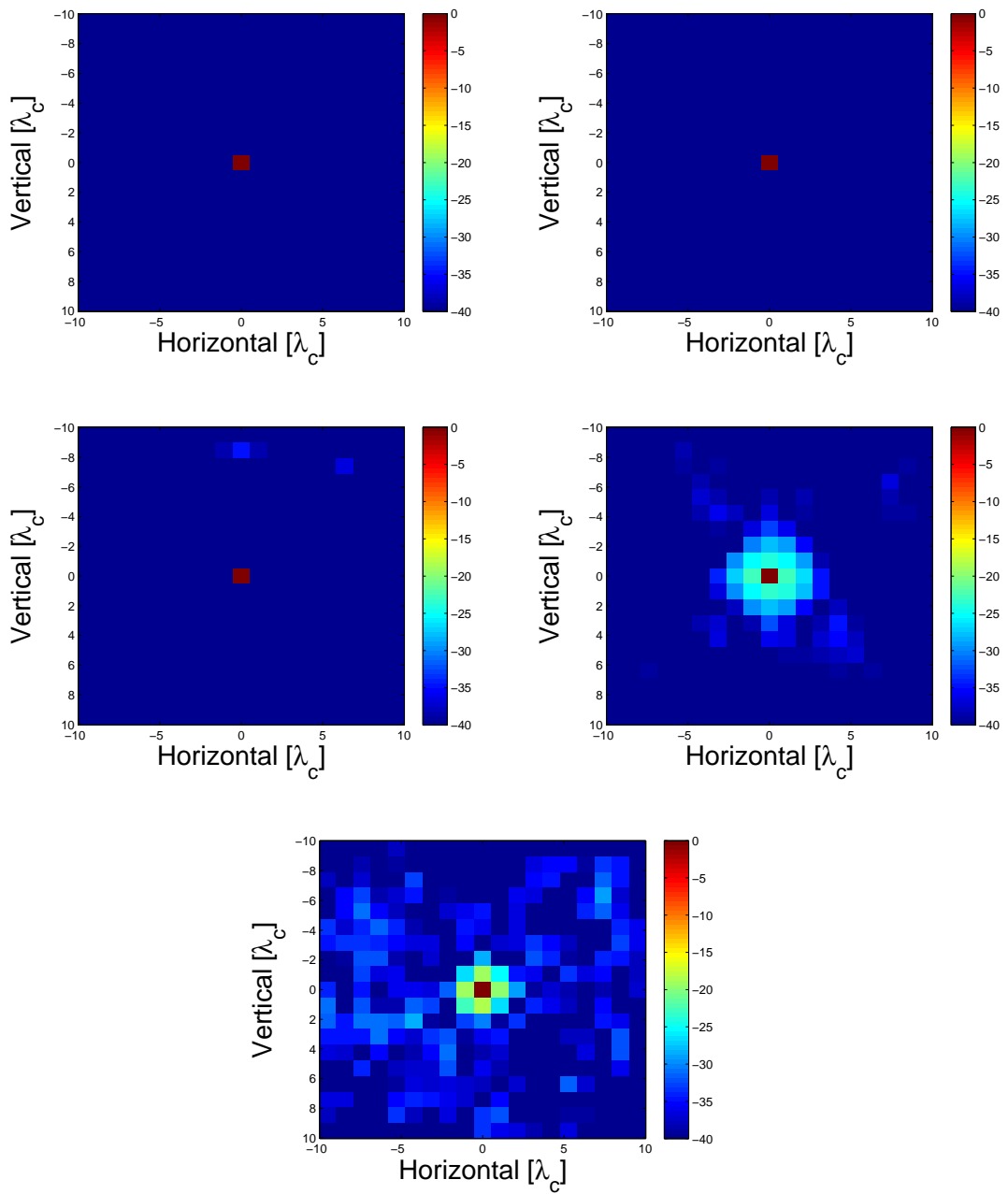


Figure 2.26: MAP results for PS at SNR of 30 dB: CSBS-designed with uniform initialization (upper left), CSBS-designed with random initialization (upper right), rectangular (middle left), Mills Cross (middle right), ring-spiral (bottom)

2.3.2.3 Comparison of Obtained Designs

Many designs are obtained using the same initializations for both ML and MAP frameworks. In this section, we compare these designs with each other to gain a better

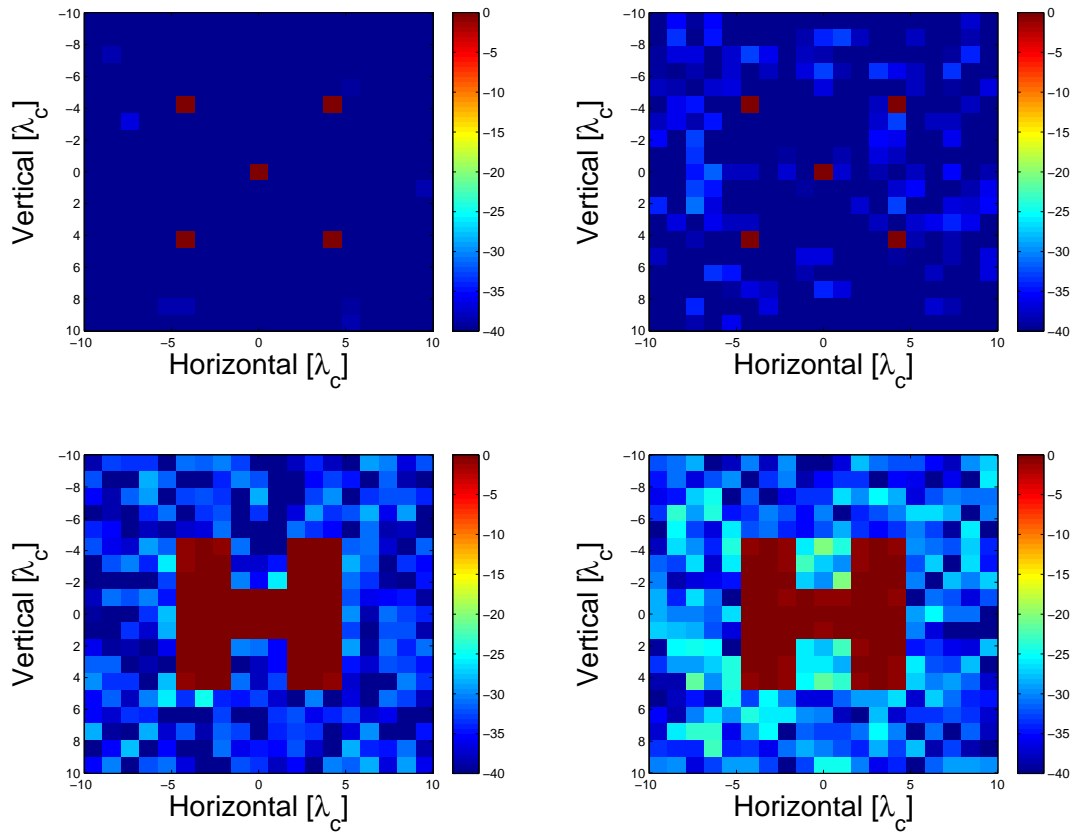


Figure 2.27: MAP results at SNR of 30 dB: CSBS-designed with uniform initialization, MPS (upper left), rectangular, MPS (upper right), CSBS-designed with uniform initialization, EO (lower left), rectangular, EO (lower right)

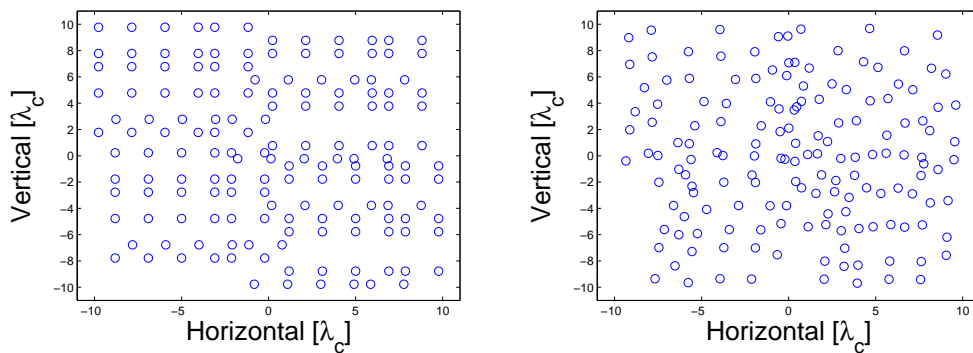


Figure 2.28: Virtual arrays for MAP at SNR of 30 dB: CSBS-designed with uniform initialization (left), CSBS-designed with random initialization (right)

understanding of the performance of the CSBS algorithm and the resulting designs.

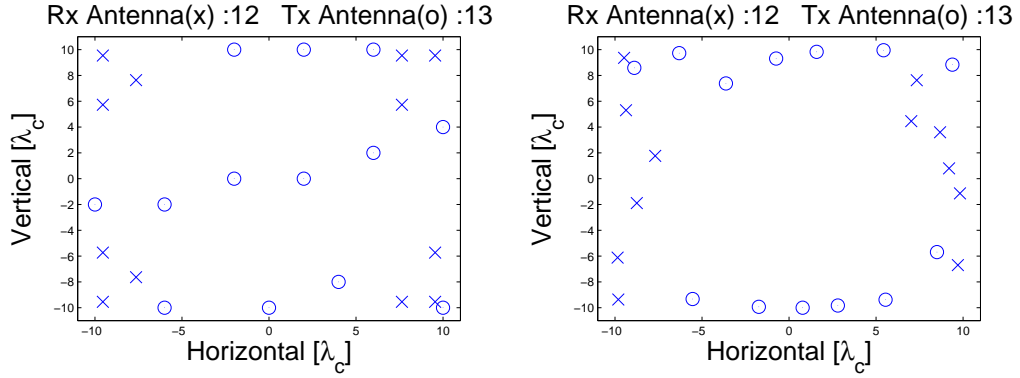


Figure 2.29: Optimal designs for MAP framework at SNR of 15 dB: CSBS-designed with uniform initialization (left), CSBS-designed with random initialization (right)

Table 2.9: Cost and MSE values using MAP framework for PS, MPS, EO for SNR = 15 dB

Array Type	Init. Cost_{MAP}	Final Cost_{MAP}	MSE, PS	MSE, MPS	MSE, EO
CSBS-design, init. uniform	3.71	268	0.12	0.61	5.4
CSBS-design, init. random	3.52	263	0.10	0.51	5.1
Rectangular	-	294	0.12	0.83	5.6
Mills Cross	-	302	0.28	0.99	6.3
Ring-Spiral	-	356	0.36	1.41	7.9

If we compare the locations of the antenna elements in different designs, the CSBS-based designs with the uniform initialization is different for ML and MAP frameworks. However, the CSBS-based designs obtained with the same random initialization have some similarities such that the locations of the nearly 20 antenna elements coincide. Hence, for uniformly distributed initialization different optimal arrays are obtained for ML and MAP frameworks whereas for randomly distributed initialization rather similar designs are obtained with the CSBS algorithm.

Comparing the locations of the antenna elements in MAP-based designs, the designs with uniform initialization are different for 15 dB SNR. But for 60 dB and 30 dB SNR designs, antenna locations are symmetrical with respect to x axis. Moreover, the CSBS-based designs with random initialization also resemble to each other (except

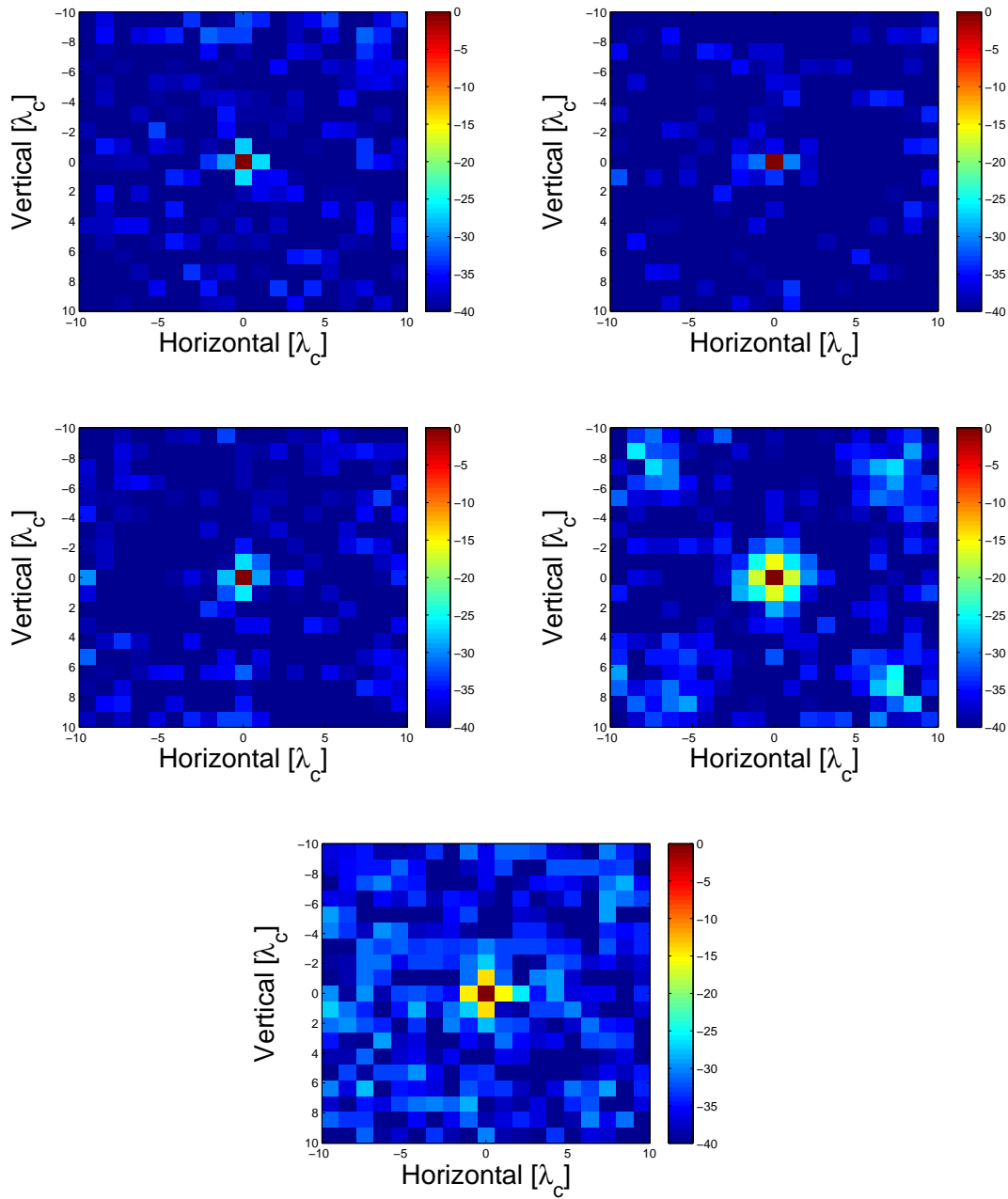


Figure 2.30: MAP results for point scatterer at SNR of 15 dB: CSBS-designed with uniform initialization (upper left), CSBS-designed with random initialization (upper right), rectangular (middle left), Mills Cross (middle right), ring-spiral (bottom)

dislocation of a couple of antenna elements).

The designs can also be compared by calculating their cost values when operated at a different setting than their design settings (such as ML or MAP, different SNR).

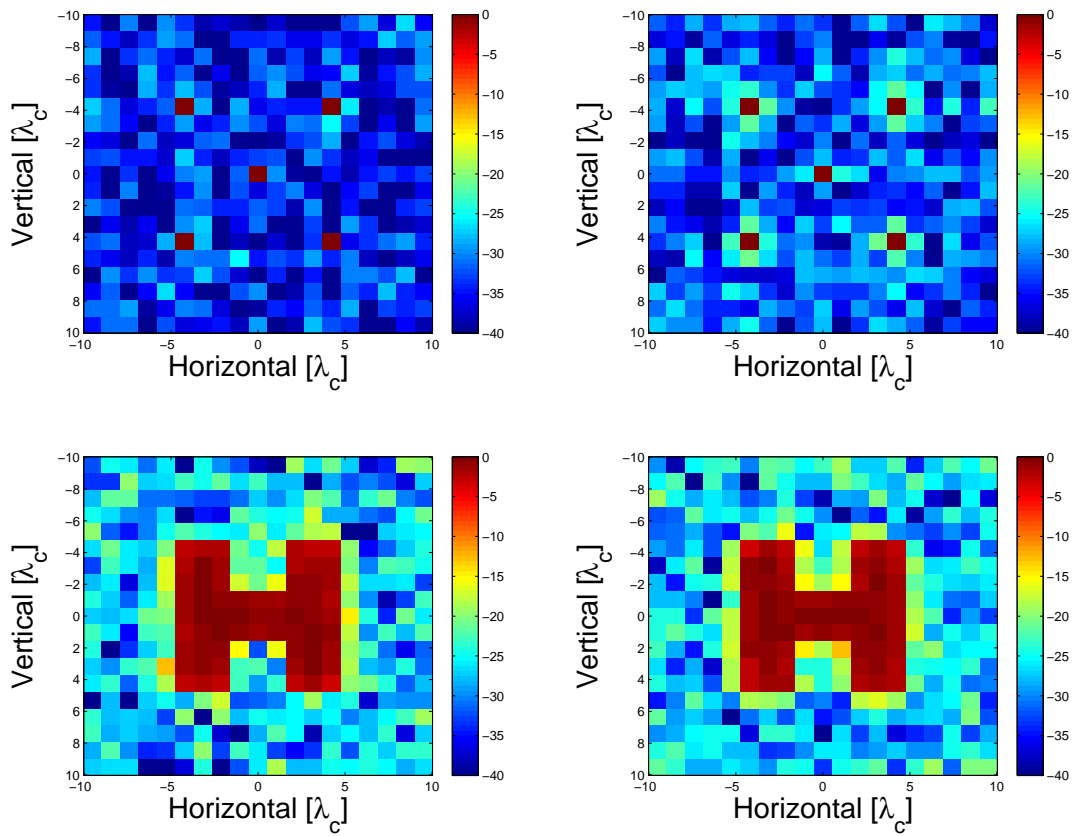


Figure 2.31: MAP results at SNR of 15 dB: CSBS-designed with random initialization for MPS (upper left), rectangular for MPS (upper right), CSBS-designed with random initialization for EO (lower left), rectangular for EO (lower right)

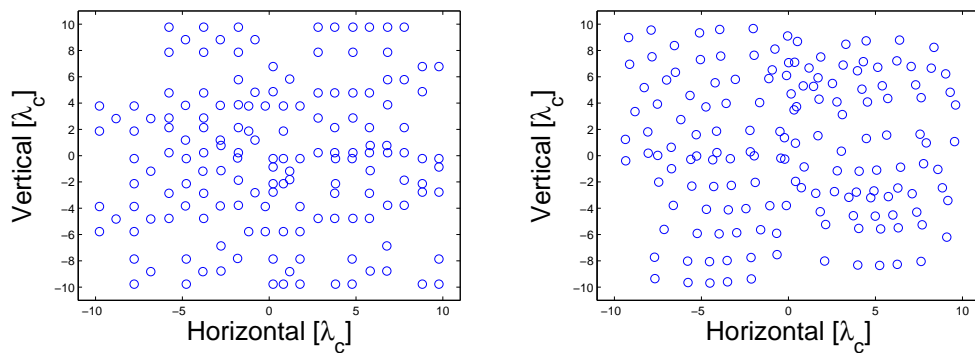


Figure 2.32: Virtual arrays for MAP at SNR of 15 dB: CSBS-designed with uniform initialization (left), CSBS-designed with random initialization (right)

For instance, the cost value can be computed if a design obtained for ML framework were to be used for MAP framework. These cost values are provided in Table 2.10 for

all CSBS-based designs, as well as for the uniform rectangular array, which appears as the best classical design for the chosen scenario. Four different cost values are available for each array in this table. Cost_{ML} corresponds to the cost value in the ML framework, i.e. $\text{Cost}(\mathbf{A})_{\text{ML}}$ in Eqn. 2.37. $\text{Cost}_{\text{MAP},60 \text{ dB}}$ is the cost value in the MAP framework for 60 dB SNR case, i.e. $\text{Cost}(\mathbf{A})_{\text{MAP}}$ in Eqn. 2.38 with $\lambda = 9 \times 10^{-6}$. $\text{Cost}_{\text{MAP},30 \text{ dB}}$ is the cost value in the MAP framework for 30 dB SNR case, i.e. $\text{Cost}(\mathbf{A})_{\text{MAP}}$ in Eqn. 2.38 with $\lambda = 9 \times 10^{-3}$. Lastly, $\text{Cost}_{\text{MAP},15 \text{ dB}}$ is the cost value in the MAP framework for 15 dB SNR value, i.e. $\text{Cost}(\mathbf{A})_{\text{MAP}}$ in Eqn. 2.38 with $\lambda = 3 \times 10^{-1}$.

Table 2.10: Cost values for ML and MAP frameworks

Array Type	Cost_{ML}	$\text{Cost}_{\text{MAP},60 \text{ dB}}$	$\text{Cost}_{\text{MAP},30 \text{ dB}}$	$\text{Cost}_{\text{MAP},15 \text{ dB}}$
Best ML	1.44e+3	1.44e+3	1.03e+3	264
Best MAP 60 dB	1.33e+3	1.33e+3	974	260
Best MAP 30 dB	1.33e+3	1.33e+3	974	260
Best MAP 15 dB	1.45e+3	1.45e+3	1.03e+3	263
Rectangular	4.28e+5	5.12e+4	1.94e+3	294

The values in the table can be interpreted by considering each cost type (i.e. cost values in one row) separately. For example, if we compare the Cost_{ML} values provided for each array, the minimum value is achieved by the best CSBS-designs for the MAP 60 dB and MAP 30 dB cases. It is desired that the best CSBS-design obtained for the ML case should have the minimum Cost_{ML} value. However, due to the sub-optimality of the CSBS algorithm, the best array obtained for the ML setting does not achieve the minimum Cost_{ML} value. However, it should also be noted that Cost_{ML} values of all CSBS-based arrays are close to each other, hence the difference in the cost value is not significant.

The best CSBS-designs for the MAP 60 dB and MAP 30 dB cases have the same cost values for all cost types. As mentioned above, these designs are essentially the same. In particular, their antenna locations are symmetric with respect to x-axis. Hence, they have the same cost values for all cost types.

The minimum $\text{Cost}_{\text{MAP},60 \text{ dB}}$ value is obtained by both MAP 60 dB and MAP 30 dB designs. This also illustrates the sub-optimality of the CSBS algorithm. It is also observed that Cost_{ML} and $\text{Cost}_{\text{MAP},60 \text{ dB}}$ values for each CSBS- array are the same. The reason is that $\text{Cost}_{\text{MAP},60 \text{ dB}}$ is calculated by using the smallest λ (i.e. regularization) value among all MAP settings. The term in the $\text{Cost}_{\text{MAP},60 \text{ dB}}$ due to prior becomes negligibly small in this case, and $\text{Cost}_{\text{MAP},60 \text{ dB}}$ value becomes equal to Cost_{ML} value.

The minimum $\text{Cost}_{\text{MAP},30 \text{ dB}}$ value is obtained by both MAP 60 dB and MAP 30 dB designs. Moreover, the minimum $\text{Cost}_{\text{MAP},15 \text{ dB}}$ value is also obtained by both MAP 60 dB and MAP 30 dB designs. However, it is desired for the best MAP 15 dB design to have minimum $\text{Cost}_{\text{MAP},15 \text{ dB}}$ value; but this is not achieved due to the sub-optimality of the algorithm. However, the rectangular array is the worst array for all cost types. Hence, the sub-optimal algorithm is still able find a better design than the classical designs for the analyzed simulation scenario.

CHAPTER 3

OPTIMAL DESIGN WITH PRACTICAL CONSIDERATIONS

A design approach for sparse MIMO arrays is presented in Chap. 2. In this chapter, the design approach is extended to incorporate different practical considerations into the design. First, the design approach for synthetic aperture-based implementation is investigated. Second, the antenna patterns for both transmit and receive antennas are also included into the formulation and the design approach.

3.1 Enforcing a Synthetic Aperture

The number of antennas used in the MIMO system affects the cost of the design and the data acquisition time. Moreover, the reduction in the size of the observation matrix yields faster reconstruction. For these reasons, it is often desirable to decrease the number of antennas.

The reduction in the number of antennas, on the other hand, degrades the image reconstruction quality. Introducing a synthetic aperture can help to enhance the image reconstruction quality due to the increase in the aperture size [1]. There are different ways of creating a aperture such as by circularly rotating the array plane around a center point or shifting the array plane to the predefined locations. The main goal of moving the array plane is to increase the aperture size and measurement diversity so that the quality of the reconstructed images can be improved [4, 13].

In this section, the modifications on the observation model and the optimal design method are presented for a general synthetic aperture setting. The simulation scenario and the results are provided for one special case of generating synthetic aperture. This

case consists of shifting the array plane to the four quadrants successively.

3.1.1 Observation Model

In this setting, the locations of the antenna elements are changed by moving the array plane from one location to another. The observations are taken at each location. The corresponding matrix-vector form for the observations is the following:

$$y^{(u)} = A^{(u)}f + w^{(u)}, \quad (3.1)$$

Here, upper index, u , indicates the location of array plane. To be more precise, there are U array plane location in the synthetic aperture implementation, hence u is a discrete variable taking values from the set $\{1, 2, \dots, U\}$. Hence, $y^{(u)}$ is the measurement vector, $w^{(u)}$ is the noise vector, and $A^{(u)}$ is the observation matrix for the u th location of the array plane.

Prior to applying the design method, the observations taken at different locations of the array plane should be combined. By vertically concatenating both $y^{(u)}$ vectors and $A^{(u)}$ matrices, the forward model becomes:

$$y = Af + w, \quad (3.2)$$

where

$$y = \begin{bmatrix} y^{(1)} \\ y^{(2)} \\ \vdots \\ y^{(U)} \end{bmatrix}, \quad A = \begin{bmatrix} A^{(1)} \\ A^{(2)} \\ \vdots \\ A^{(U)} \end{bmatrix} \quad (3.3)$$

3.1.2 Optimal Design Method

Having derived the matrix-vector form for the observation model, the optimal design method can be applied. Geometry configuration of synthetic aperture is different from the prior array configurations since for each location of the array plane same transmit and receive antenna pair is used to take measurements. Hence, in the optimization algorithm, the observations from different locations of the antenna array should be

taken into account for calculating the cost value of the specific antenna element. For this reason, the iteration in the CSBS algorithm is updated as follows:

$$\Gamma \leftarrow \Gamma \setminus k^* : k^* = \arg \min_{k \in \Gamma} \sum_{u \in \Lambda} \sum_{i \in \Pi_k^{(u)}} \frac{a_i^{(u)} \Sigma_e^2 a_i^{(u)H}}{1 - a_i^{(u)} \Sigma_e a_i^{(u)H}}, \quad (3.4)$$

where Γ contains the indices of the antenna elements in the MIMO array configuration, and k^* represents the index of the antenna element that is removed from the current configuration. Λ contains the indices for the locations of the array plane, and u indicates at which location array plane is placed. Moreover, $a_i^{(u)}$ represents the i th row of the observation matrix when the array plane is in the u th location and $\Pi_k^{(u)}$ contains the row numbers corresponding to the measurements related to the k th antenna element. To compute this cost function, matrix Σ_e is required to be updated at each iteration using the current observation matrix A^Γ and Eqn. 2.38.

3.1.3 Numerical Results

The aim of this section is to present the performance of the design method when a synthetic aperture is implemented.

3.1.3.1 Simulation Scenario

The chosen synthetic aperture geometry is demonstrated in Fig. 3.1. The moving platform is such that the MIMO array is placed at four different quadrants. The quadrants are separated by a distance D . The transmit and receive antennas in the array are initially assumed to be placed in the location II . The observations for different transmit and receive antenna pairs at predefined frequency steps are taken in this location. Then, the MIMO array is shifted to the locations I , IV , and III , and measurements are taken from each location.

The structure of the observation matrix A is depends on the synthetic aperture geometry as mentioned earlier. The matrix A consists of 4 parts each corresponding to a different location. The observation matrix at each location can be represented as $A^{(I)}$, $A^{(II)}$, $A^{(III)}$ and $A^{(IV)}$. Thus, the matrix A can be defined as $A = [A^{(I)}; A^{(II)}; A^{(III)}; A^{(IV)}]$.

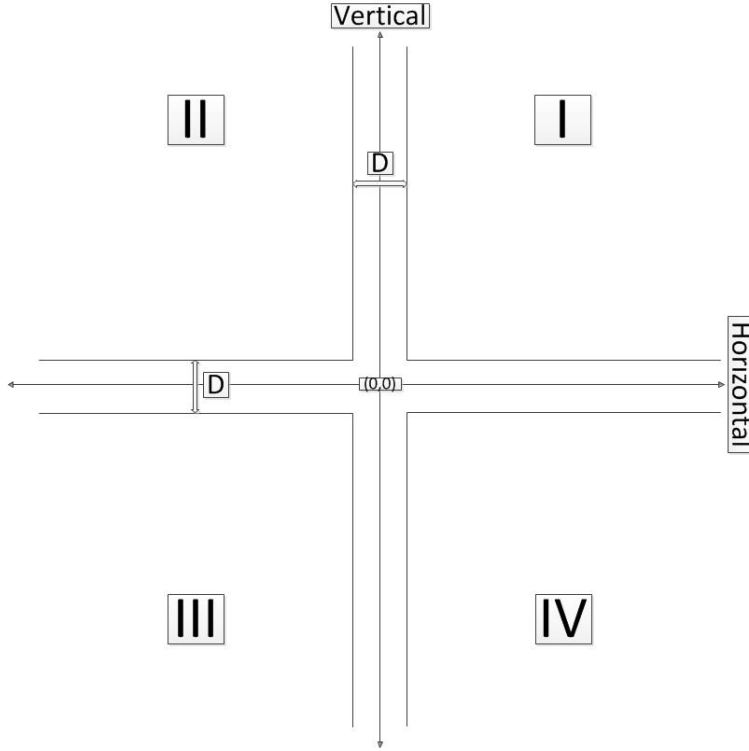


Figure 3.1: Array geometry for synthetic aperture implementation

To investigate the image reconstruction quality of the CSBS-based antenna arrays the same imaging scenario is considered. The parameters used in this scenario are given in Table 3.1. The only difference here is that the final number of antenna elements is set to 12, instead of 25.

The main goal here is to compare the performance of the design with the synthetic aperture to the optimized array in Sect. 2.3.2.2. Design algorithm starts with 72 antennas equally shared for transmit and receive antennas, and reduces the total number of antennas to 12. Moreover, the distance D between two locations is set to the distance between two neighboring antenna elements in the initial configuration, which is $2\lambda_c$.

3.1.3.2 Results for MAP Framework

Initial antenna arrays are illustrated in Fig. 3.2. The CSBS algorithm is applied using MAP framework at 30 dB SNR and the resulting array configurations are provided in Fig. 3.3. The designed arrays are copied to each array location so that one can

Table 3.1: Scenario parameters

Parameter	Value
Center frequency (f_c)	11 GHz
Bandwidth (B)	16.5 GHz
Number of frequency steps (F)	10
Center wavelength (λ_c)	2.73 cm
Number of image cube voxels (x, z, y)	19 x 19 x 3
Voxel size (x, z, y)	$\lambda_c, \lambda_c, \lambda_c$
Physical size of the image cube	$19\lambda_c \times 19\lambda_c \times 3\lambda_c$
Target distance to arrays (R)	$40\lambda_c$
SNR (dB)	30
Distance (D)	$2\lambda_c$

observe the overall design with synthetic aperture.

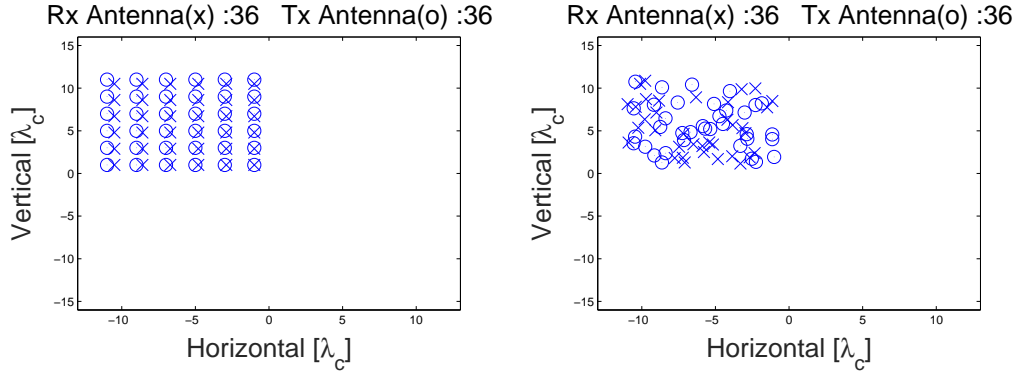


Figure 3.2: Initial configuration for synthetic aperture at one array plane location: Uniform initial distribution (left), random initial distribution (right)

Sample image reconstructions for point scatterer are provided in Fig. 3.4. The final cost values and the MSE values for different object types are given in Table 3.2. CSBS-based design with uniform initialization is better than the one with random

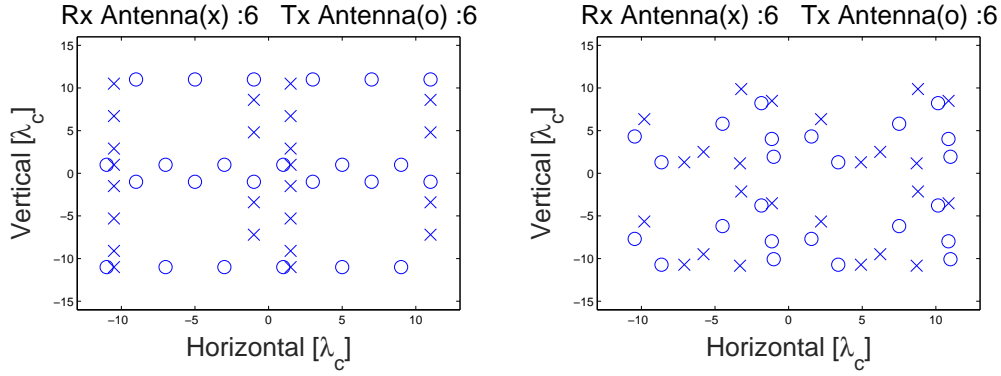


Figure 3.3: Optimal arrays for MAP framework at SNR of 30 dB: CSBS-designed with uniform initialization (left), CSBS-designed with random initialization (right)

Table 3.2: Cost and MSE values using MAP framework for PS, MPS, EO for SNR = 30 dB

Array Type	Init. Cost _{MAP}	Final Cost _{MAP}	MSE, PS	MSE, MPS	MSE, EO
CSBS-design, init. uniform	13.92	1.74e+3	0.012	0.08	0.69
CSBS-design, init. random	37.55	1.83e+3	0.016	0.09	0.99
CSBS-design, previous	3.74	0.9e+3	4.8e-3	2.5e-2	0.54

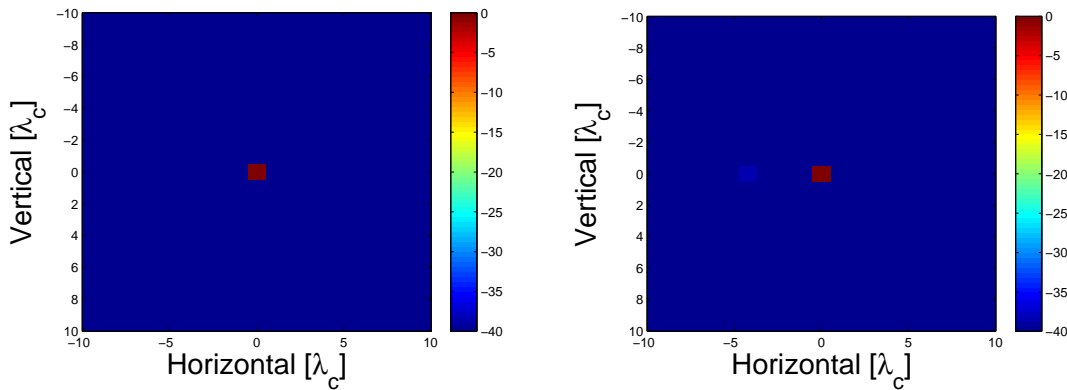


Figure 3.4: MAP results for point scatterer at SNR of 30 dB: CSBS-designed with uniform initialization (left), CSBS-designed with random initialization (right)

initialization in this case.

To compare the best design for the synthetic aperture case with the best MAP design

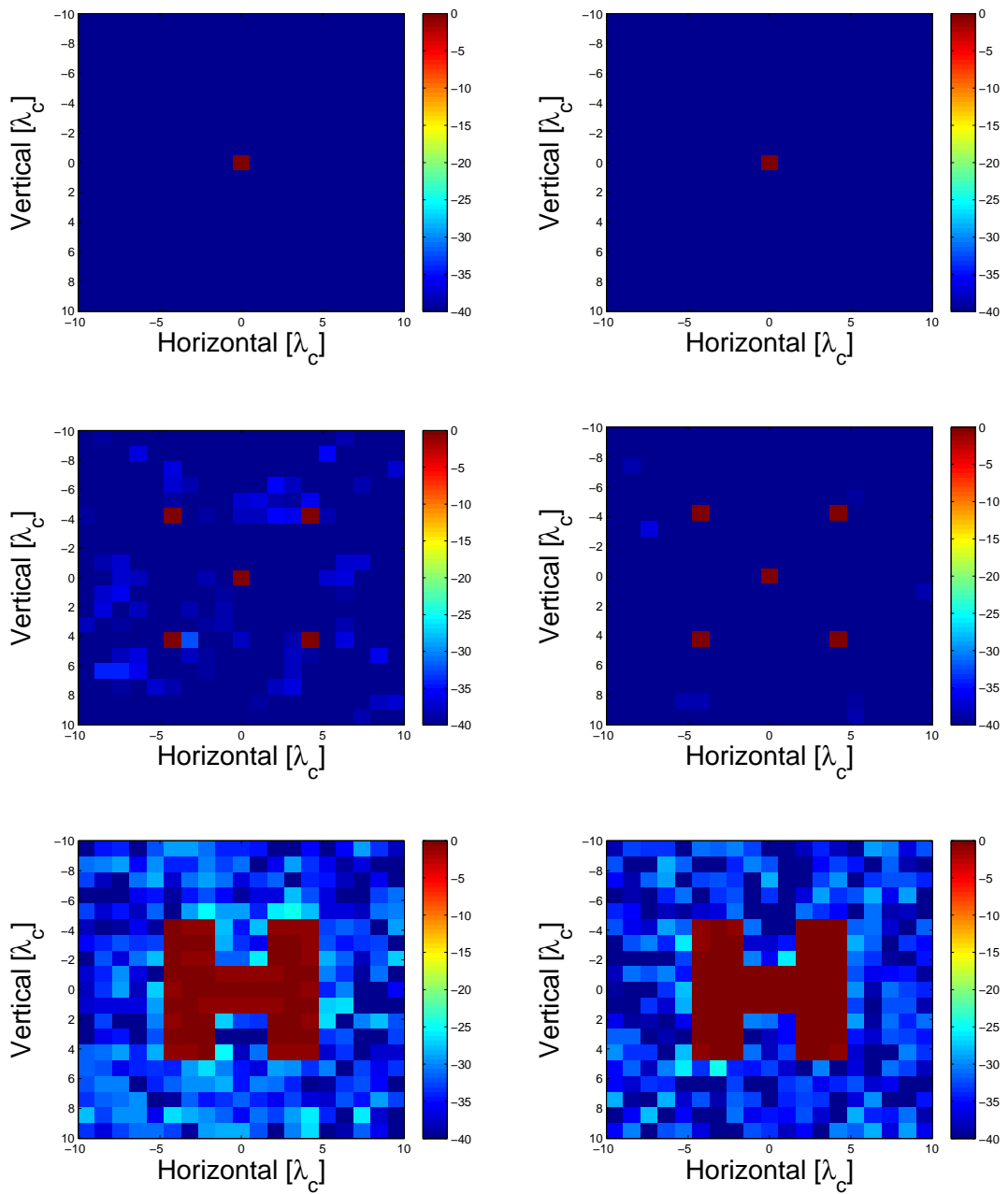


Figure 3.5: MAP results at SNR of 30 dB: CSBS-designed with uniform initialization, PS (upper left), CSBS-designed with uniform initialization from previous chapter, PS (upper right), CSBS-designed with uniform initialization, MPS (middle left), CSBS-designed with uniform initialization from previous chapter, MPS (middle right), CSBS-designed with uniform initialization, EO (bottom left), CSBS-designed with uniform initialization from previous chapter, EO (bottom right)

in the previous chapter at 30 dB SNR, the cost and MSE values for the earlier design are also provided in the table. Moreover, sample image reconstructions are shown in Fig. 3.5. The optimized array in the previous chapter slightly outperforms the optimized synthetic aperture array in terms of both cost and MSE values. However, it should be noted that in the synthetic aperture case, the number of antenna elements is 12, instead of 25. The reason behind degraded performance in synthetic aperture stems from the fact that transmissions and receptions are all made from one quadrant in the synthetic aperture geometry whereas in the previous chapter there is no limitation on locations for transmission and reception.

The virtual arrays of CSBS-designs are also provided in Fig. 3.6. The virtual array of the design with uniform initialization appears to be more uniform, which is consistent with its superior performance.

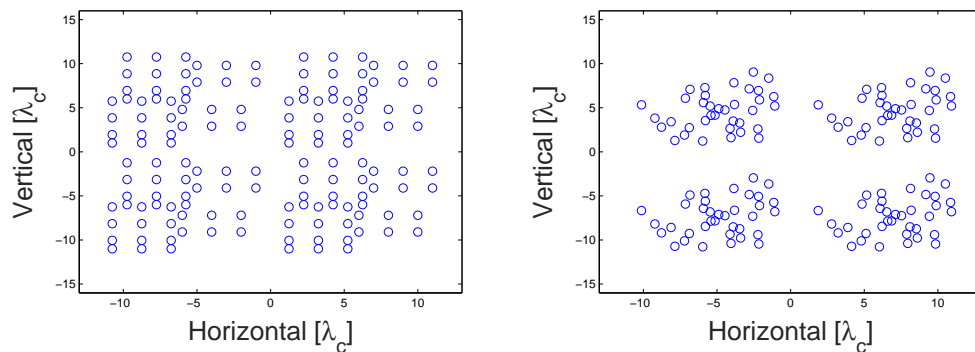


Figure 3.6: Virtual arrays for MAP at SNR of 30 dB: CSBS-designed with uniform initialization (left), CSBS-designed with random initialization (right)

3.2 Inclusion of Antenna Pattern

In this section, first the observation model is modified to include the antenna patterns in the formulation. Moreover, simulation results are presented to compare the optimized designs and the classical designs with different antenna patterns.

3.2.1 Observation Model

Prior to describing the transmitter and receiver antenna patterns, 3D spherical coordinate system should be introduced since antenna patterns can be expressed in this coordinate system. In Fig.3.7, the origin is considered as the location of a specific antenna element. The point at (r, θ, ϕ) is the location of the specific voxel in the imaging cube and r is the distance between the antenna element and the voxel. The antenna pattern can be selected such that it only depends on the angle θ , and not angle ϕ .

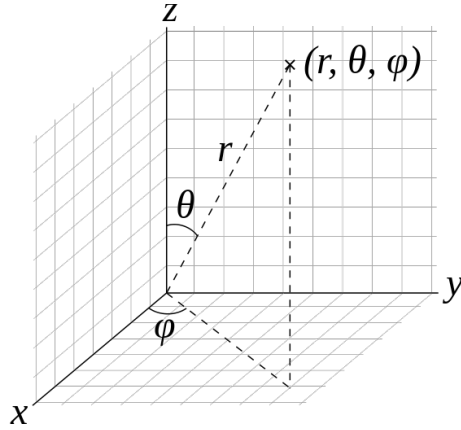


Figure 3.7: 3D Spherical Coordinate System [3].

After the inclusion of the antenna patterns, elements of the observation matrix become as follows:

$$A_{i,q} \approx \frac{p(k_l) e^{-jk_l d_{t_m}^{(q)}} e^{-jk_l d_{r_n}^{(q)}} g_m^{(q)} g_n^{(q)} \Delta x \Delta y \Delta z}{4\pi d_{t_m}^{(q)} d_{r_n}^{(q)}} \quad (3.5)$$

Here the only difference with the system matrix given earlier in Eqn. 2.10 is the addition of the terms $g_m^{(q)}$ and $g_n^{(q)}$. These terms $g_m^{(q)}$ and $g_n^{(q)}$ are the antenna patterns of the m th transmitter and n th receiver for the q th voxel, respectively. That is, the antenna pattern depends on the location of the antenna element and the voxel.

3.2.2 Optimal Design Method

Optimal design method used in this part is similar to the method utilized in Chapter 2. The only difference is in the formulation of the observation matrix. The antenna patterns for both transmit and receive antennas are taken into account in this part as given in Eqn. 3.5.

3.2.3 Numerical results

The aim of this section is to investigate the effect of different element patterns on the performance of CSBS-designs.

3.2.3.1 Simulation Scenario

In the simulations, the following element pattern is used [42]:

$$g_m^{(q)} = g_n^{(q)} = \cos^n(\theta), \quad (3.6)$$

Here the main beams of the transmit and receive antenna patterns are assumed to be the same regardless of the operating frequency. Corresponding antenna patterns are illustrated for $n = 4$ and $n = 40$ in Fig. 3.8, respectively.

Same simulation scenario is used. In this case, maximum θ value between an antenna element and a voxel is 24 degrees. Hence, the half power beamwidth should be larger than 24 degrees in order for each antenna element to cover the imaging cube. For this, value of n should be equal to, or smaller than 8. In the simulations, two different values are chosen: $n = 4$ and $n = 40$, for which the beamwidth is 33 and 11 degrees, respectively.

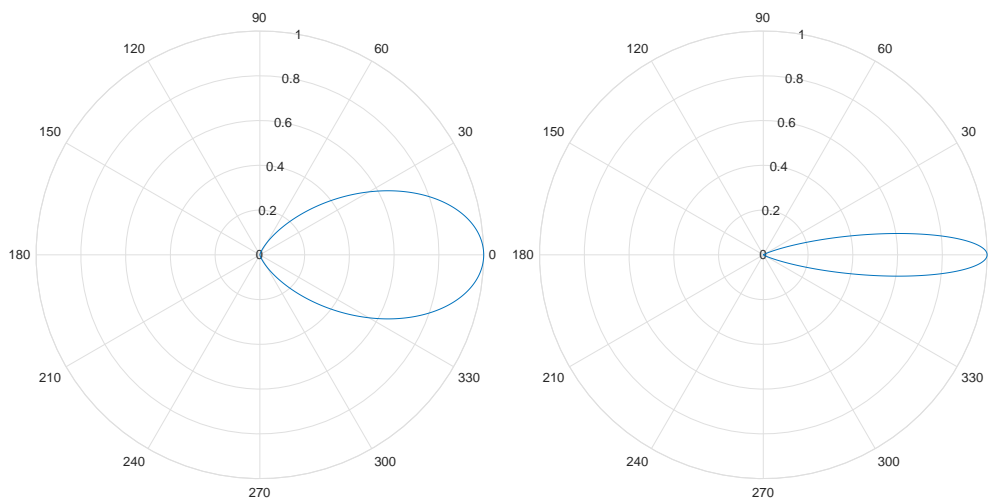


Figure 3.8: Normalized antenna beam patterns for different n values: $n = 4$ (left), $n = 40$ (right)

3.2.3.2 Results for MAP Framework

Same initial antenna arrays (see Fig. 2.2) are used to obtain designs for the MAP framework at 30 dB SNR. The resulting CSBS designs are shown in Fig. 3.9. The number of receive and transmit antennas in both designs are 12 and 13, respectively.

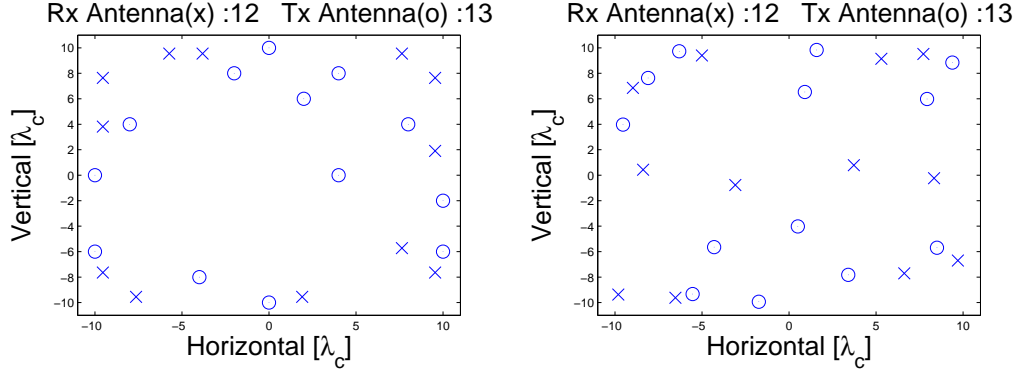


Figure 3.9: Optimal arrays for MAP framework, $n = 4$: CSBS-designed with uniform initialization (left), CSBS-designed with random initialization (right)

Table 3.3: Cost and MSE values using MAP framework for PS, MPS, EO for SNR = 30 dB, $n = 4$

Array Type	Init. Cost _{MAP}	Final Cost _{MAP}	MSE, PS	MSE, MPS	MSE, EO
CSBS-design, init. uniform	3.74	2.1e+3	9.4e-3	4.3e-2	0.90
CSBS-design, init. random	19.88	2.2e+3	1.2e-2	5.4e-2	1.03
Rectangular	-	2.9e+3	0.02	0.11	1.08
Mills Cross	-	3.8e+3	0.11	0.38	1.85
Ring-spiral	-	5.0e+3	0.20	0.70	2.34

It appears that element patterns for $n = 4$ case cause the antennas to locate closer to the center of the array plane. Moreover, the CSBS-designs outperform the classical arrays in terms of both cost and MSE values as shown in Table 3.3. It is concluded that the best array is the CSBS-based design with uniform initialization, and the best classical array is the rectangular array. Sample image reconstructions are also provided in Fig. 3.10 for PS. The image reconstruction results for the best CSBS-design and classical array are also shown for MPS and EO target types in Fig. 3.11. Furthermore, the

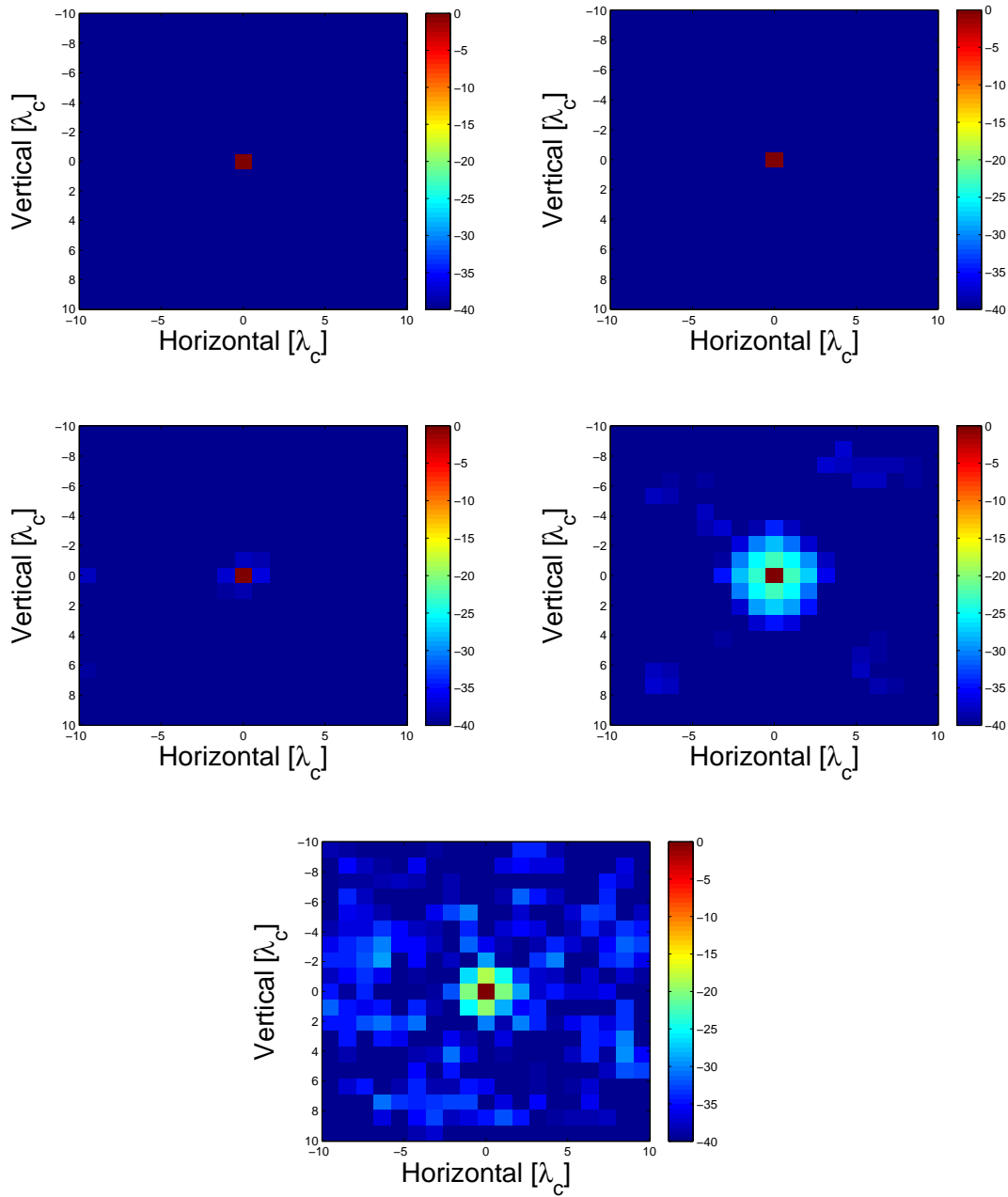


Figure 3.10: MAP results, $n = 4$ for PS: CSBS-designed with uniform initialization (upper left), CSBS-designed with random initialization (upper right), rectangular (middle left), Mills Cross (middle right), ring-spiral (bottom)

virtual arrays of CSBS-designs are also shown in Fig. 3.12. The virtual elements also appear to be closer to the center of the array plane.

The CSBS-designs for $n = 40$ case are shown in Fig. 3.13. The number of receiver

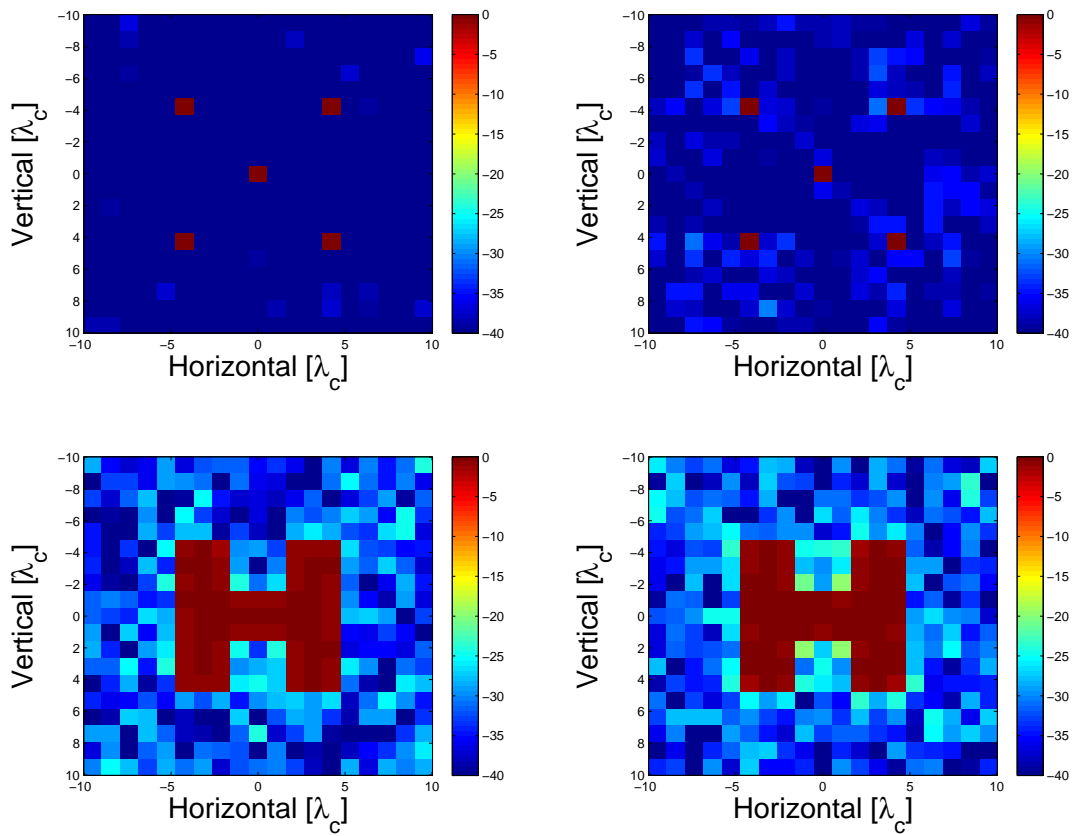


Figure 3.11: MAP results, $n = 4$: CSBS-designed with uniform initialization, MPS (upper left), rectangular, MPS (upper right), CSBS-designed with uniform initialization, EO (lower left), rectangular, EO (lower right)

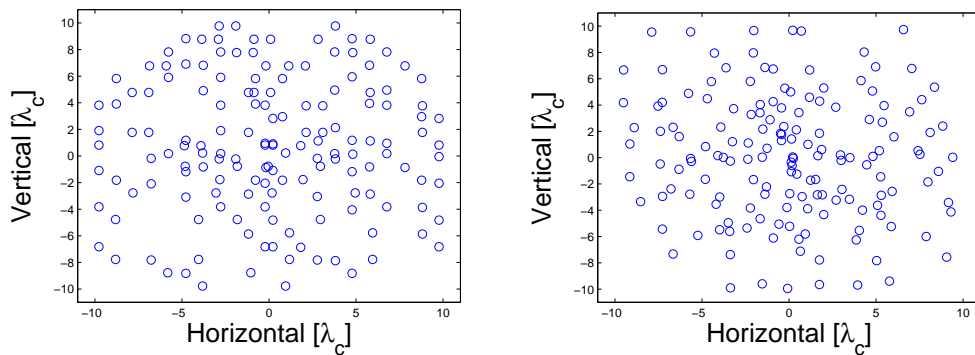


Figure 3.12: Virtual arrays for MAP framework, $n = 4$: CSBS-designed with uniform initialization (left), CSBS-designed with random initialization (right)

and transmitter antennas are 13 and 12 for the design with uniform initialization, and 12 and 13 for the design with random initialization.

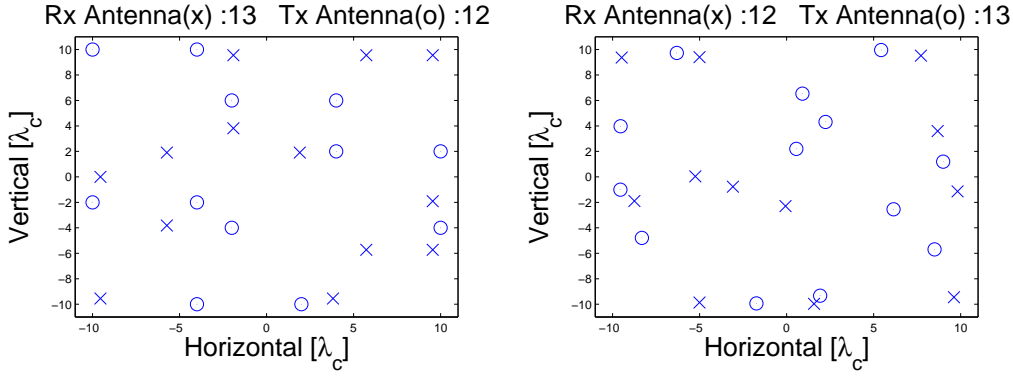


Figure 3.13: Optimal arrays for MAP framework, $n = 40$: CSBS-designed with uniform initialization (left), CSBS-designed with random initialization (right)

Table 3.4: Cost and MSE values using MAP framework for PS, MPS, EO for SNR = 30 dB, $n = 40$

Array Type	Init. Cost _{MAP}	Final Cost _{MAP}	MSE, PS	MSE, MPS	MSE, EO
CSBS-design, init. uniform	3.74	1.8e+5	9.7e-2	0.80	2.68
CSBS-design, init. random	19.88	1.8e+5	9.2e-2	0.67	2.47
Rectangular	-	2.2e+5	0.07	0.95	2.13
Mills Cross	-	2.5e+5	0.21	0.84	3.88
Ring-spiral	-	2.4e+5	0.17	1.00	2.95

The effect of beampattern on the locations of the antennas are more clearly observed as opposed to $n = 4$ case. The antennas are located much closer to the center of the array plane for both designs.

The CSBS-designs again outperform the classical arrays in terms of cost values as shown in Table 3.4. It is concluded that, in terms of cost values, the best design is CSBS-based design with random initialization, and the best classical array is the rectangular array. Sample image reconstructions for PS are also provided in Fig. 3.14. The image reconstruction results for the best CSBS-designs and classical arrays are also shown for MPS and EO target types in Fig. 3.15. It is observed that CSBS-designs generally yield better reconstructions, but not always.

The virtual arrays of the CSBS-designs are also illustrated in Fig. 3.16. It is observed

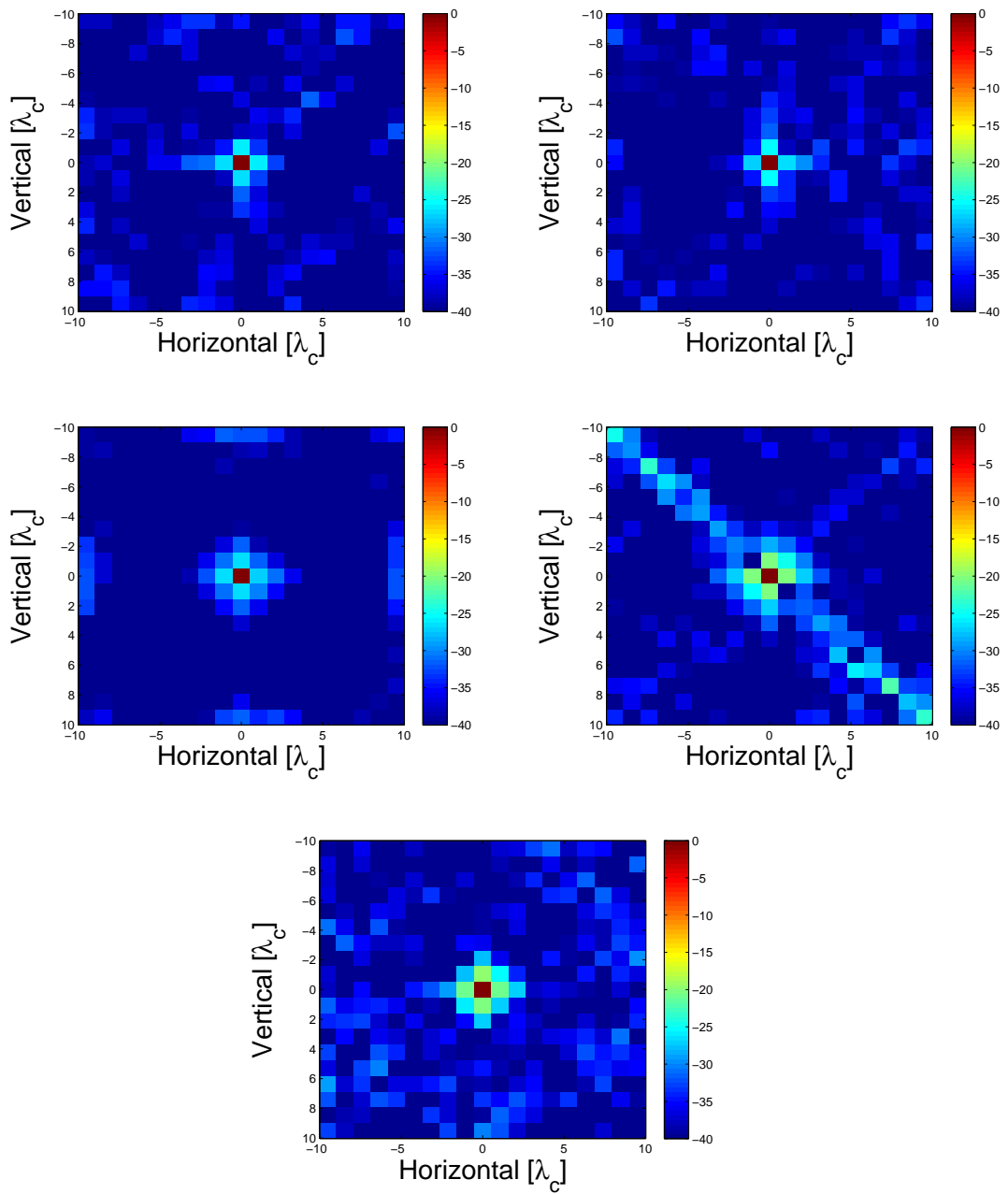


Figure 3.14: MAP results, $n = 40$ for PS: CSBS-designed with uniform initialization (upper left), CSBS-designed with random initialization (upper right), rectangular (middle left), Mills Cross (middle right), ring-spiral (bottom)

that the elements of the virtual array are more concentrated at the center of the array plane.

Finally, the effect of antenna pattern on the CSBS-designs is illustrated in Fig. 3.17.

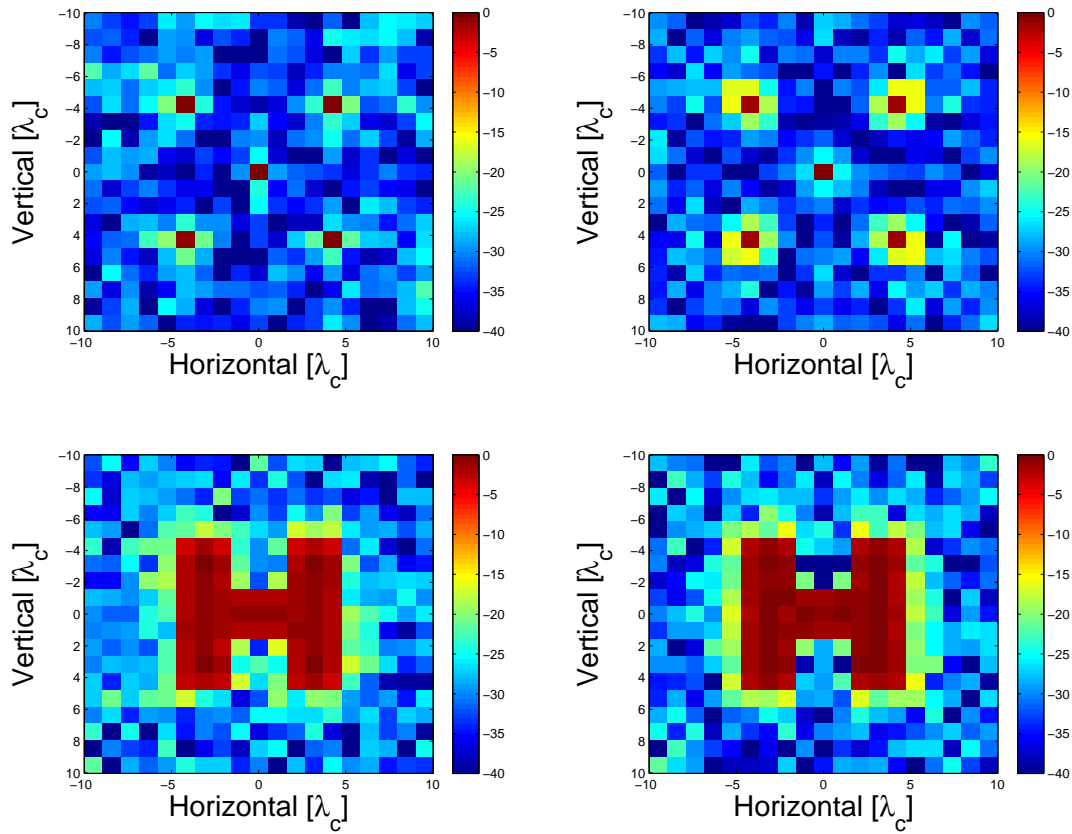


Figure 3.15: MAP results, $n = 40$: CSBS-designed with random initialization, MPS (upper left), rectangular, MPS (upper right), CSBS-designed with random initialization, EO (lower left), rectangular, EO (lower right)

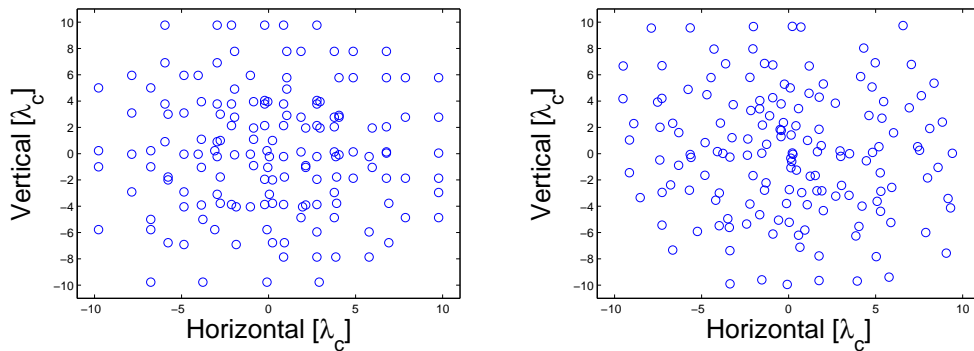


Figure 3.16: Virtual arrays for MAP framework, $n = 40$: CSBS-designed with uniform initialization (left), CSBS-designed with random initialization (right)

As antenna beam pattern becomes more directed with increasing value of n , the antenna elements are more concentrated in the middle of the array plane and less con-

centrated at the edges.

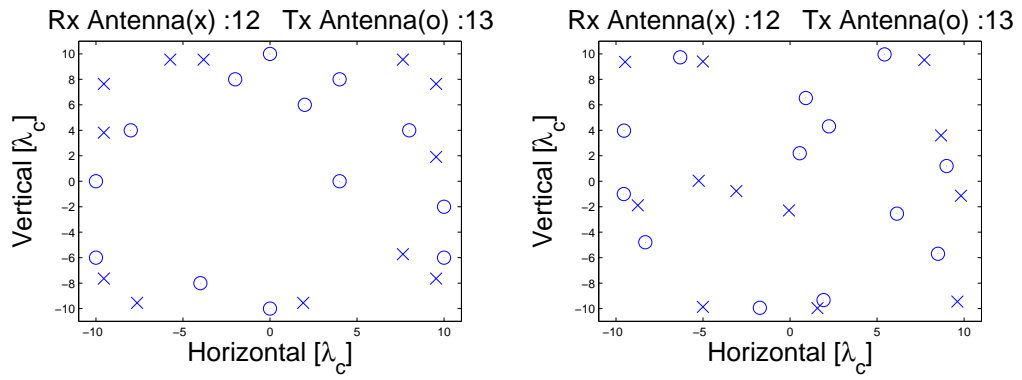


Figure 3.17: Best optimal arrays for MAP framework: $n = 4$ (left), $n = 40$ (right)

CHAPTER 4

CONCLUSIONS

In this thesis, a design approach is presented for two-dimensional MIMO arrays used in wideband near-field imaging. Different than the earlier design approaches, the quality of the reconstructed images obtained with the design is taken into account with a statistical approach. For this purpose, the problem of image reconstruction from MIMO measurements is formulated as an estimation problem using ML and MAP frameworks (or, equivalently, least-squares (LS) and Tikhonov-regularized LS approaches), and the trace of the error covariance matrix is chosen as the optimality criterion for the final design.

The clustered sequential backward selection (CSBS) algorithm is used to perform the optimization of the chosen criterion over all initial locations of antenna elements. That is, the algorithm starts with an initial antenna configuration (either a uniform or a random configuration), and iteratively reduces the antenna elements based on the chosen optimality criterion until the desired number of elements is reached. The performance of the CSBS designs is then illustrated for a microwave imaging application. The imaging performance of the designed MIMO arrays are analyzed for different observation settings, and compared with the classical MIMO designs.

In particular, the design approach is described in detail in Chapter 2, which includes the forward problem, statistical image reconstruction approaches, the related design cost formulation and the optimization method. The designs obtained with our approach are compared with some commonly used sparse array configurations, such as Mills Cross, rectangular and ring-spiral arrays, at different SNRs. It is observed that the CSBS-designs outperform the classical designs at each SNR in terms of cost values, regardless of the chosen framework. Moreover, the MAP framework outperforms

the ML framework in terms of both cost and MSE values especially at lower SNRs of 30 and 15 dB. The CSBS-designs obtained using ML and MAP frameworks are also compared with each other, which reveals the sub-optimality of the CSBS algorithm.

The developed design approaches are also flexible; they allow incorporating different practical considerations into the design. This is illustrated in Chapter 3, by extending the design approach to include synthetic aperture implementations and antenna patterns. The simulation results are presented for the MAP framework and 30 dB SNR case. The results for the synthetic aperture case are compared with the best MAP design obtained in Chapter 2. It is observed that the synthetic aperture implementation with the number of antenna elements reduced to half provides similar imaging performance with the earlier design. Moreover, the results for the antenna pattern case are compared with the classical designs using different antenna patterns. It is again observed that the CSBS-designs outperform the classical arrays in terms of cost values, although for more directed antenna patterns the difference in the cost values becomes small. Moreover, as the antenna pattern becomes more directed, the antenna elements in the CSBS-designs are located closer to the center of the array plane, as expected.

4.1 Future Work

As future work, the prior distribution used in the MAP framework can be changed to enforce sparse reconstructions. This can yield designs with improved imaging quality. Moreover, different constraints can be added to the design optimization problem to produce more realistic designs. For instance, the distance between different antenna elements in the final design can be set to a minimum value and enforced in the design optimization [43]. In addition, it may be possible to improve the CSBS-designs by rerunning the suboptimal CSBS algorithm with the randomly perturbed designs, which is also a topic of future study.

REFERENCES

- [1] R. E. Blahut, *Theory of remote image formation*. New York City, NY: Cambridge University Press, 2004.
- [2] X. Zhuge and A. G. Yarovoy, “Three-dimensional near-field MIMO array imaging using range migration techniques,” *IEEE Trans. on Image Process.*, pp. 3026–3033, 2012.
- [3] P. Moon and D. E. Spencer, *Field theory handbook including coordinate systems differential equations and their solutions*. Berlin, Germany: Springer-Verlag, 1961.
- [4] X. Zhuge and A. G. Yarovoy, “A sparse aperture MIMO-SAR-based UWB imaging system for concealed weapon detection,” *IEEE Trans. on Geosci. and Remote Sensing*, pp. 509–518, 2011.
- [5] D. M. Sheen *et al.*, “Three-dimensional millimeter-wave imaging for concealed weapon detection,” *IEEE Trans. on Microwave Theory and Techniques*, pp. 1581–1592, 2001.
- [6] I. Catapano and L. Crocco, “An imaging method for concealed targets,” *IEEE Trans. on Geosci. and Remote Sensing*, pp. 1301–1309, 2009.
- [7] E. C. Fear *et al.*, “Microwaves for breast cancer detection?,” *IEEE potentials*, pp. 12–18, 2003.
- [8] M. Klemm *et al.*, “Radar-based breast cancer detection using a hemispherical antenna array? Experimental results,” *IEEE Trans. on Antennas and Propagation*, pp. 1692–1704, 2009.
- [9] A. T. Mobashsher *et al.*, “An imaging method for concealed targets,” *IEEE Trans. on Microwave Theory and Techniques*, pp. 1826–1836, 2014.
- [10] M. G. Amin, *Through-the-wall radar imaging*. Boca Raton, FL: CRC press, 2016.
- [11] X. Zhuge and A. Yarovoy, “Sparse multiple-input multiple-output arrays for high-resolution near-field ultra-wideband imaging,” *IET Microwaves, Antennas & Propagation*, pp. 1552–1562, 2011.
- [12] A. G. Yarovoy *et al.*, “UWB array-based sensor for near-field imaging,” *IEEE Trans. on Microwave Theory and Techniques*, pp. 1288–1295, 2007.

- [13] A. Yarovoy, "Ultra-wideband radars for high-resolution imaging and target classification," in *Proc. European Radar Conf. (EuRAD)*, pp. 1–4, Germany, 2007.
- [14] X. Zhuge *et al.*, "Modified Kirchhoff migration for UWB MIMO array-based radar imaging," *IEEE Trans. on Geosci. and Remote Sensing*, pp. 2692–2703, 2010.
- [15] X. Zhuge *et al.*, "UWB array-based radar imaging using modified Kirchhoff migration," in *Proc. Int. Conf. on Ultra-Wideband (ICUWB)*, pp. 175–178, Germany, 2008.
- [16] C. R. Vogel, *Computational methods for inverse problems*. Philadelphia, PA: Society for Industrial and Applied Mathematics, 2002.
- [17] S. S. Ahmed, A. Schiessl, and L.-P. Schmidt, "Multistatic mm-wave imaging with planar 2D-arrays," in *Proc. German Microwave Conf.*, pp. 1–4, Germany, 2009.
- [18] J. F. Federici *et al.*, "THz imaging and sensing for security applications—explosives, weapons and drugs," *IOP Semiconductor Sci. and Tech.*, p. S266, 2005.
- [19] V. Murino *et al.*, "Synthesis of unequally spaced arrays by simulated annealing," *IEEE Trans. on Signal Processing*, pp. 119–122, 1996.
- [20] K. Yang *et al.*, "Synthesis of sparse planar arrays with matrix pencil method," in *Proc. Int. Conf. on Computational Problem-Solving (ICCP)*, pp. 82–85, 2011.
- [21] W. Zhang *et al.*, "Reducing the number of elements in linear and planar antenna arrays with sparseness constrained optimization," *IEEE Trans. on Antennas and Propagation*, pp. 3106–3111, 2011.
- [22] L. F. Yepes *et al.*, "Synthesis of two-dimensional antenna array using independent compression regions," *IEEE Trans. on Antennas and Propagation*, pp. 449–453, 2013.
- [23] K. Tan *et al.*, "A novel two-dimensional sparse MIMO array topology for UWB short-range imaging," *IEEE Antennas and Wireless Propagation Letters*, pp. 702–705, 2016.
- [24] X. Zhuge and A. G. Yarovoy, "Study on two-dimensional sparse MIMO UWB arrays for high resolution near-field imaging," *IEEE Trans. on Antennas and Propagation*, pp. 4173–4182, 2012.
- [25] X. Zhuge and A. Yarovoy, "Near-field ultra-wideband imaging with two-dimensional sparse MIMO array," in *Proc. European Conf. on Antennas and Propagation (EuCAP)*, pp. 1–4, Spain, 2010.

- [26] K. Tan *et al.*, “On sparse MIMO planar array topology optimization for UWB near-field high-resolution imaging,” *IEEE Trans. on Antennas and Propagation*, pp. 989–994, 2017.
- [27] R. T. Hoctor and S. A. Kassam, “The unifying role of the coarray in aperture synthesis for coherent and incoherent imaging,” *Proceedings of the IEEE*, pp. 735–752, 1990.
- [28] P. Pal and P. Vaidyanathan, “Nested arrays: A novel approach to array processing with enhanced degrees of freedom,” *IEEE Trans. on Signal Process.*, pp. 4167–4181, 2010.
- [29] P. Pal and P. Vaidyanathan, “Nested arrays in two dimensions, part i: Geometrical considerations,” *IEEE Trans. on Signal Process.*, pp. 4694–4705, 2012.
- [30] P. Pal and P. Vaidyanathan, “Nested arrays in two dimensions, part ii: Application in two dimensional array processing,” *IEEE Trans. on Signal Process.*, pp. 4706–4718, 2012.
- [31] S. Qin *et al.*, “DOA estimation of mixed coherent and uncorrelated targets exploiting coprime MIMO radar,” *Digital Signal Process.*, pp. 26–34, 2017.
- [32] S. Qin *et al.*, “Generalized coprime array configurations for direction-of-arrival estimation,” *IEEE Trans. on Signal Process.*, pp. 1377–1390, 2015.
- [33] P. P. Vaidyanathan and P. Pal, “Sparse sensing with co-prime samplers and arrays,” *IEEE Trans. on Signal Process.*, pp. 573–586, 2011.
- [34] P. Vaidyanathan and P. Pal, “Theory of sparse coprime sensing in multiple dimensions,” *IEEE Trans. on Signal Process.*, pp. 3592–3608, 2011.
- [35] S. Qin *et al.*, “DOA estimation of mixed coherent and uncorrelated signals exploiting a nested MIMO system,” in *Proc. Benjamin Franklin Symp. on Microw. and Antenna Sub-Syst. Radar, Telecommun., and Biomed. Appl. (BenMAS)*, pp. 1–3, USA, 2014.
- [36] K. Tan *et al.*, “A novel two-dimensional MIMO array topology for UWB near-field high-resolution imaging,” in *Proc. Int. Conf. on Ground Penetrating Radar (GPR)*, pp. 1–4, Hong Kong, 2016.
- [37] B. Sharif and F. Kamalabadi, “Optimal sensor array configuration in remote image formation,” *IEEE Trans. on Image Process.*, pp. 155–166, 2008.
- [38] M. B. Kocamis and S. F. Oktem, “Optimal MIMO array configuration for ultra-wideband microwave imaging,” in *Proc. Signal Process. and Commun. Applicat. Conf. (SIU)*, pp. 1–4, Turkey, 2017.
- [39] S. M. Kay, *Fundamentals of Statistical Signal Processing: Estimation Theory*.

- [40] M. B. Kocamis and S. F. Oktem, “Optimal design of sparse MIMO arrays for near-field ultrawideband imaging,” in *Proc. European Signal Process. Conf. (EUSIPCO)*, pp. 1952–1956, Greece, 2017.
- [41] M. Cetin, “Feature-Enhanced synthetic aperture radar imaging,” Ph.D. thesis, Dept. Elect. & Electron. Eng., Boston Univ., USA, 2001.
- [42] C. A. Balanis, *Antenna Theory: Analysis and Design*. Hoboken, NJ: WILEY, 2016.
- [43] G. Gok, “Sparse sensor array design via constrained optimization,” Ph.D. thesis, Dept. Elect. & Electron. Eng., METU, Turkey, 2013.